High-pressure Raman scattering of pure and doped $PbSc_{0.5}Ta_{0.5}O_3$ and $PbSc_{0.5}Nb_{0.5}O_3$ single crystals

Dissertation

Zur Erlangung des Doktorgrades der Naturwissenschaften im Department
Geowissenschaften der Universität Hamburg

vorgelegt von

Anna-Maria Welsch, Dipl. Ing.

(Ana-Maria Velč, Dipl. Ing.)

aus

Belgrad, Serbien

Hamburg
2009

Als Dissertation angenommen vom Department Geowissenschaften der Universität Hamburg

Auf Grund der Gutachten von Prof. Dr. Boriana Mihaylova (Jun.-Prof.)

und Prof. Dr. Ulrich Bismayer

Hamburg, den 18.12.2009

Prof. Dr. Oßenbrügge

Leiter des Department Geowissenschaften

Contents

Summary

Relaxor ferroelectrics (relaxors) and related materials have outstanding dielectric, electromechanical and optoelectric properties, presenting vast possibilities for technological applications. The exceptional relaxor properties are intrinsically related to the complex nanoscale structural features characterized by the existence of polar nano-regions embedded within the cubic host matrix. The majority of relaxors are Pb-based complex oxides of perovskite-type with the general formula ABO_3. The flexibility of this structure type enables the coexistence of ferroelectrically active and inactive cations in both A and B crystallographic sites as well as the formation of chemically ordered nanoregions inside a chemically ordered matrix. Although there are extensive studies on relaxors made over the past decade, the relation between nanoscale chemical and structural (ferroic) inhomogeneities is still not well understood. Pressure is a much stronger driving force than temperature and thus high-pressure experiments are vial to clarify the structural peculiarities and transformation processes in relaxors.

To elucidate the primary role of local elastic and local electric fields associated with compositional fluctuations for the suppression of long-range ferroelectric order, which is essential for the relaxor state, for the first time a comprehensive high-pressure Raman spectroscopic study on stoichiometric, mixed and A-site doped $PbSc_{0.5}Ta_{0.5}O_3$ (PST) and $PbSc_{0.5}Nb_{0.5}O_3$ single crystals as model relaxor systems was performed in this thesis.

In combination with X-ray diffraction analysis, a pressure-induced phase transition was observed for the first time in this class of materials. The phase transition is of second order. It is realized via a precursor violation of the dynamical coupling between the B-site and Pb^{2+} cations in the polar nanoregions, a consequent decrease in the B-cation polar shifts and an increase in the coherence of ferroic Pb-O species. The comparison between the pressure dependence of phonon modes in pure PST and PSN reveal that ferroic Pb-O-Nb linkages are more stable to elastic stress than the corresponding Pb-O-Ta linkages, which leads to a higher critical pressure in PSN as compared to PST.

For the first time a diffuse pressure-induced phase transition over a pressure range was observed in the newly synthesized relaxor $Pb_{0.78}Ba_{0.22}Sc_{0.5}Ta_{0.5}O_3$. The pressure evolution of phonon anomalies in this novel canonical relaxor reveals that the smearing out of the phase transition results from local elastic fields in the vicinity of incorporated Ba cations. The dilution of the system of Pb^{2+} cations, having the affinity to form lone pairs, with isovalent cations of larger ionic radius and isotropic electron shell suppresses the development of pressure-induced long-range ferroic order, in spite of the existence of B-site

chemically long-range ordered regions. This underlines the primary role of potential barriers related to elastic strains for the formation of the relaxor state.

The detailed comparative analysis of the high-pressure Raman spectra of PSN doped with Ba^{2+} and Bi^{3+} shows that the incorporation of aliovalent A-site cation (Bi^{3+}) with nearly the same ionic radius and outermost electron shell as those of Pb^{2+} does not suppress and even enhances the pressure-induced ferroic ordering processes, although the introduction of additional charge imbalance, whereas the incorporation of Ba^{2+} has the same effect as in the case of PST. This highlights the predominant effect of local elastic fields over local electric fields related to compositional disorder in the A-site.

Under pressure the solid solution of PST and PSN shows an intermediate behaviour with structural features characteristic of PST and PSN. An additional lowest-energy Raman signal observed in PST at the critical pressure is also observed in PST-PSN at nearly the same pressure point; however, abundant suppression of polar shifts of B-cations occurs near the corresponding pressure point in PSN. The addition of Ba^{2+} leads to the same type of renormalization of the pressure-induced structural transformations as in the case of the individual end members PST and PSN.

1. Introduction to Perovskite-type Relaxors

1.1 Ferroelectricity

Ferroelectricity represents a spontaneous electric polarization of a material with two or more stable equivalent orientational states that can be reversed by the application of an external electric field. It was first discovered in Rochelle salt, $NaKC_4H_4O_6 \cdot 4H_2O$ by Valasek [1], but only after it was observed in perovskite-type materials it became clear that this phenomenon is the electrical analogue of ferromagnetism.

Spontaneous polarization is found among crystals belonging to the 10 pyroelectric crystallographic classes. The highest-symmetry structure compatible with the ferroelectric material is called *prototype phase*. The phase which changes into the ferroelectric phase is referred to as the *paraelectric phase*. Usually, the prototype and the paraelectric phase are one and the same and exist above the Curie temperature, T_C [2].

At T_C a macroscopic paralectric-to-ferroelectric transition takes place, resulting in the appearance of the spontaneous polarization $\mathbf{P}_S$ (fig.1.1a). In the vicinity of T_C, the static dielectric permittivity ε exhibits a sharp peak marking the temperature of the ε maximum value as T_m (figure1.1a). The Curie temperature T_C is very close to T_m but not coincidental. Above T_C, in the paraelectric state the temperature dependence of ε follows the Curie-Weiss law:

$$\varepsilon = \frac{C}{T - T_C} \quad , \tag{1.1}$$

where C is the material-specific Curie constant and T is the temperature, measured in Kelvins. Upon reaching the maximum value of ε, a phase transition occurs and the magnitude of ε drops (fig 1.1c). At both sides of the maximum, ε exhibits a very weak frequency dispersion.
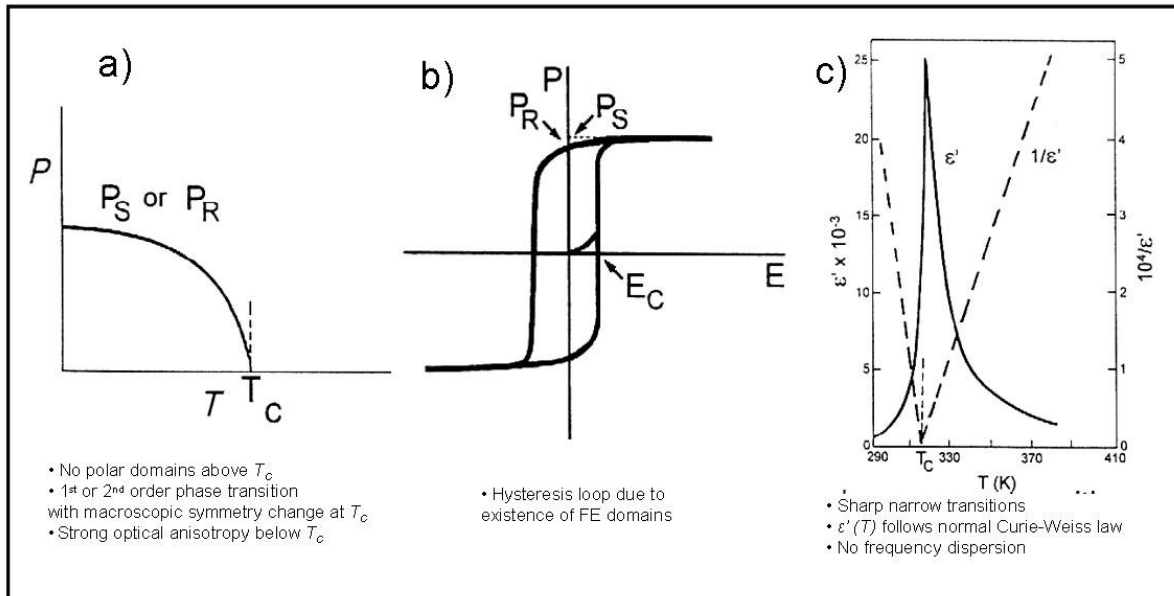
Figure 1.1 Properties of a ferroelectric, after Samara and Venturini, 2006 [3]

Ferroelectric materials can be classified into two groups relative to the *origin* of P_S:

1. displacive type – cations shift against anions in an ionic crystal, as in the case of $PbTiO_3$
2. order-disorder type – permanent dipole moments which are randomly oriented at high temperatures align into domains [4].

Since 1920-ties, ferroelectrics have evolved into a wide and constantly expanding scientific field. Many studies have focused on the understanding of how to control and tailor their features for technological applications, via different chemistry, synthesizing conditions, external fields etc. In the last two decades, the utilization of ferroelectric compounds as single crystals, ceramics or films, has seen an exponential growth and novel compounds keep on bringing up new scientific challenges.

1.2 Relaxor Ferroelectrics. Characteristic Features

Relaxor ferroelectrics, or *relaxors*, are ferroelectric materials with a diffuse phase transition over a temperature range, as revealed by the very broad peak of the dielectric permittivity ε as a function of T and a strong frequency dispersion of $\varepsilon(T)$. Some relaxors develop a long-range ferroelectric order (fig 1.2b), whereas canonical relaxors (fig 1.2c) remain isotropic with respect to X-rays and polarized light even at 4 K.

The temperature dependence of ε in relaxor materials strongly deviates from the standard Curie-Weiss law and follows a special quadratic Curie-Weiss law: $\varepsilon \propto \dfrac{1}{(T - T_C)^2}$ [5].

Dielectric properties of these materials are marked by large values of temperature-insensitive but strongly frequency-dependent ε with large dispersion over a considerable temperature range. The name 'relaxors' is directly related to the exhibited dielectric relaxation. The unusually high values and the atypical behaviour of ε, as well as the very small thermal expansion throughout the Curie range, make relaxors very interesting from the aspect of technological applications, including novel memory devices, electrostrictive actuators, sonars and high-frequency bio-medical transducers [6, 7].
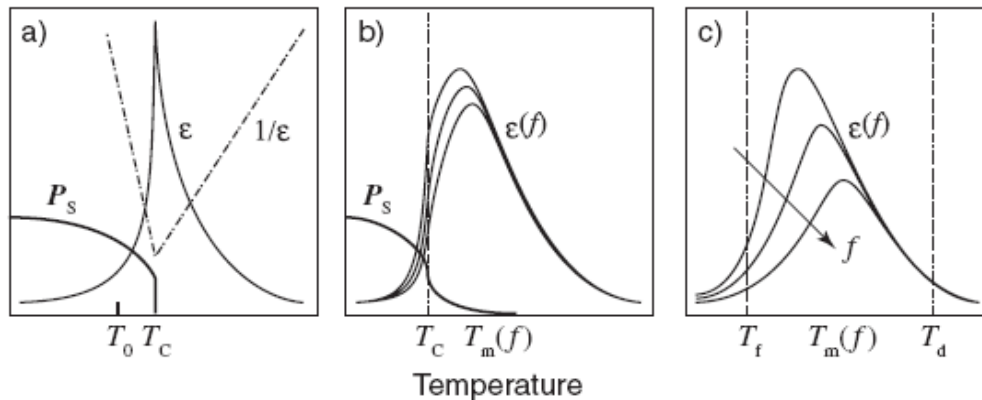
Figure 1.2 Schematic presentation of ε and $\mathbf{P}_S$ for a) normal ferroelectrics, b) relaxors that undergo a phase transition into ferroelectrics and c) canonical relaxor ferroelectrics –after Hirota et al [8]

The unusual features of relaxor ferroelectrics are intrinsically linked to their complex nano-scale structure. Unlike normal ferroelectrics, which have a sharp, well defined paralectric-to-ferroelectric phase transition at T_C, relaxors undergo a sequence of structural transformations marked by characteristic temperature points (fig 2.3). According to pair-distribution function analysis and Raman spectroscopy, even at very high temperatures, the paralectric cubic state of a relaxor is violated by individual incoherent ferroic atomic shifts [9,

10, 14]. Upon cooling, individual atomic shifts couple to form the dynamical polar nano-regions (*PNRs*). The temperature at which first PNRs occur was first detected by Burns and Dacol via the deviation of the refractive index from the linear dependence [11], and is referred now to as the Burns temperature T_B. The system of the cubic matrix embedding randomly distributed and oriented PNRs is in the so-called *ergodic state* because from the thermodynamical point of view the average of the microscopic structural state over time does not yield any preferential polar direction.

Upon further cooling, at a temperature point designated as *T**, the initially formed PNRs grow and *couple* via the electric field. The larger size of the ferroic domains within the paraelectric matrix result in the local accumulation of the elastic strain. As a consequence, an acoustic emission is observed at *T** and the pseudo-cubic unit cell parameter deviates from its linear dependence [12, 13, 14].
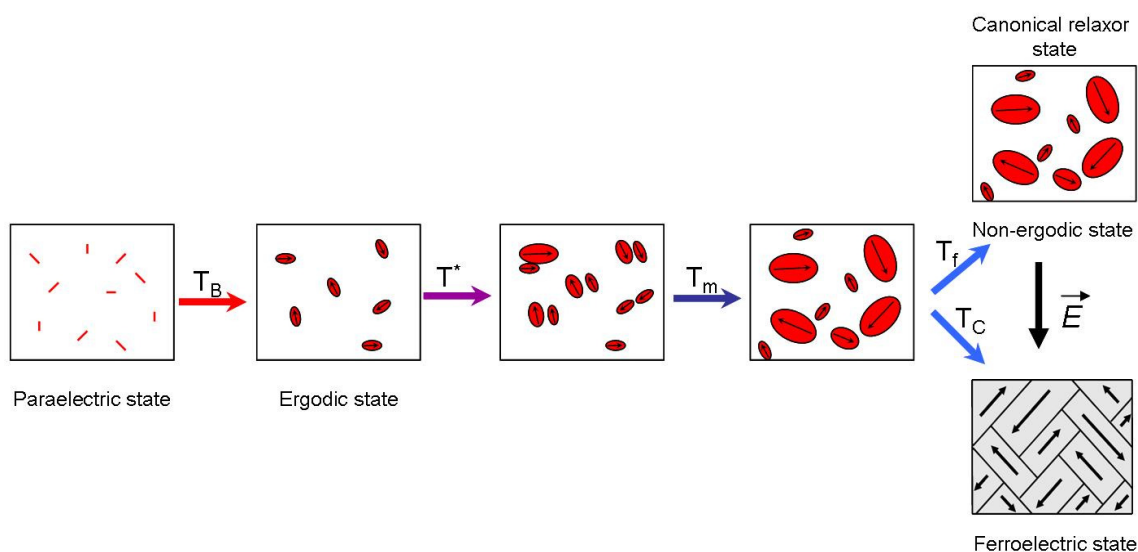
Figure 1.3 Schematic temperature-induced transformation sequence of relaxor materials.

The temperature of the maximum ε value T_m, marks the peak point in abundance and size of the PNRs with an average lifetime of $10^{-4} - 10^{-5}$ s [15]. Below T_m relaxors either undergo a phase transition to a normal ferroelectric state at T_C, i.e. develp a long-range ferroelectric phase or transform to a non-ergodic state at T_f (fig 1.3), consisting of static PNRs without establishing ferroelectric long-range order. The latter is typical of canonical relaxors. Under the influence of a strong electric field, canonical relaxors can be irreversibly transformed into a regular long-range ordered ferroelectric state. In this aspect, relaxors differ from typical dipole glasses.

The existence of PNRs, has been proved by various methods (elastic neutron and X-ray scattering [8, 16-25], Raman spectroscopy [26-29], nuclear magnetic resonance [31, 32], pair distribution function [33, 34]). PNRs are responsible for the majority of the peculiar features exhibited by relaxors, including the dispersion of the $\varepsilon(T)$-peak and the occurrence of polarization above T_C. However, the real nature and mechanism of the PNRs is still not well understood and explanations are contradictive. So far, it is accepted that the formation of PNRs is closely related to chemically-induced disorder and that in the formation and evolution of the ferroic nano-domains the type of cations plays a significant role.

1.3 Perovskite-type structure

Most of relaxor materials are complex oxides of two structural types:

1. Tungsten bronze-type systems, of general formula $M_{1-x}Ba_xNb_2O_6$ (M = Sr, Pb) [35];

2. Perovskite-type systems of the general formula ABO_3 (A = Pb^{2+}, Na^+, K^+, Ba^{2+} La^{3+}, Bi^{3+}; B = Mg^{2+}, Zn^{2+}, Sc^{3+}, Fe^{3+}, In^{3+}, Ta^{5+}, Nb^{5+}, W^{6+}, Ti^{4+}) and three subcategories relative to the type of cations on A- or B- sites:

   - A-site complex, $(A'A'')BO_3$ like $Pb_{1-x}La_{2x/3}TiO_3$ or $Na_{0.5}Bi_{0.5}TiO_3$

   - B-site complex, $A(B'B'')O_3$ with B-site cations being either in 1:1 ratio (as in $PbSc_{1/2}Ta_{1/2}O_3$) or 2:3 (as in $PbMg_{1/3}Nb_{2/3}O_3$)

   - Mixed A- and B-site complex $(A'A'')(B'B'')O_3$ (e.g. $Pb_{0.91}La_{0.09}Zr_{0.65}Ti_{0.35}O_3$) [36, 37]
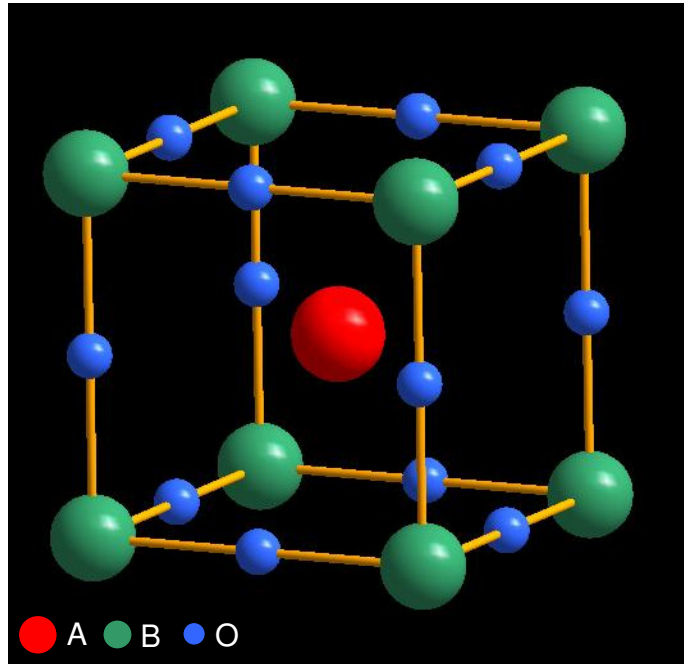
Figure 1.4 Example of the cubic perovskite-type structure of the general formula ABO_3; structure shown is the typical $Pm\bar{3}m$ cell which the majority of relaxor materials occupy above T_m.

The ABO_3 structure allows heterovalency of different cation types to occupy crystallographically equivalent sites in different ratios and with a certain degree of substitutional disorder. This substitutional disorder is a common precondition for the relaxor behaviour, as it consequently bears large influence on the dispersion of $\varepsilon(T)$ and via a proper choice of ionic system it enables fine tuning of the desired effects. Based on excessive and thorough work on a large number of complex perovskite-type materials, Goldschmidt introduced the concept of the *tolerance factor t* as a measure of how easy the structure adjusts to a combination of different types of cations on *A*- and *B*-sites:

$$t = \frac{R_a + R_x}{\sqrt{2}(R_b + R_O)} \tag{1.2}$$

In this equation, R_a, R_b and R_O are the ionic radii of A- and B-cations and an oxygen, respectively (see Fig 1.4) [38, 39]. For perovskite structures it is important that the tolerance factor stands between 0.8 and 1. In complex-oxide perovskite-type relaxor materials, at least one ferroelectrically active cation is included, usually a *d*-shell transition metal ion on *B*-site. In Pb-based perovskite-type relaxors, both *A*- and *B*-sites contribute to the ferroelectric behaviour, because Pb^{2+} has the affinity to form lone-pair electrons, i.e. to shift aside from the centre of the cubo-octahedral cavity and hence, it is ferroelectrically active.

The perovskite-type structure of $AB'_{0.5}B''_{0.5}O_3$ type tolerates a modification of the degree of 1:1 cation order in the *B*-sublattice via thermal annealing at temperatures higher than T_B. The 1:1 cation order considers the two alternating types of cations in the *B*-sublattice. The degree of chemical order in the *B*-sublattice strongly affects the dielectric properties [40-42]. Completely ordered PST is a normal ferroelectric material, while *B*-site chemical disorder induces relaxor behaviour in PST [43]. Materials with a complete 1:1 *B*-site order are either normal ferroelectrics or anti-ferroelectrics, whereas partially or entirely chemically *B*-site disordered materials usually show relaxor behaviour.
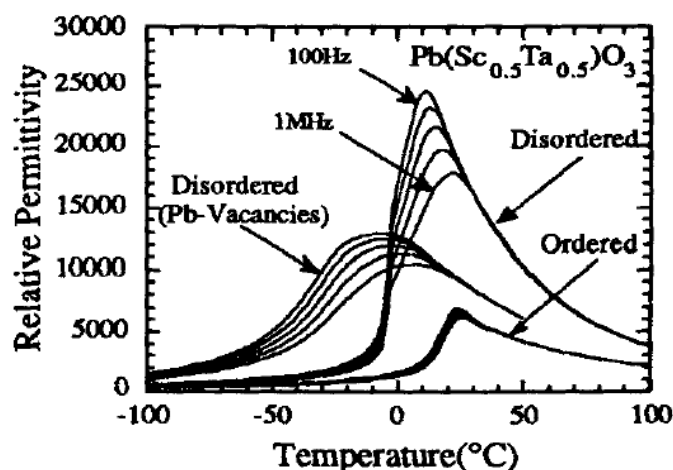
Figure 1.5 Relative permittivity of PST ceramics with different degree of *B*-site order, measured at different frequencies, after Chu et al [43].

1.4 Theoretical concepts of relaxor behaviour

In relaxor materials, the average structure remains virtually undisturbed over a considerable temperature range while various types of changes occur on the nano-scale level. Mechanisms of the nucleation and temperature evolution of the local polar nano-scale domains and the relaxor behaviour itself are still controversial. There are two general theoretical concepts about the relaxor behaviour: the dipolar glass approach and the random-field-domain stabilized approach. According to the dipolar glass approach, relaxor materials comprise polar nano-domains embedded within a paraelectric matrix whose dipole moments freeze on cooling. The latter proposes that the existence of size-restricted nano-domains is due to local random electric fields appearing from compositional fluctuations.

One of the oldest and simplest explanation was proposed by Smolenskii based on his investigations of $PbMg_{1/3}Nb_{2/3}O_3$ [44]. The compositional fluctuations on *B*-sites influence the formation of local polar nano-domains, each undergoing phase transition at a different T_C.

In this case, T_m represents the mean Curie temperature of all local transitions. Local covalent bonding between *2p* oxygen electrons and *B*-site cations additionally affects the Curie temperature T_C of individual nano-domains. As a result, the transformation between the paraelectric and ferroelectric state appears diffuse and smeared. This was the reason why in the early days relaxors were named "ferroelectrics with diffuse phase transition" [45]. The model given by Smolenskii considers the chemical disorder as a primary driving force in PNR nucleation [46,47]. However this approach cannot explain the strong suppression of $\varepsilon(T)$. A superparaelectric model was proposed by Cross [48] by analogy with the superparamagnetic state in which spin clusters nucleate as an attempt to remain stable against the thermal motion and their random interaction gives rise to a magnetic relaxation. The polar nano-regions act like individual dipoles and are switching between the equivalent orientation states relative to the local symmetry. Above T_m these polar regions have a dynamic orientational disorder. However, the directions of the individual local polarizations are *not random* but with preferential orientation along the possible polar crystallographic directions, leading to grouping and growth of the regions [9, 36]. Bokov further develops this model by suggesting that the appearance of the polar-nano regions is followed by local elastic and electric fields increasing the total energy of the system [49]. Such local anomalies are initiated by individual atomic shifts but stabilize with the nucleation of first PNRs at T_B. Upon cooling, the number of initial PNRs increases but a significant growth happens at temperatures close to T_C. Bokov's theory does not take into account mutual interactions between the PNRs at low temperature, which is not negligible and can lead to the formation of a glass-type phase at T_f [50]. The main disadvantage of glass-type models is that they all have difficulties explaining the crossover from relaxor to ferroelectric state under the external electric field.

The second theoretical approach assumes that the crystal consists of small nano-sized ferroelectric domains separated by domain walls of thickness comparable to the size of the ferroelectric nanodomains. This was established based on theoretical work of Imry and Ma [51] and supported by the quenched *random-field* model, developed by Westphal, Kleemann and Glinchuk [52, 53]. According to Imry and Ma, in a system with a continuity of a certain order parameter, a second-order phase transition should be destroyed by quenched random local fields. Similar to the concept of PNRs, the crystal is represented as a system of reorientable dipoles, embedded in a highly polarisable "host lattice" and the interaction between the dipoles is random, indirect and mediated by the host. Eventually, random dipoles lead to a uniformly directed local field and FE long-range ordering at low temperature. The disadvantage of this concept lies in its inability to explain the dynamics of polar nano-regions near and above T_C.

One should mention that the glassy-models assume potential barriers between the different orientation states as a result mainly of local *elastic fields*, while the random-field-

domain stabilized models are based mainly on the existence of local electric fields due to the *charge imbalance.*

1.5 High pressure studies on relaxors, state of the art

As pointed out in the previous chapter, the exact mechanism of the formation and evolution of the relaxor behaviour, as well as the transition between the relaxor ferroelectric (RFE) and normal ferroelectric state (nFE) is not well understood and remains controversial. High-pressure studies can help elucidate whether the primary factor in the formation of the relaxor state is related to the elastic fields or due to with the existing charge imbalance.

In his pioneering work, Samara was the first to introduce investigating pressure-induced changes in the relaxor properties, combining dielectric spectroscopy with the high-pressure technique. Hydrostatic pressure is considered to be a "cleaner" variable [54], influencing only the balance between the long- and short-range forces. In his work, the focus was mainly on investigating *A*- or *B*-side doped Pb-based perovskite relaxor ceramics such as La-modified $PbZr_{1-x}Ti_xO_3$ (PLZT) [54, 55], Ba- and Bi-substituted $PbZr_{1-x}Ti_xO_3$ [56], PSN [57], $PbMg_{1/3}Nb_{2/3}O_3$ (PMN) [58] or Ca-doped single crystal $KTa_{1-x}Nb_xO_3$ [59]. Due to the complexity of the experimental setting that combined the dielectric measurement at varying frequency and temperature with pressure, the pressures at which these compounds were studied never exceeded 2 GPa.

The results of the behaviour of the ε between ambient pressure and 2 GPa indicated that pressure frustrates the long-range coherence of ferroic species and favours the relaxor state. Samara suggested that (i) the pressure-induced nFE – RFE crossover is a general phenomenon observed in many soft-mode perovskites, (ii) the pressure favours the RFE state [59]. Based on the results on PSN, obtained at moderate pressure (< 2 GPa) it was assumed that at higher pressures the relaxor ferroelectric state would disappear, leaving the system in a pure paraelectric state (see figure 1.6).
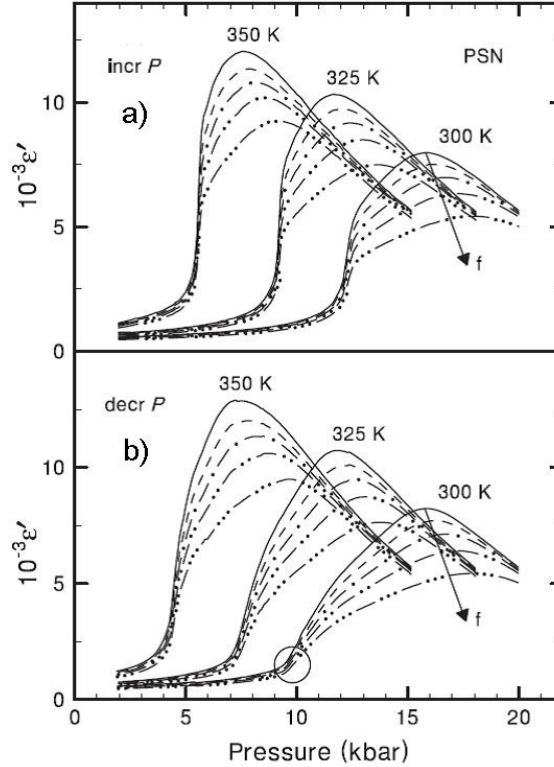
Figure 1.6 Isotherms of ε' vs pressure showing the influence of a) increasing and b) decreasing pressure on PSN ceramic (after [59]) – 1 kbar = 0.1 GPa.

In relaxors the local structure strongly deviates from the average structure and therefore methods sensitive to local structural transformations have to be used to study pressure-induced structural changes. Raman spectroscopy and X-ray diffuse scattering (XDS) are very appropriate techniques for this purpose and enable new insight into the pressure-induced structural changes on the local level, e.g. on polar nano-domains [60]. Additionally, the diamond anvil cell technique allows for studies at pressures much higher than 2 GPa, achieved in high-pressure dielectric measurements. Changes in the phonon modes are sensitive indicators of pressure-induced local structural transformations. The pressure evolution of the diffuse X-ray scattering, which originates from coherent cation off-centred shifts correlating on an intermediate-range scale but insufficient to produce Bragg reflections, is also informative of the development of polar nano-regions upon external elastic field.

The work of Kreisel et al [60-66] revealed that the different perovskite-type relaxors $Na_{0.5}Bi_{0.5}TiO_3$ (NBT) and $PbMg_{1/3}Nb_{2/3}O_3$ exhibit similar pressure-induced changes, which go along with the suppression of B-site cation off-centre displacements and a corresponding pressure evolution of the internal octahedral modes. Additionally, in both cases the XDS disappears under pressure. In PMN, which is a canonical relaxor, the suppression of the XDS above 4.5 GPa points towards the diminishing differences between the local and the

12

average structure. Based on pressure-induced changes in the classical ferroelectrics such as BaTiO$_3$, the simplest explanation of the XDS suppression in relaxor-material, is associated with a phase transition of the whole system into cubic symmetry. On the other hand, such a transition would lead to the total disappearance of the Raman activity at pressures above 4.5 GPa, which is however not the case (see figure 1.7).

The probable explanation implied by Chabaane et al [65], combining both the Raman and XDS data considers the suppression of the diffuse scattering as a consequence of the weakening of the local strains in PMN, when the local domains and the initially cubic matrix adopt the same non-cubic symmetry. The authors assumed that the high-pressure long-range ordered phase is anti-ferroelectric with a doubled unit cell corresponding to the a face-centred cubic $Fm\overline{3}m$ prototype structure [62]. Therefore, the
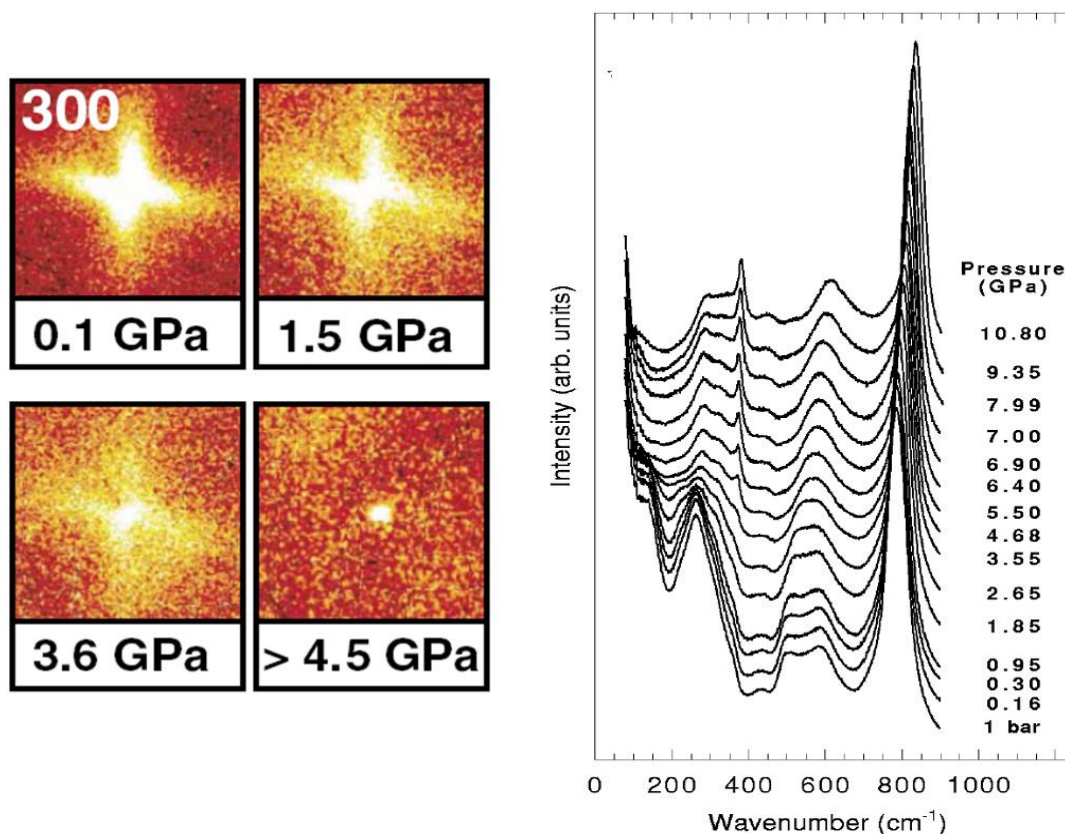
Figure 1.7. Suppression of the diffuse scattering of the (300) reflection in PMN might indicate long-range ordering in the cubic symmetry if the Raman signal of PMN did not prove that the structure at high-pressures is far from the paraelectric state, after [61, 65].

previous assumption based on dielectric measurements that pressure favours the segmentation of long-range coherence of the ferroic species and leads to a cubic structure seem to be oversimplified. Additionally, a considerable difference between the pressure- and

13

temperature-induced structural evolution of the relaxor materials became apparent. Experiments at high-pressure enabled a new approach in studying the mechanism of the relaxor behaviour.

2. Objectives

The aim of this study is to analyze pressure-induced local structural changes in a series of model Pb-based perovskite-type relaxor compounds in order to elucidate the energetically preferred atomic arrangements, stable under mechanical load, and to clarify the role of local elastic fields versus local electric fields for the development of pressure-induced ferroic ordering in this type of materials. For this purpose, Raman spectroscopy in the pressure range up to 10 GPa was applied to

- stoichiometric $PbSc_{0.5}Ta_{0.5}O_3$ (PST) and $PbSc_{0.5}Nb_{0.5}O_3$ (PSN)
- Ba- and Bi-doped PST and PSN
- a solid solution of PST and PSN as well as Ba-doped PST-PSN.

$PbSc_{0.5}Ta_{0.5}O_3$ (PST) and $PbSc_{0.5}Nb_{0.5}O_3$ (PSN) represent model relaxor systems of type $AB'_{0.5}B''_{0.5}O_3$ (see Fig.2.1), with ferroelectrically active cations in both A- and B''-sites (Pb^{2+} and Ta^{5+}/Nb^{5+}, respectively). The ionic radii of octahedrally-coordinated Ta^{5+} and Nb^{5+} are identical ($r_{Ta} = r_{Nb} = 0.64$ Å) and, hence, the tolerance factors of the two compounds are the same. Besides, the stoichiometry of both compounds allows for the variation of the degree of chemical 1:1 B-site order, which on a local scale is typical of all Pb-based relaxors. It is known that Sc and Ta cations tend to order easier than Sc and Nb do [72,122], which should result from the larger B-site mass and force-constant difference ($\Delta m_B = m_{B''} - m_{B'}$ and $\Delta K(B-O) = K(B''-O) - K(B'-O)$) for PST as compared to PSN. At ambient pressure, T_m for both compounds is close to room temperature and thus, the structure of both PST and PSN is abundant of polar nanoregions, which significantly facilitates the detection and analysis of pressure-induced structural transformations.

Ba is a two-valent cation, whose ionic radius is larger than that of Pb^{2+} in a 12-fold coordination ($r_{Ba} = 1.61 > r_{Pb} = 1.49$). In addition, the outermost electron shell of Ba is isotropic, i.e., in contrast to Pb^{2+}, Ba can not form lone-pairs and does not tend to off-centre displace. The incorporation of Ba into the A-site cannot lead to charge imbalance because Ba is isovalent to Pb^{2+}, but due to the differences in the outermost electron shell and the ionic radius, it will give rise to additional local elastic fields.
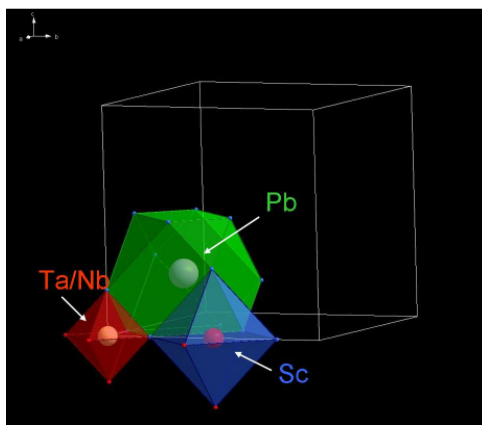
Figure 2.1 Coordination of the cations within the $Fm\bar{3}m$ symmetry. *A*-sites are occupied by Pb atoms in the middle of the cubooctahedral void, while Sc on *B'*- and Ta or Nb *B"*-sites create two types of octahedra.

Bismuth is a three-valent element and the outermost electron shell is identical to that of Pb^{2+} and, hence, Bi^{3+} has the same affinity to form lone pairs and off-centre shifting as Pb^{2+} does. At the same time, the ionic radius of Bi^{3+} is slightly smaller than that of Pb^{2+} and therefore the incorporation of Bi^{3+}, which is aliovalent to Pb^{2+}, into the A-site results in charge imbalance and local electric fields, without causing significant local elastic strains in the structure. Therefore, by comparing Ba-doped PST with a moderate degree of chemical B-site order with pure PST having a very low degree of B-site order, one can analyze the effect of local elastic fields versus B-site related charge imbalance, whereas by comparing Ba- and Bi-doped PSN with a complete chemical B-site disorder, one can analyze the effect of local elastic fields versus A-site related charge imbalance.

The solid solution of PST-PSN has two competing ferroelectrically active *B"*-site cations. Therefore, the comparative analysis of the series PST, PST-PSN and PSN as well as PST-Ba, PST-PSN-Ba and PSN-Ba can give further insight into the role of local elastic/electric fields associated with the A-site chemical disorder versus those associated with the B-site chemical disorder

The temperature-dependent structural changes of the same compounds used in this study have been thoroughly studied by means of Raman spectroscopy and XRD [67-76]. No high-pressure structural studies on PST, PSN, their solid solutions and A-site doped analogues have been performed prior to this study. The only previous investigation of $AB'_{0.5}B''_{0.5}O_3$-type relaxors has been restricted to dielectric measurements of highly ordered ceramic PSN samples at moderate pressures up to 2 GPa [59]. Two anomalies in the dielectric response have been observed and were interpreted as related to a spontaneous ferroelectric phase transition in the ordered regions while the second corresponds to the relaxor behaviour of the material. Since the intergrain strains are abundant in the ceramic samples, in order to investigate more precisely the pressure-induced structural transformations in the bulk and the interactions between the incipient ferroic species, this work focuses on the single-crystal samples.

3. Methods

3.1. Raman spectroscopy

3.1.1. The Raman effect

White light is a mixture of electromagnetic waves in the range from 400 to 700 nm (see fig 3.1). As an electromagnetic wave, It consists of electric and magnetic field components which oscillate in phase perpendicular to each other and perpendicular to the direction of energy propagation.
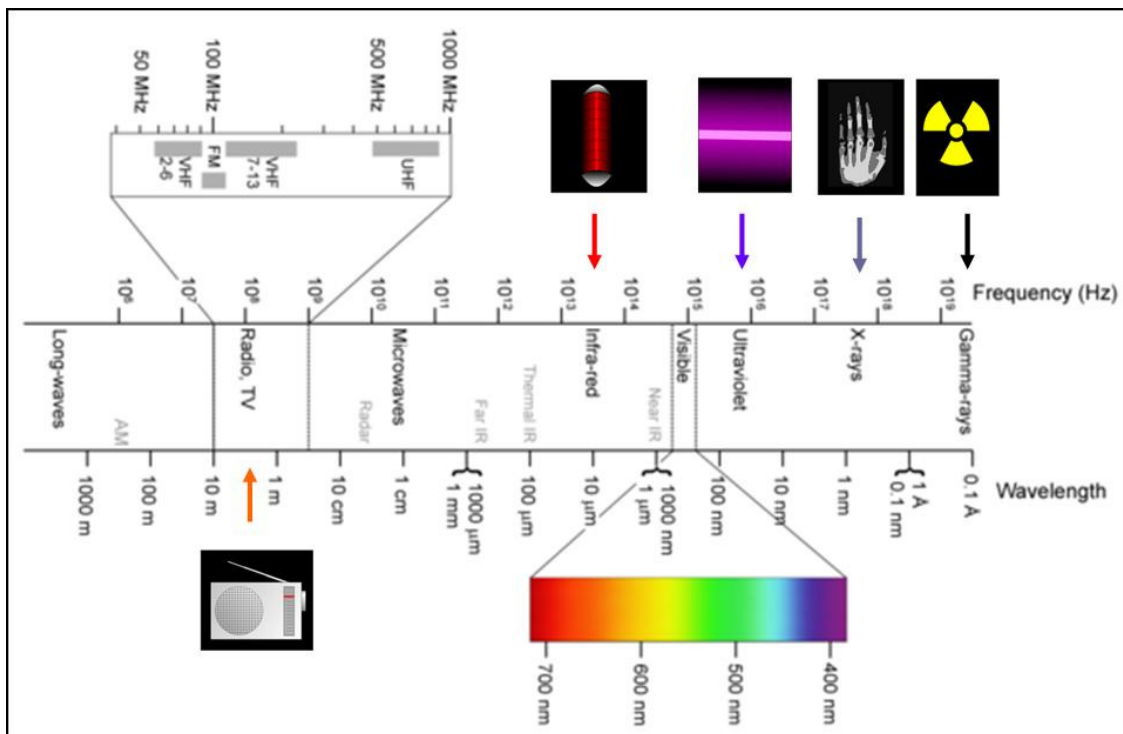
Figure 3.1 The complete electromagnetic spectrum.

The shortest distance between the two successive points oscillating in phase represents the *wavelength* – λ (see fig 3.2), measured by units of length, usually μm, nm or Å. The frequency f is defined as the number of oscillations per second, i.e.

$f = \dfrac{1}{\tau}$, where τ is the period of oscillation of the electric/magnetic field. The units of

v is $Hz \equiv \dfrac{1}{s}$. The angular frequency ω is defined as $\omega = 2\pi v$.
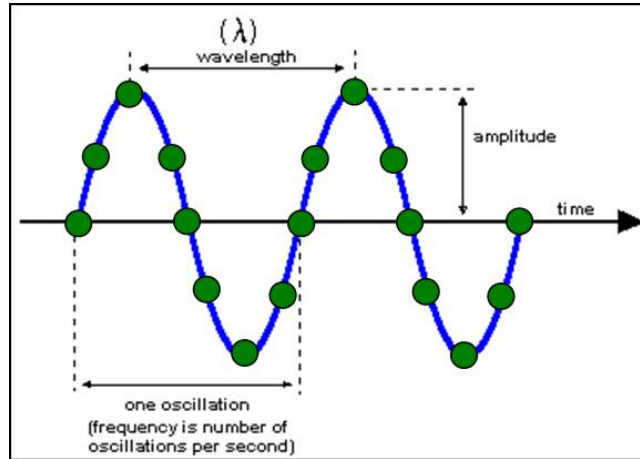
Figure 3.1 Sketch of a plane wave.

In spectroscopy, the frequency is commonly given in wavenumbers $\tilde{v}$, inversely related to the wavelength. It is a measure of the number of repeating units of a propagating wave (the number of times a wave has the same phase) per unit of space.

$$\tilde{v} = \frac{v}{c} = \frac{1}{\lambda} \Rightarrow [\tilde{v}] = cm^{-1} \qquad (3.1)$$

Due to the wave-particle dual nature of electromagnetic radiation, a quantum of light is represented by a *photon*, which has a quasi-momentum *p*:

$$p = \frac{hv}{c} \qquad \text{or} \qquad \mathbf{p} = \hbar\,\mathbf{k} \qquad (3.2)$$

where h is the Planck's constant (h =6.626069 ·10^8 m/s) and $\hbar = \dfrac{h}{2\pi}$, $\mathbf{k}$ is the

wavevector with magnitude of $\dfrac{2\pi}{\lambda}$ and the direction of the vector indicates the

direction of wave propagation.

The energy of electromagnetic radiation is:

$$E = \hbar\omega \qquad (3.3)$$

Bonded atoms vibrate at frequencies between 10^{12} and 10^{14} Hz. The exact frequency of the vibrations is governed by the interatomic force constants K and the reduced mass m . In the case of a monoatomic chain composed of identical atoms

18

with a mass m, interacting between one another with a force constant K, the frequency ω is:

$$\omega = \sqrt{\frac{K}{m}} \qquad (3.4)$$

In a crystal comprised of **N** atoms in the primitive unit cell, vibrating in **3D** space, $3N$ degrees of freedom are possible with a finite number of normal states. Thus the system of N atoms vibrating in 3 directions can be replaced by a system of $3N$ normal phonon modes. The phonons represent quanta of vibrational energy in crystals and similarly to photons, they are characterized by frequencies and wavevectors **k** of the corresponding normal elastic wave.

$$N \text{ atoms} \times \mathbf{3} \text{ dimensions} \longleftrightarrow \mathbf{3N} \text{ phonons}$$

Out of the $3N$ symmetry allowed phonons, three are acoustic and $3N$-3 are optical phonons (see figure 3.3). Atoms vibrate out of phase, leading to an induced dipole moment that can interact with the electric field of light.
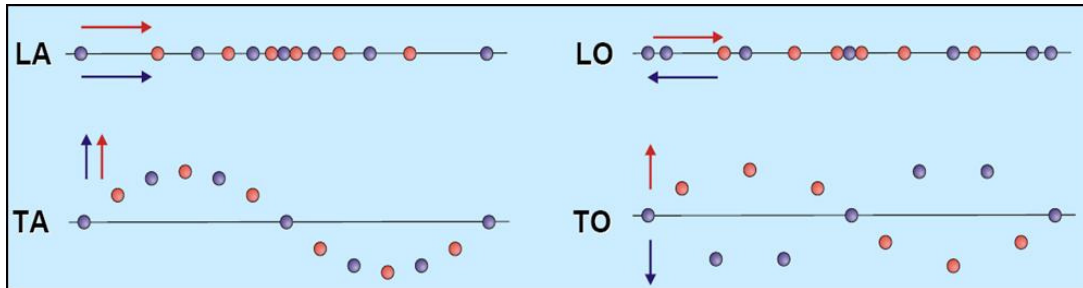
Figure 3.3 Propagation of phonons in a diatomic chain – LA – longitudinal acoustic, TA – transverse acoustic, LO – longitudinal optic and TO – transverse optic.

The phonon wavevectors are actually translational vectors in the reciprocal space. When $\mathbf{k} = \mathbf{0}$ it refers to the centre of the *Brillouin zone*: the Wigner-Seitz primitive cell in the reciprocal space.

Phonons can be further differentiated into longitudinal and transverse depending on if the elastic wave polarization (the direction of atomic displacements) is respectively parallel or perpendicular to the wave propagation. The interaction between phonons and photons lead to absorption during scattering processes. Absorption processes occur if the incident radiation is within the IR spectral range,

19

since in this case the photon energy is close to the typical phonon energies. In the case of near-IR/visible/near-UV indicent radiation, the excitation of atomic vibrations through a simple absorption of incident light is not possible due to the substantial frequency difference, however the oscillating electric field of an incident light wave can interact with the electronic cloud around the vibrating atomic nuclei. Such generated energy is immediately released through a diffuse elastically scattered light with the same frequency as the incident beam of light. The light scattered with no change in energy is known as the elastic 'Rayleigh scattering' ($E_i = E_s$). In addition light can be inelastically scattered. The energy of the inelastically scattered light is either higher or lower in value relative to the elastic scattering and is shifted from the Rayleigh signal (see figure 4.5), towards higher frequencies in the case of the *Stokes* scattering ($E_s = E_i - \hbar\omega_s$) or towards lower frequencies in the case of the *anti-Stokes* scattering ($E_s = E_i + \hbar\omega_s$). Inelastic light scattering from the optical vibrational mode is the *Raman effect*. It was first reported by C. V. Raman and K. S. Krishnan [77], and independently by G. Landsberg and L. Mandelstam, in 1928. Raman received the Nobel Prize in 1930 for his work on the scattering of light. Due to the difference in the wavevectors, only phonons in the vicinity of the Brillouin zone centre can scatter visible photons.

The Raman signal intensities are strongly temperature dependent as the occupation of phonon states depends on *T*. In order to compare spectra collected at different temperatures after the background noise subtraction, raw spectra are corrected for the *Bose-Einstein occupation factor n :*

$$1^{st} \text{ order Stokes signal: } I_{reduced} \propto \frac{I_{measured}(\omega)}{(n(\omega)+1)} \qquad (3.5)$$

$$1^{st} \text{ order anti-Stokes signal: } I_{reduced} \propto \frac{I_{measured}(\omega)}{n(\omega)} \qquad (3.6)$$

where $n(\omega) = \dfrac{1}{e^{\hbar\omega/kT}+1}$, k is the Boltzmann's constant and *T* is the temperature in kelvins. First order process mean that one photon interact with one photon only. Such
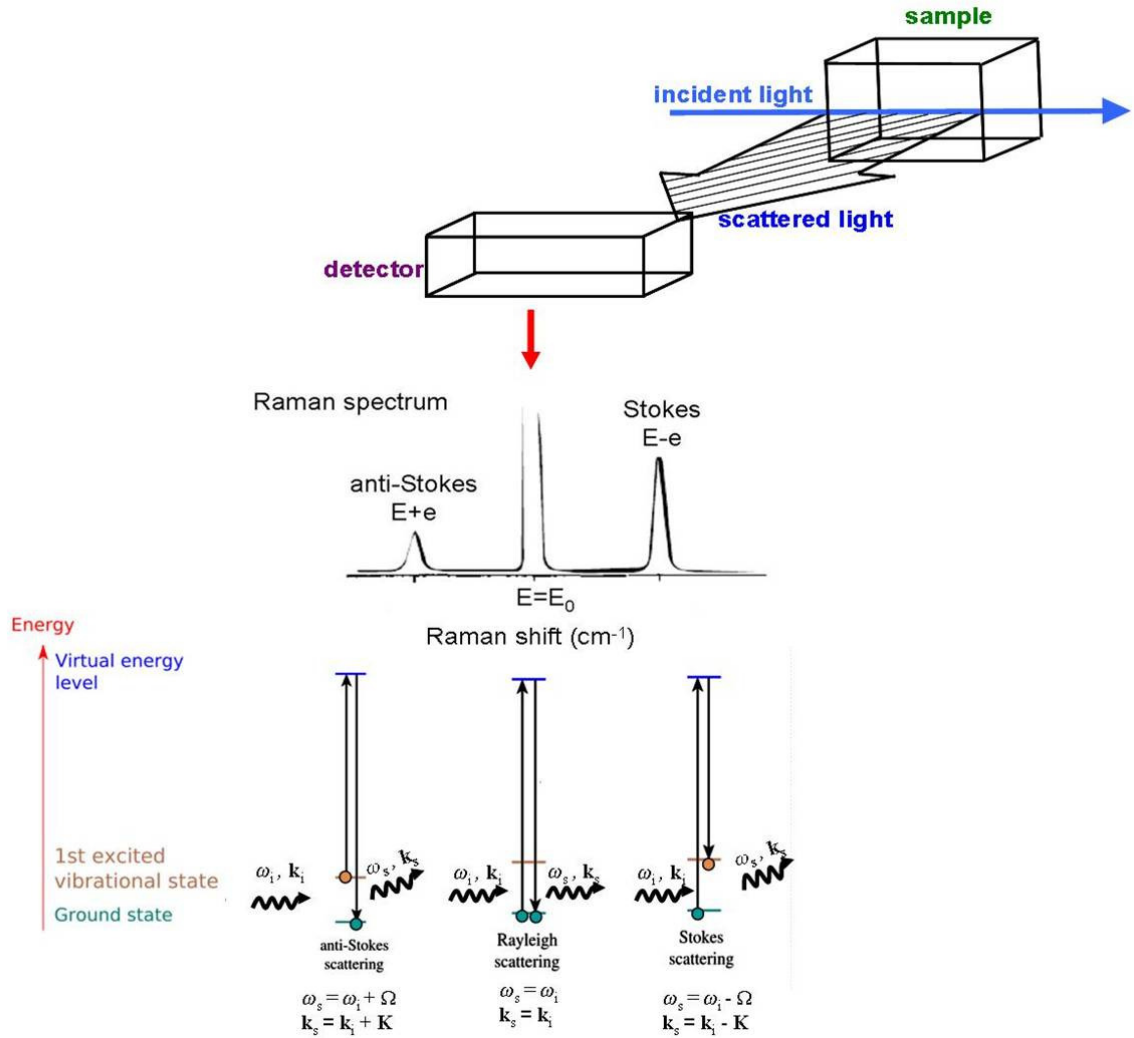
Figure 3.4 Scheme of the Raman effect – incident laser beam passing through the sample, getting scattered, detector capturing the scattered signal which is analysed in spectrometer (not included in the picture) into a Raman spectrum relative to the energy level, shown on the bottom part of the diagram.

reduced intensities of Stokes and anti-Stokes signals can be used for temperature determination by a simple approximation:

$$\frac{I_{anti-Stokes}}{I_{Stokes}} \approx e^{-(\hbar\omega/kT)} \tag{3.7}$$

By considering phonon-phonon interactions, one can establish a correlation between the change in phonon frequencies and unit-cell volume. The coefficient of proportionality is called the *Grüneisen parameter* γ_G. In the case of $1D$ monoatomic crystals

$$\gamma_G = \frac{\dfrac{\Delta\omega}{\omega}}{\dfrac{\Delta a_0}{a}} \qquad (3.8)$$

In the case of 3*D* crystals the Grüneisen parameter is a second rank tensor:

$$\frac{\Delta\omega}{\omega} = -\overline{\overline{\gamma}} \bullet \overline{\overline{S}} \qquad (3.9)$$

where **S** is a stress tensor.

The origin of the Raman spectra is closely related to the change in the polarizability due to the deformation of the electronic shell. Polarization **P** (dipole moment per unit cell):

$$\mathbf{P} = \mathbf{\alpha}.\mathbf{E}, \qquad (3.10)$$

where **α** is the *polarizability tensor*.

For small vibration amplitudes, the polarizability α can be represented as a Taylor series generalized via nuclear displacement q :

$$\mathbf{\alpha}(q) = \mathbf{\alpha}_0 + \sum \frac{\partial \mathbf{\alpha}}{\partial q_k} q_k + \ldots \qquad (3.11)$$

In eq. 3.11, α_0 represents the polarizability in the equilibrium position. Elastic (Rayleigh) scattering occurs while the linear term describes the inelastic (Raman) scattering. If for a given mode $\left(\dfrac{\partial \mathbf{\alpha}}{\partial q_k}\right) \neq 0$ this mode is Raman-active and gives rise to a excitation in the Raman spectrum.

Induced dipole moment due to the change in the atomic positions results in infra-red activity. Raman-active vibrations are symmetrical, while IR-active modes are anti-symmetrical with respect to the symmetry elements. Simultaneous IR and Raman activity is only possible in non-centrosymmetric structures. The Raman or IR activity of crystal phonon modes is regulated by symmetry with certain "selection rules" related to the space group and the occupied Wyckoff positions.
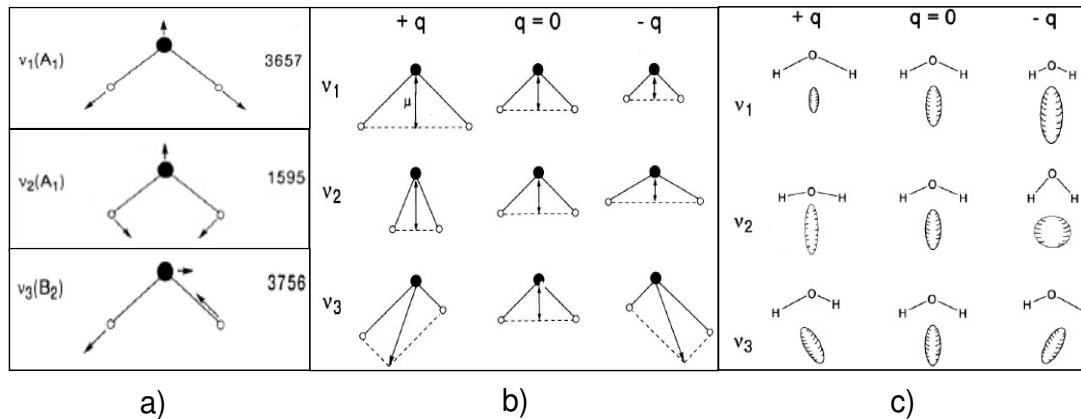
Figure 3.5 Example of the vibrations of a water molecule: a) the three normal vibrational modes of H_2O; b) anti-symmetric vibrations are IR active due to the change in the dipole moment induced by nuclear displacements; c) symmetrical vibrations are Raman-active due to the change in size, shape, and/or orientation of the polarizability tensor; after [78]

Normal phonon modes in crystals correspond to the irreducible representations of the symmetry elements and are designated by the Mulliken symbols. The symbols consist of:

1. capital letter – gives information on the type of degeneration – all vibrations have the same phonon energy (frequency):
   - A and B – **1D** representations - single (non-degenerate) mode while A-modes are symmetric and B- are antisymmetric in respect to the principle rotation axis;
   - E – **2D** representations - doubly degenerate mode, appearing only in uniaxial crystal
   - F (T) - **3D** representations - triply degenerate mode (sometimes known as T) – appearing only in cubic crystals.

2. subscripts g or u – describing whether relative to $\bar{1}$ the mode is:
   - symmetric – g (gerade - even);
   - antisymmetric – u (ungerade - odd).

3. superscript ' or " – describing whether the mode is symmetric or anti-symmetric relative to the mirror plane.

4. subscript numbers 1 or 2 – describing whether the mode is symmetric or anti-symmetric relative to the additional symmetry element (mirror planes or axis of symmetry).

3.1.2 Instrumentation and experimental setup for this study

The Raman scattering measurements were performed using a Horiba Jobin-Yvon T64000 triple-grating spectrometer equipped with a LN_2-cooled 1028 x 256 CCD detector, using a Coherent innova® technology 90C FreD Ar^+ laser operating at $\lambda = 514.5$ nm. The output laser power was 0.135 W and a filter of crystal density 0.3 was put in the pathway of incipient beam to additionally adjust the laser power. The second intermediate slit was kept at 100 µm in all measurements. The spectral resolution achieved under these experimental conditions was approximately 2 cm^{-1}. Data were collected in back-scattering geometry with an Olympus microscope and a 50 x long-working distance objective. The acquisition time varied from 30 to 90 s depending on the strength of the signal and was performed in two loops, in order to eliminate the spikes.

At each pressure, a background spectrum was collected from a spot distant from the sample, with the same acquisition time and focusing used for collecting of the sample spectrum. In order to eliminate the artificial contribution from the medium and anvils, the as-measured background spectrum was subtracted from the sample spectrum. All spectra were corrected for the Bose-Einstein occupational factor and smoothed by the adjacent averaging method with a coefficient 3. The latter procedure did not affect the full-width-at-half-maximum (FWHM) of the measured Raman excitations.

The peak positions, FWHM and the integrated intensities were determined by fitting the spectrum profiles with Lorentzian functions. The repeatability of each individual spectral feature was verified by measuring several samples of each compound for a reliable statistic.

3.2 High-pressure experiments

3.2.1 Diamond anvil cell

Studies of materials under extreme *p-T* conditions were made possible by the combination of the diamond anvil cell (DAC) technique and the pressure calibration based on the ruby luminescence method. The principle of the diamond anvil cell is simple. The original concept has seen little changes since its original design over the years, where small culet areas of the diamond anvils induce the large pressure load, with minimal force. The primary components are (see figure 3.7):

        a. Diamond anvils

        b. Gasket

        c. Pressure medium

        d. Pressure calibrant
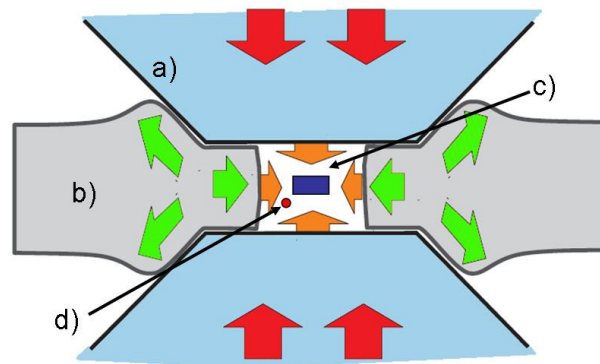
Figure 3.7 Basic scheme of a DAC containing sample: a) anvil, b) gasket with a hole, c) pressure medium with the sample (blue rectangle), d) ruby (red dot).

The use of diamond anvil cell enables the transformation of unilateral *stress* into *pressure*. Elastic stress T_{ik} results from mechanical force $\mathbf{F}_i$ directed onto a surface S_k. It is a second rank tensor with special cases:

- Uniaxial stress - $\begin{pmatrix} T & 0 & 0 \\ 0 & 0 & 0 \\ 0 & 0 & 0 \end{pmatrix}$

- Shear stress $\begin{pmatrix} -T & 0 & 0 \\ 0 & T & 0 \\ 0 & 0 & 0 \end{pmatrix}$

- Hydrostatic pressure $\begin{pmatrix} -T & 0 & 0 \\ 0 & -T & 0 \\ 0 & 0 & -T \end{pmatrix}$

The SI unit for pressure is *pascal*, while another commonly used unit is *bar*. They stand in the following proportion:

$$10^5 \text{ Pa} = 1 \text{ bar}$$
$$1 \text{ GPa} = 10 \text{ kbar}$$
$$100 \text{ GPa} = 1 \text{ Mbar}$$

The principle of DAC relies on two opposed diamond anvils for generating pressure. The reason to use diamond for anvils is two-fold: (i) it is the hardest existing material and (ii) considerably transparent to electromagnetic radiation over IR, visible, UV and X-ray (above 10 keV). Depending on the quantity and the nature of impurities, diamonds are classified into two major groups with two subgroups – see table 3.1.

Type Ia	98 % of natural diamonds. Nitrogen present in platelets, N-N pairs or 4 N atoms surrounding a vacancy, resistant to plastic deformation and good for experiments in the Mbar regions	Type Ib	~ 0.1 % of Nitrogen impurities present in the form of point defects
Type IIa	1-2 % Very pure, usually rose or with yellowish brown hue, low fluorescence and good for spectroscopic studies	Type IIb	Contain ~ 0.1 % of Al or B

Table 3.1 – Classification of diamonds according to the defects present.

Diamond impurities can easily be detected by the IR absorption spectra. Type II does not absorb in the UV and IR regions thus being better suited for the use in

spectroscopic studies. However, natural diamonds of type II are very rare and very expensive compared to diamonds of type I. For Raman spectroscopy and other sensitive optical techniques, diamonds should be pre-selected for low luminescence.
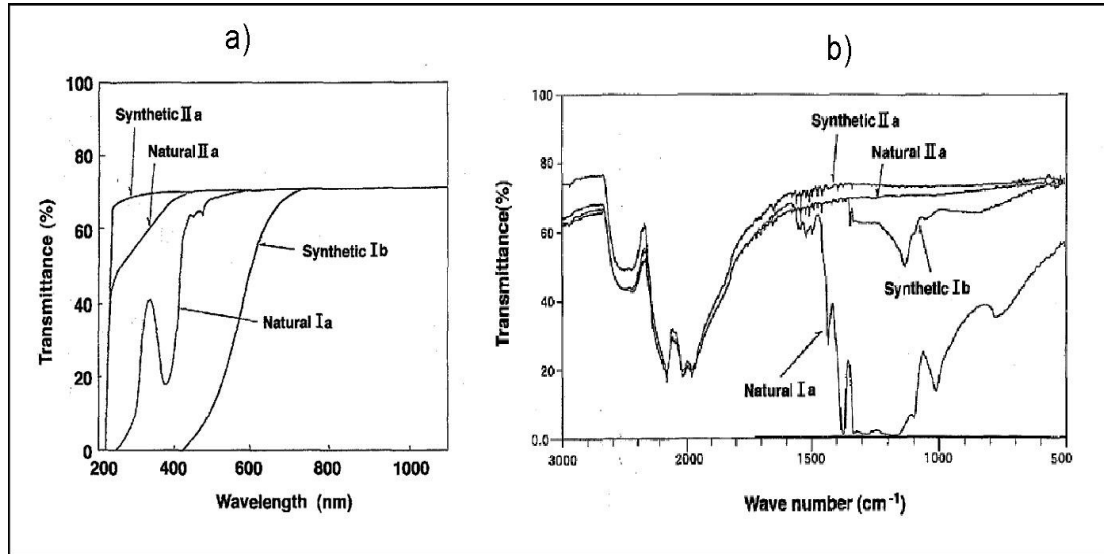
Figure 3.8 Spectra of the different types of natural and synthetic diamonds: a) ultraviolet spectra, b) IR-spectra, after Sumiya et al [79]

Defects influence not only the optical but also the mechanical properties of diamonds. The relationship between the mechanical properties of a diamond and the type is not yet thoroughly clear, but it is empirically proved that IIa diamonds are the hardest although brittle. At very high pressures in the Mbar range, diamonds of Ia type are more resistant to plastic deformations giving additional security to the experiment.

By analysing the radial cracks developed within the diamond anvils at room and low temperatures, a correlation between the critical intensity stress coefficient K_{IC} and different nitrogen defects had been established.

$$K_{IC} = \sqrt{2E\gamma_{eff}}$$ (3.13)

In equation 3.13, E stands for the bulk elastic modulus and γ_{eff} is the effective failure energy, the energy needed for creation of new crack surfaces. The increase in the failure energy with low concentration of defects is due to the bending of the crack front between neighbouring defects and thus increasing the length of the crack. At a high concentration of defects the crack front becomes flat because of the

27

overlapping fields of elastic stress existing around the defects which stops it from growing. Maximum values for K_{IC} occur for Ia type, and minimal for IIb [80].

The most abundant diamonds on the market are of the modified *brilliant cut*[1]. The brilliant cut has been in use since the 17th century but received its present design in the 19th century when Marcel Tolkowsky calculated the best possible angles for enhancement of *brilliance* (the amount of white light reflected) and *fire* (flashes of spectral colours). The original Tolkowsky cut is very rare and an improved *modern brilliant cut* is used instead (see fig 3.9).
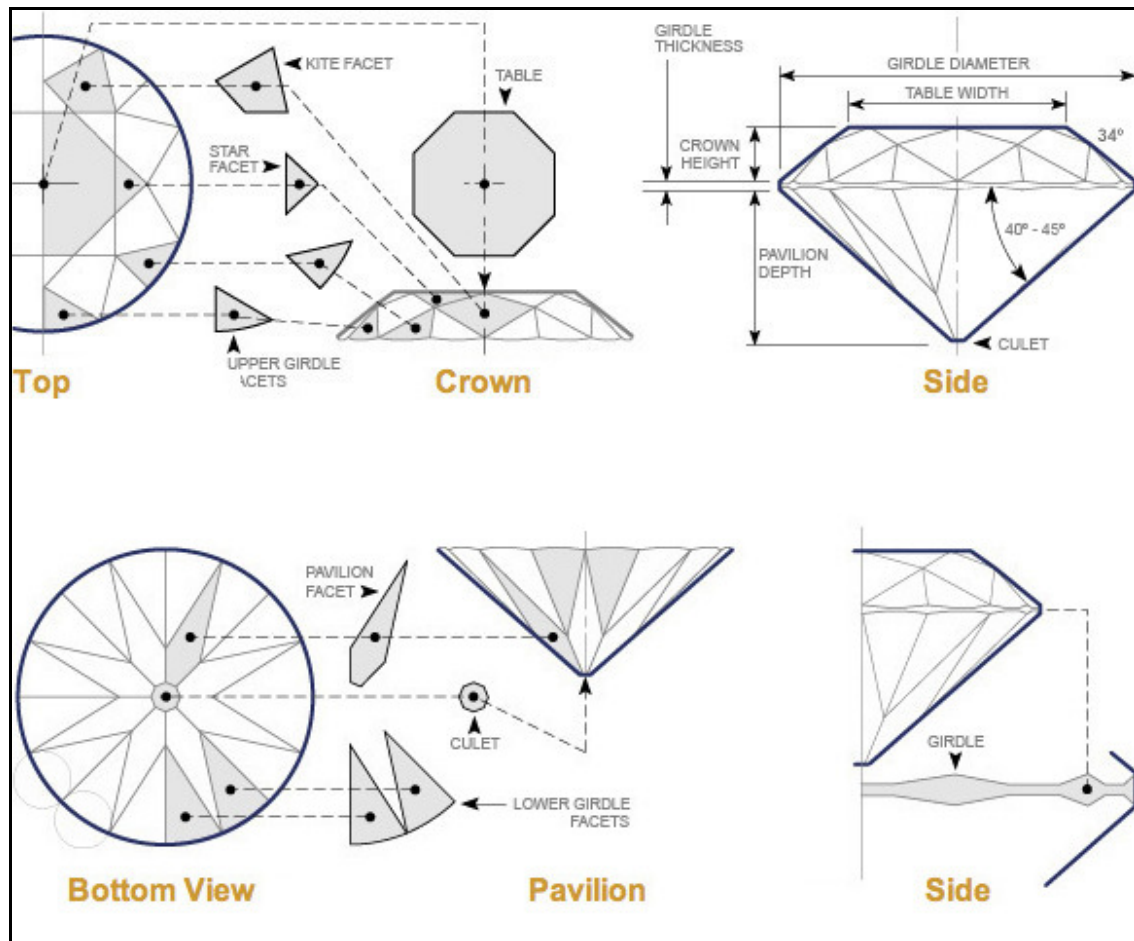
Figure 3.9 The modern brilliant diamond cut (source – www.DeBeers.com)

For the purpose of high-pressure experiments, diamonds with the brilliant cut have an enlarged culet surface. The brilliant cut suffers large stress on its girdle area, resulting in instability at pressures above 50 GPa. The Drukker and Boehler-Almax

---

[1] Cut of a diamond represents the number and type of facets applied by polishing.

diamond cut (figures 3.10a and 3.10b, respectively) are more reliable for the use in DAC due to different table-girdle-pavillion ratios (see figure 3.9 for the designation of the diamond facets). For experiments in the Mbar region, culet surfaces should be additionally modified to withstand large pressure loads by redistribution to the additional sideways facets (figure 3.10c). Such a modification is known as the culet *bevelling*.
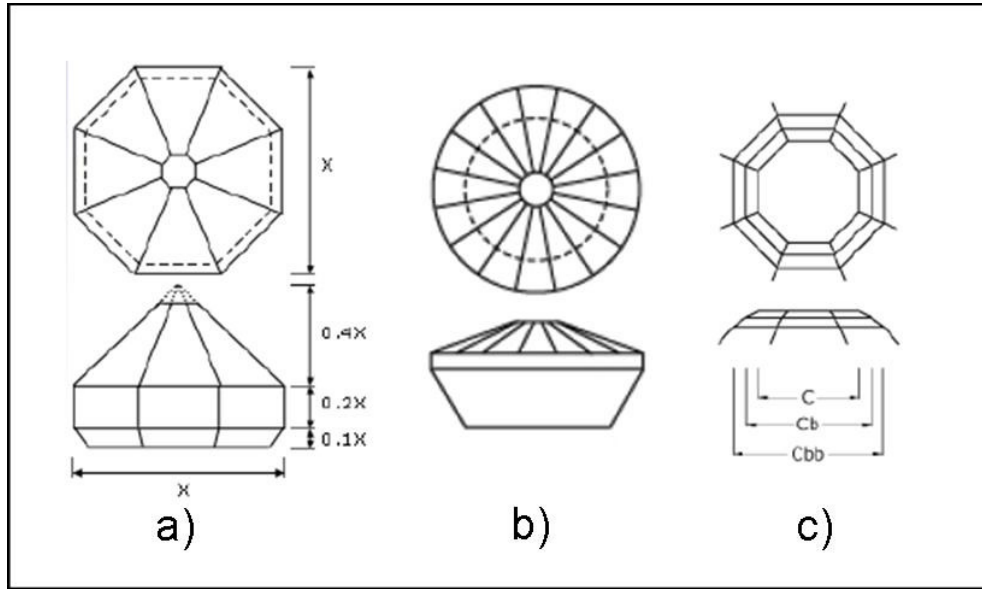
Figure 3.10 a) 8-sided Drukker cut, b) 16-sided Boehler-Almax cut with reduced thickness and c) double-bevelled culet.

For all DAC anvils it is fundamental to establish the upper pressure limit they can achieve and withstand during the experimental cycle. The maximum pressure is related to the culet diameter (see fig 3.11). The culet-pressure ratio can be calculated, knowing the mechanical properties of the diamond material and depending on the type of dislocations:

$$\overline{P}_0 = \frac{2}{1-2v}\sqrt{\frac{2\gamma E}{\pi\left(1-v^2\right)c_f}} \qquad (3.14)$$

In this equation, $\overline{P}_0$ represents the mean pressure under an indenter before the brittle failure, v is the Poisson ratio, E is the bulk elastic modulus, γ represents the surface energy and c_f is a characteristic size of defects developed [81-83].
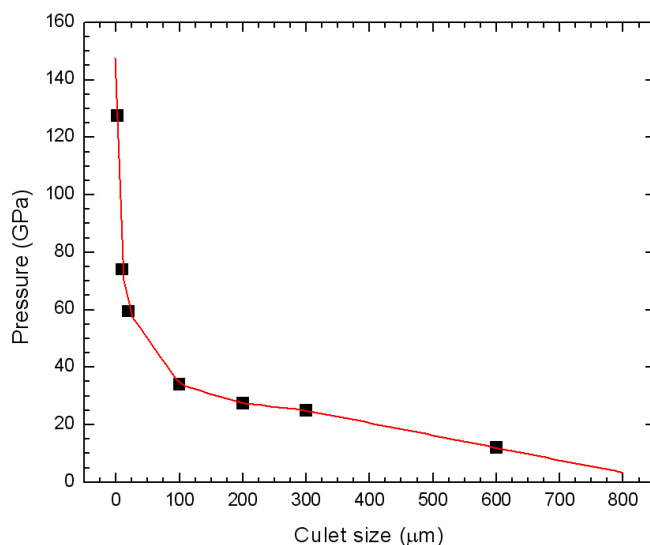
Figure 3.11 'Pressure vs culet diameter' diagram shows maximal working pressure achievable by respective culet diameters for brilliant cut diamonds (curve is based on experimental tests).

The diamond anvils are isolated from getting into a direct contact during the experimental run by a thin gasket. The gasket also embeds the actual pressure chamber: a hole at the middle of the gasket, containing the sample, pressure transmitting medium and the pressure calibrant. The gasket is a metal foil of thickness between 250 to 300 µm and with elastic properties consistent with the experimental requirements, ensuring stability of the culets during the pressure loading. The materials most commonly used are stainless steel, Inconel Ni-Cr-Fe alloy, tungsten or rhenium. Stainless steel gaskets are readily available, cheap and easy to drill while rhenium and tungsten are more robust and able to withstand experiments in the Mbar range, or high pressure/high temperature experiments. In order to avoid plastic deformation during the experiment, the gasket is preindented prior to the experiment to the thickness corresponding to the desired maximum pressure or slightly more. The compression of the gasket should not exceed 70% of the initial gasket thickness. Once indented, the gasket is drilled in the middle of the indented area (fig 3.12). There are different techniques used for drilling. Stainless steel can be drilled mechanically, unlike tungsten or rhenium gaskets. The downside of this cheap and fast method is poor quality of the drilled holes. Spark eroding ensures a clean hole with no micro-cracks in either of the metal gasket materials. Drilling by laser ablation ensures even better quality gasket holes, regardless of the

gasket material. A perfect gasket hole improves the stability of the experiment and lowers the risk of gasket failure at high pressure loads.
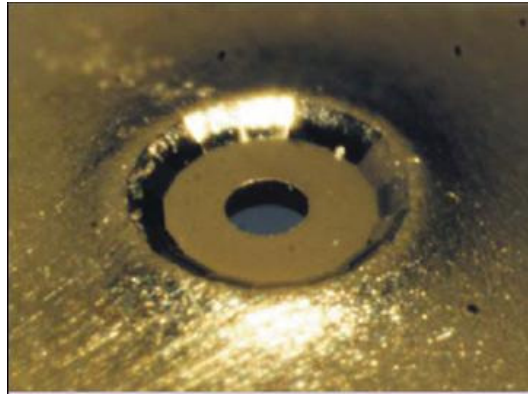
Figure 3.12 Spark-eroded gasket yields a perfect hole.

The size of the hole depends on the size of the culets and the type of pressure-transmitting medium. For the purposes of gas-loading the volume of the pressure chamber should be small, especially in the case when the gas is not cryogenically loaded. In average, the diameter of the hole should not exceed 60% of the culet diameter. The size of the sample should be proportional to the gasket hole. The maximum experimental pressure and the size of the sample stand in inverse proportion since the higher the pressure, the smaller the volume of the sample. Usually, the sample thickness should be around 60% of the gasket thickness. For recommended pressure-sample relations see table 3.2.

Pressure	10 GPa < p < 30 GPa	30 GPa <p <50 GPa	50 GPa < p
Sample thickness	~ 40 µm	~ 20 µm	< 15 µm
Sample diameter	~ 150 µm	50 to 70 µm	~ 30 to 50 µm

Table 3.2 Recommended sample dimensions with respect to the maximum working pressure.

Depending on the type of *force-generating mechanisms*, there are two main groups of DAC used:

1. force generation through screw/bolts
2. pneumatic driving mechanism

a)   b)
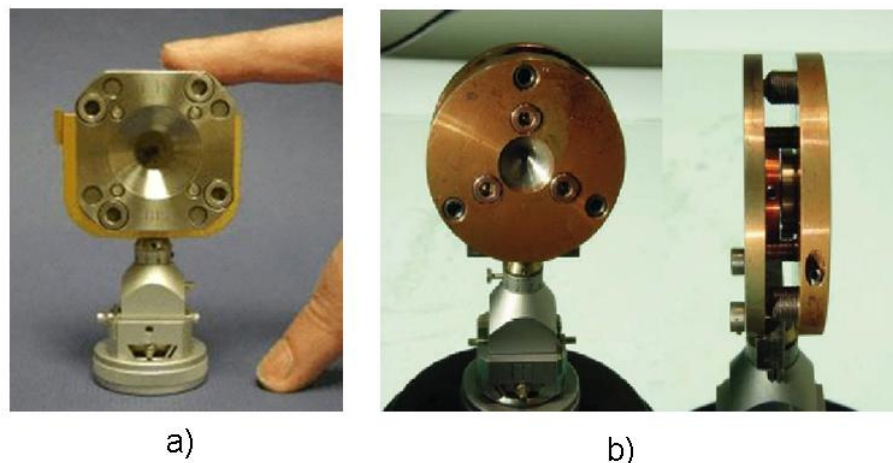
Figure 3.13 DAC with bolt force generating mechanism: a) ETH cell and b) Boehler-Almax DAC, both mounted on goniometre heads.

The first type of DACs is the force generation through screws/bolts is the most widely used system where the pressure is introduced by screwing 3 or 4 bolts in sequence, individually or by the use of a gear tool. These cells are relatively small and light, which makes them preferred for XRD analyses. Examples of such cells are the "ETH" (see fig 3.16a) and the "BGI" cell, both based on the Mao-Bell design [87] as well as the Boehler-Almax cell (see fig 3.16b), belonging to the most modern generation of DAC [103]. The main benefits of the Boehler-Almax DAC lies in the carbide seats on which the diamonds recline, making it appropriate for synchrotrone radiation and the improved anvil cut, reducing the attenuation of X-rays.

The gas-membrane driven DAC permits the most accurate pressure loading. This design allows changing the pressure without dismounting the cell from the instrument during the experiment. Another benefit of this DAC type is that the gas-membrane presses the pistons towards one-another in a uniformed and even way, extending the anvils working lifetime. Examples of gas-membrane driven cells are Diacell (easyLab) (see fig 3.17) and BETSA.

Figure 3.14 EasyLab μscope-RT(G) gas membrane DAC

3.2.2 Pressure transmitting media

The pressure medium enables the homogenous distribution of stress inside the gasket-embedded sample chamber. Pressure media used in high-pressure experiments can be solid, liquid or gaseous but in any case they must be *inert to the sample*, i.e. not to react with it during the experiment.

The solid pressure media, usually alkali-halides, are the easiest to use. Only a couple of pressure medium grains are needed for pressing down within the pressure chamber so that the sample and the pressure calibrant are nested in the mid-point. The alkali halides become transparent when relatively low pressure is applied to the cell (~ 1 GPa). In spite of the certain downsides related to this type of pressure medium (in terms of hydrostaticity), they are still preferable to all other types for the high-pressure/high-temperature experiments.

A liquid mixture of methanol : ethanol in the ratio of 4 : 1 is commonly used as a pressure-transmitting medium. It is (quasi)hydrostatic to 9.8 GPa. When diluted with distilled water so that the methanol : ethanol : water are in the 16 : 3 : 1 ratio, hydrostaticity is extended to 14.5 GPa [84].

Medium	Hydrostatic pressure limit (GPa)
Glycerol	1.4
Silicone oil	< 2.0
Argon	2.0
Water (distilled)	2.2
Nitrogen	3
Isopropanol	3.9
Glycerine : water = 3:2	5.3
Petroleum ether	6
Methanol	8.6
Methanol : ethanol = 4:1	9.8
Methanol : ethanol : water = 16:3:1	14.5
Neon	16
Xenon	55
Helium	70
Hydrogen	177

Table 3.3   The most commonly used pressure media and their maximum pressure before the shear stress overrides quasi-hydrostatic conditions [88, 89].

The inert gases used as pressure media are most reliable and consequently preferential for the use in high-pressure experiments although the most difficult to work with. Helium ensures outstandingly stable hydrostatic conditions up to ~70 GPa.Xe supplies hydrostatic conditions for pressure measurements up to 55 GPa [85] (see Table 4.3). On the other hand, neon and argon were used in the past under the assumption that they remain hydrostatic up to almost 80 GPa [86] only to be

more recently determined as hydrostatic only to 16 GPa (for Ne) and 2 GPa (for Ar) [87]. Hydrogen has proved to be a very good pressure-transmitting medium since it maintains hydrostatic conditions up to the Mbar range

Gas loading represents the main difficulty. The gaseous pressure medium can be introduced into the gasket hole while the half-closed DAC is in the isolated chamber. This process can be additionally cryogenically facilitated (see figure 4.13). Usually an isolated chamber containing the half-closed DAC is immersed in a pool of liquid nitrogen. Once the inert gas condensates within the DAC, the cell is immediately closed, directly or telescopically via a system of gear mechanism accessed from outside the isolated gas-pressure chamber. The cryogenic loading of the gas pressure medium exposes the diamond anvils to very serious hazard of the brittle failure
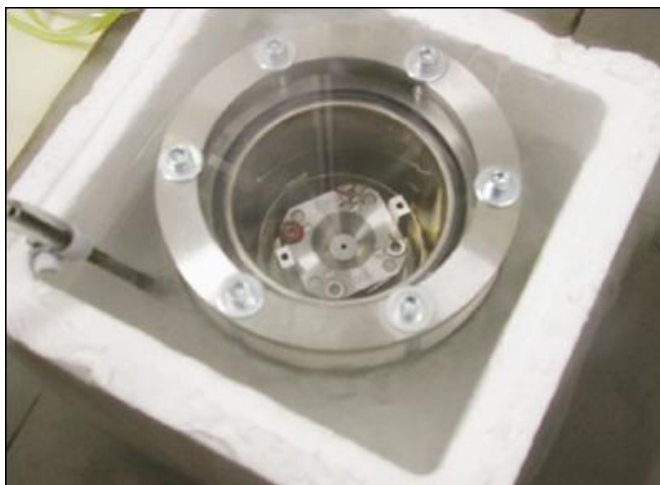
Figure 3.15 The cryogenic loading - the isolated chamber containing DAC into which inert gas is pumped is immersed into the Styrofoam bath containing liquid nitrogen (picture made at the *BGI* Bayreuth).

3.2.3 Pressure calibration standards

The ruby luminescence method is widely used for the pressure measurement in the diamond anvil cell. Ruby is a variety of corundum (α-Al_2O_3, $R\bar{3}c$) containing between 3000 to 5000 ppm of Cr^{3+} substituting Al. Ruby does not undergo a phase transition for pressures under a Mbar and room temperature, RT. Cr^{3+} has a slightly larger ionic radius compared with Al leading to small elastic strain within the structure

and an off-centre displacement from the octahedral central positions. Under the laser excitation, strong fluorescence in the shape of a sharp doublet observed at ambient conditions is:

- R_1 – 694,2 nm (14 402 cm^{-1})
- R_2 – 692,8 nm (14 432 cm^{-1})

It appears due to the change in the electron states from the ground to the metastable $^4A_2 \rightarrow\ ^2E$ of Cr^{3+} in the distorted octahedral coordination [90-93].

Electron Config- uration	Cubic Field Terms		Eigen- state	Transition to Ground State	Energy (cm^{-1})
$t_2^2 e$	$^4T_1$		$^4A_2$ ^4E	Y	25200 24400
t_2^3	$^2T_2$		$\overline{E}_b$ $\overline{E}_a$ $2\overline{A}$	B_3 B_2 B_1	21360 21070 21000
$t_2^2 e$	$^4T_2$		$^4A_1$ ^4E	U	18450 18000
t_2^3	$^2T_1$		$\overline{E}_a$ $2\overline{A}$ $\overline{E}_b$	R'_1 R'_2 R'_3	15190 15170 14960
t_2^3	^2E		$2\overline{A}$ $\overline{E}$	R_2 R_1	14430 14400
t_2^3	$^4A_2$				0

Figure 3.16 The electronic energy levels in ruby, after Eggert et al [92].

Under pressure, the ruby doublet exhibits a red shift, which under hydrostatic conditions is linear up to the Mbar range with pressure dependency of Δλ/Δp = 0.306 nm/GPa [94, 95]. Pressure can be determined from the wavelength of R_1 line, according to the recalibrated ruby pressure scale by Mao et al (1986) [96]:

$$P = 1904 \left[\left(\frac{\lambda(p)}{\lambda_0} \right)^B - 1 \right] \cdot \frac{1}{B} \tag{3.15}$$

where λ is the measured R_1 wavelength at pressure p and λ_0 is the position of the R_1 at ambient conditions, B is is an empirically determined coefficient. For hydrostatic conditions B is 7.59 ± 0.04 cm^{-1}/GPa by Piermarini et al and corrected by

Mao to 7.665 ± 0.04 cm^{-1}/GPa and for non-hydrostatic conditions B is 5 (see figure 3.17) [97].

The precision of the ruby luminescence calibration standard is of the order of ± 0.03 GPa [98]. The precision of the pressure measurement also depends on the size, shape and the degree of crystallinity of ruby crystals. The most commonly used micro-crystals chips have considerable internal elastic strain.
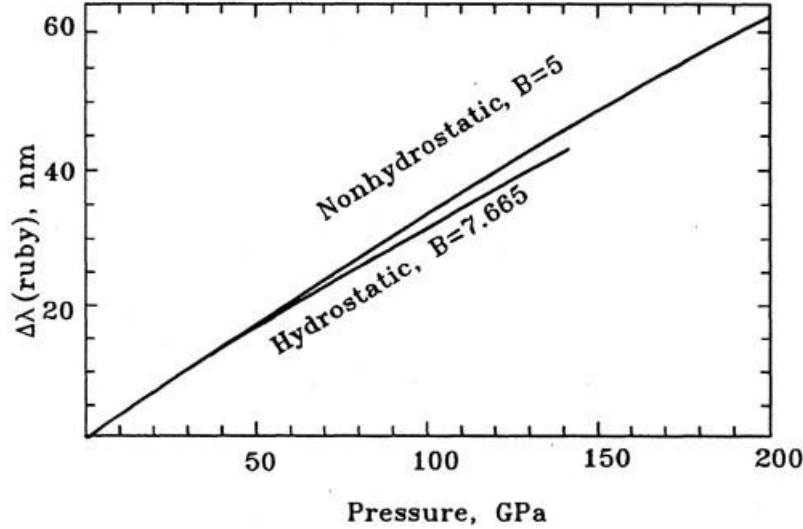
Figure 3.17 Ruby pressure calibration curve, after Mao [97]

The temperature sensitivity is a disadvantage of this calibration method. The gradient of the temperature leads to a wavelength shift for the R_1 line of $\Delta\lambda/T \sim 6.2 \times 10^{-3}$ nm/K [94, 99]. An empirically derived equation by Vos and Schouten determines the R_1 line shift relative to the ΔT change near 300 K according to:

$$\Delta R_1 = 6.591 \times 10^{-3} \times \Delta T + 7.624 \times 10^{-6} \times \Delta T^2 - 1.733 \times 10^{-8} \times \Delta T^3 \qquad (4.16)$$

In the recent years, compounds doped with rare earth elements have exhibited luminescent features similar to ruby, but with negligible temperature-dependence. Sm^{2+} doped compounds show up to 4 times larger wavelength shift and almost no sensitivity to temperature variation [100-102]. The FWHM of the single excitation line of Sm^{2+} corresponding to its $^5D_0 \rightarrow {}^7F_0$ transition and is about a third of the ruby doublet which ensures high precision. It is probable that once these materials become more easily available, ruby as a pressure-calibrant shall be replaced.

3.2.4 Instrumentation and experimental conditions used in this study

For high-pressure experiments ‹100› - oriented plates were polished to a thickness of ~ 50 μm and subsequently samples of approximate size 50 × 50 × 50 μm^3 were cut from these plates.

The high-pressure micro-spectroscopic measurements were performed with the gas-membrane driven Diacell$^®$ μScopeDAC-RT(G) (easyLab) equipped with diamonds preselected with low luminescence. A mixture of methanol - ethanol - water in the ratio 16 : 3 : 1 as used as the pressure-transmitting medium, which ensured hydrostatic conditions above 9.8 GPa. The pressure was determined by the shift of the R_1 photoluminescence peak of ruby chips, positioned next to the sample.

3.3 Other analytical methods applied to characterize the samples

Cubic-shaped single crystals of linear size ca 3 – 5 mm were used in this study, The samples were synthesized in the Laboratory of Crystal Growth, Bulgarian Academy of Sciences, using the high-temperature solution growth method. The cooling rate was individual relative to the compound:

1. PST – 0.3 K/h (for suppressed oxygen deficiencies)
2. PSN – 0.3 K/h
3. Ba-PST – 0.5 K/h
4. Ba-PSN – 0.5 K/h
5. Bi-PSN – 0.5 K/h until 1193 K and then with rate of 0.3 K/h
6. PSTN – 0.5 K/h
7. Ba-PSTN – 0.5 K/h

The stoichiometry and chemical homogeneity of the as-synthesized samples used in this study was characterized by the electron microprobe (EMP) analysis Camebax microbeam SEM-system.

The average structure at ambient pressure and room temperature was probed by the in-house powder X-ray diffractometry (XRD) (Philips X'Pert diffractometer), in-house single crystal XRD (Nonius Kappa CCD difractometer) and synchrotron single-crystal XRD (at F1 beamline, DESY/HASYLAB using high-energy radiation wavelength λ = 0.4000 Å and a MAR CCD 165 detector).

4. Results

4.1. Chemical compositions and unit cell parameters at ambient pressure

Table 4.1 presents the chemical composition, tolerance factors and crystallographic information about the compounds used in this study

PST and PSN and their doped analogues exhibit relaxor behaviour when a certain degree of compositional disorder exists in the structure. If completely B-site disordered the corresponding compound has a 'single-perovskite' $Pm\bar{3}m$ symmetry. If partially or completely ordered the structure can be refined in 'double-perovskite' $Fm\bar{3}m$ symmetry. From this cubic structure the material changes into a ferroelectric rhombohedral phase by slight angle distortion, less than 0.03 degrees even at liquid nitrogen temperatures and small atomic displacements along the cubic body diagonal. Only PST and PST-Ba possess spatial regions with B-site long-range order detectable via powder XRD, because the size of B-site ordered regions in PST-Ba is approximately 5 times bigger than in PST.

Dielectric measurement show that all compounds exhibit relaxor behaviour [8, 114]. According to our synchrotron XRD experiments, the solid solution PSTN as well as all Ba-doped compounds are canonical relaxors, i.e. at $T < T_m$ the X-ray scattering originating from PNRs is gradually enhanced and no FE long-range ordering is developed. At low temperature PST and PSN clearly show additional Bragg reflections, typical of rhombohedral structure. At low temperatures PSN-Bi also exhibits mean Bragg reflections related to FE long-range ordering, along with the still existing XDS, which indicates that the size of FE domains in PSN-Bi is on the detection limit of synchrotron single crystal XRD analysis.

Sample designation	Chemical composition	e⁻ configuration	ionic radius r_i (Å)[ii]	t	in-house powder at RT Symmetry, a (Å)	in-house powder at RT B-site order[iii]; domain size[iv] (nm)	synchrotron single-crystal 300 K symmetry	synchrotron single-crystal 150 K FE LRO (rhombohedral)
PST	$PbSc_{0.5}Ta_{0.5}O_3$	O^{2-}: $2p^6$ Sc^{3+}: $3p^6$ Nb^{5+}: $4p^6$ Ta^{5+}: $5p^6$ Pb^{2+}: $[Xe]4f^{14}5d^{10}6s^26p^2$	O^{2-}: 1.4 (6-coord.) Sc^{3+}: 0.745 (6-coord.) Nb^{5+}: 0.64 (6-coord.) Ta^{5+}: 0.64 (6-coord.) Pb^{2+}: 1.49 (12-coord.)	0.977	$Fm\bar{3}m$, 8.154	~ 0.13; 6.4	$Fm\bar{3}m$	yes
PSN	$PbSc_{0.5}Nb_{0.5}O_3$			0.977	$Pm\bar{3}m$, 4.086	below detection	$Fm\bar{3}m$	yes
PSTN	$PbSc_{0.5}Ta_{0.36}Nb_{0.14}O_3$			0.977	$Pm\bar{3}m$, 4.079	below detection	$Fm\bar{3}m$	no
PST-Ba	$Pb_{0.78}Ba_{0.22}Sc_{0.50}Ta_{0.50}O_3$	Ba^{2+}: $[Xe]6s^2$	Ba^{2+}: 1.61 (12-coord.)	0.985	$Fm\bar{3}m$, 8.164	0.11; 32.8	$Fm\bar{3}m$	no
PSN-Ba	$Pb_{0.93}Ba_{0.07}Sc_{0.5}Nb_{0.5}O_3$			0.979	$Pm\bar{3}m$, 4.086	below detection	$Pm\bar{3}m$	no
PSTN-Ba	$Pb_{0.88}Ba_{0.12}Sc_{0.5}Ta_{0.38}Nb_{0.12}O_3$			0.981	$Pm\bar{3}m$, 4.083	below detection	$Fm\bar{3}m$	no
PSN-Bi	$Pb_{0.98}Bi_{0.02}Sc_{0.51}Nb_{0.49}O_3$	Bi^{3+}: $[Xe]4f^{14}5d^{10}6s^26p^3$	Bi^{3+}: 1.45 (12-coord)[v]	0.976	$Pm\bar{3}m$, 4.082	below detection	$Pm\bar{3}m$	yes

Table 4.1 EMP and XRD characterization of sample series used in this study.

[ii] according to Shannon, R.D. and Prewitt, C.T. [115]

[iii] estimated from the ratio ρ_{exp}/ρ_{theor}, ρ = I(1 1 1)/I(200), according to Stenger and Burggraaf [41]

[iv] determined from the Scherrer equation applied to the (1 1 1) Bragg reflection; Miller indices in $Fm\bar{3}m$.

[v] according to [116]

No matter to whether X-ray diffraction indicates a single- or double-perovskite structure, Raman scattering reveals that on the local level, of a few unit-cells all compounds have $Fm\bar{3}m$ symmetry. The occupied Wyckoff positions in the case of primitive and face-centred cubic phase are given in table 4.2.

Atoms	Wyckoff positions in $Pm\bar{3}m$
Pb	1a
Sc/*B"*	1b
O	3c
	Wyckoff positions in $Fm\bar{3}m$ **(Z=4)**
Pb	8c
Sc	4a
B"	4b
O	24e

Table 4.2 Individual Wyckoff positions of atoms in PST and PSN relative to the average symmetry of the high-temperature phase.

The vibrational modes assigned to the cubic structure and the corresponding ferroelectric rhombohedral phase are given in table 4.3.

The number of excitations which are experimentally observed in temperature-dependent Raman spectra exceeds the number of peaks allowed by group theory. This is a strong indication of a complex local nano-scale structure and local violation of the cubic symmetry due to local chemical disorder and ferroic displacements.

	$Pm\bar{3}m$	$R3m$
Pb	F_{1u} (IR)[vi]	A_1 + E
B'/ B"	F_{1u}	A_1 + E
O	2 F_{1u} + F_{2u} (ina)[vii]	$2A_1$ + A_2 + 3 E
	$Fm\bar{3}m$	$R3m$
Pb	F_{1u} + F_{2g} (R)[viii]	2A + 2E
B'	F_{1u}	A + E
B"	F_{1u}	A + E
O	A_{1g} + E_g + F_{1g} + F_{1u} + F_{2g} +F_{2u}	6 A + 6 E

Table 4.3 Transformation of phonon modes from cubic to rhombohedral symmetry upon the transition from PE into FE phase.

The Raman peaks observed at ambient pressure were assigned to definite atomic vibrations on the basis of a thorough study of the temperature evolution of phonon anomalies for a series of model relaxor compounds as well as lattice dynamics calculations [72, 73]. In the curremt high pressure Raman study the peak assignment by Mihailova et al [73] was followed. The main Raman signals are:

1. **A_{1g}** – near 820 cm^{-1} – Raman–active symmetrical BO$_6$ stretching, existing only in $Fm\bar{3}m$

2. **E_g** – near 800 cm^{-1} - Raman–active symmetrical B-O stretching, existing only in $Fm\bar{3}m$

3. **F_{1u}** – near 700 cm^{-1} - IR–active antisymmetrical B-O stretching, existing in both $Pm\bar{3}m$ and $Fm\bar{3}m$

4. The anomalous signal near 580 cm^{-1} – internal mode of deformed BO$_6$ octahedra, existing in both $Pm\bar{3}m$ and $Fm\bar{3}m$

5. **F_{2g}** – near 550 cm^{-1} – Raman–active symmetrical O-B-O bending existing only in $Fm\bar{3}m$

[vi] infrared active
[vii] inactive
[viii] Raman active

6. **F$_{1u}$** – near 430 cm^{-1} - IR–active antisymmetrical O-*B*-O bending, existing in both $Pm\bar{3}m$ and $Fm\bar{3}m$

7. **F$_{2u}$** – near 300 and 330 cm^{-1} – silent mode, Pb-O stretching in planes normal to <111> (see fig 4.2-b), anomalously active due to the noncoplanarity of Pb-O system and split due to the local double-well potentials related to the electron-phonon coupling

8. **F$_{1u}$** – near 250 cm^{-1} - IR–active *B*-localised mode, anomalously active due to *B*-cation off-centre displacements. existing only in $Fm\bar{3}m$

9. **F$_{1u}$** – near 140 cm^{-1} - IR–active *B*O$_3$ translation against Pb (coupling of *B*- and *A*- site sublattices, two ferroic species, see fig 4.2a), existing in both $Pm\bar{3}m$ and $Fm\bar{3}m$

10. The anomalous signal near 70 cm^{-1} – results from splitting of F$_{2g}$ due to Pb- off-centre shifts in planes normal to <111>, existing only in $Fm\bar{3}m$

11. **F$_{2g}$** – near 55 cm^{-1} – Raman–active Pb-localised mode, existing only in $Fm\bar{3}m$.

All modes visible but forbidden in the Raman spectrum, arising from nano-domains are often referred to as "dirty modes". The Raman activity around 300 - 350 cm^{-1} is a result of an electron-phonon coupling which leads to the dynamically off-centred displacements of Pb. Such displacements are closely related to lone pair electrons oriented along <111> . The ratio $\rho = \dfrac{I_{350}}{I_{300}}$ is sensitive to the degree of the lone pair orientational order – high value indicates the improved correlation length of coherent shifts from the Pb-O plane (fig 4.2-b).
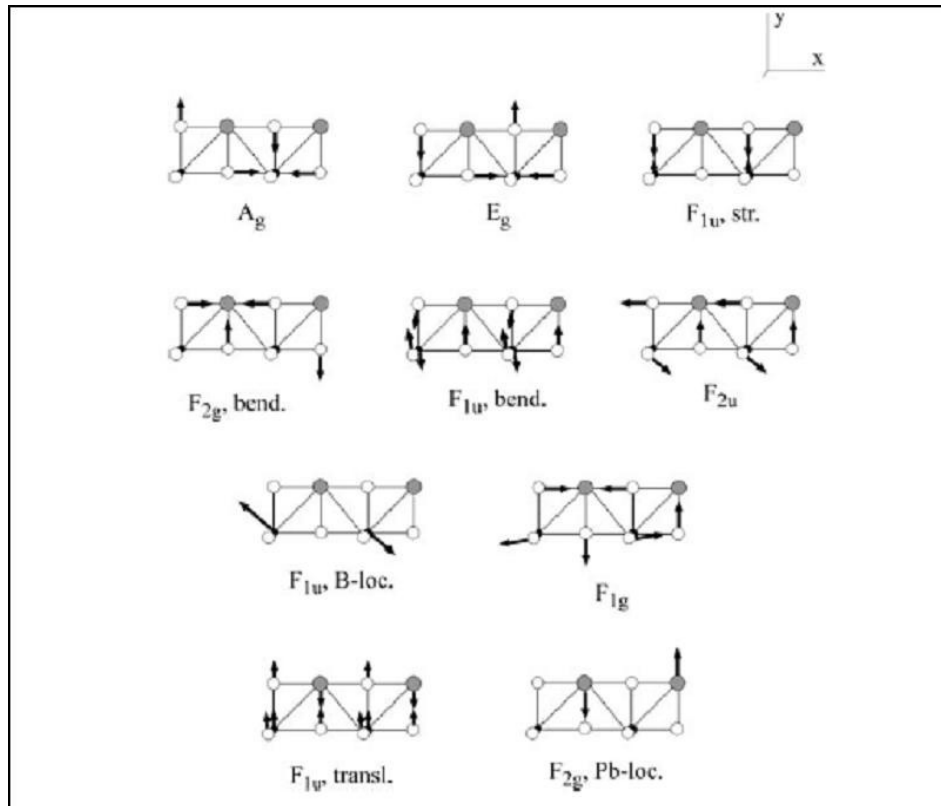
Figure 4.1 Atom vector displacements of normal modes for $Fm\bar{3}m$ symmetry for PST and PSN, after [72].
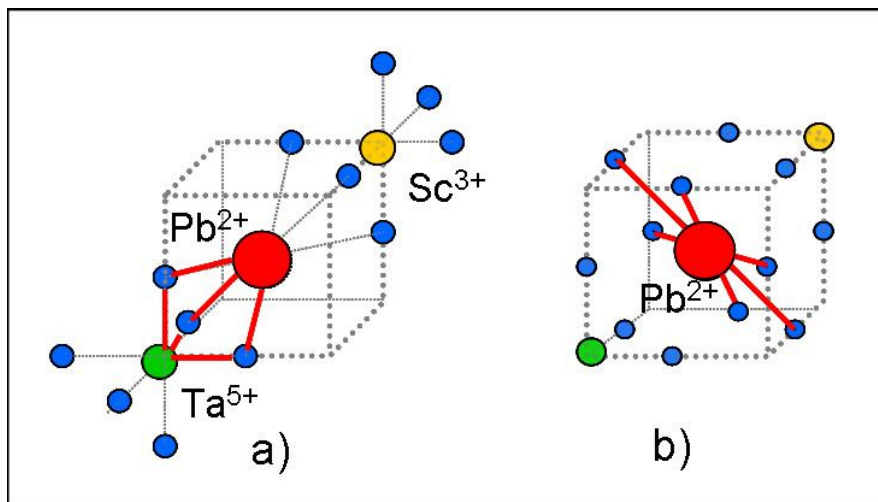
Figure 4.2 Segments of the $Fm\bar{3}m$ unit cell representing: a) coupling between the Pb and BO_3 species and b) Pb atom in the plane O-network normal to the body diagonal.

At ambient pressure and high temperature PST and PSN differ from one another in the size of ferroic Pb-O species with coherent off-centre shifts. In PST the

Pb-O correlation length is larger than in PSN, which reflects mechanisms that drive the system to a FE long-range order. At low temperatures, the Pb-O noncoplanarity is enhanced in PST, while in PSN coupling between the Pb and BO_3 species is dominant. In both cases, coupling of the Pb and BO_3 species and the lone pair electrons orientation appear to be mutually dependant. Different types of B-cations cause oxygen shifts along the cubic edge, resulting in two types of octahedra. This is reflected in the change within the Pb-O network and any shifts in heavy, stereochemically active Pb are accompanied by off-centre shifts in B-sublattice.

4.2 High-pressure Raman scattering and X-ray diffraction in PbSc$_{0.5}$Ta$_{0.5}$O$_3$

The pressure-induced structural changes in PbSc$_{0.5}$Ta$_{0.5}$O$_3$ were observed by the in-house and synchrotron single crystal XRD measurements and using Raman spectroscopy. In-house single-crystal XRD measurements showed that at ambient and low pressures the diffraction maxima with h, k, l all even (indexed according to the double-perovskite cell, $Fm\bar{3}m$) are sharp, and the measured unit-cell parameters are cubic. At pressures above 1.9 GPa the diffraction maxima show broadening (Fig. 4.3), which is completely reversible on pressure release.
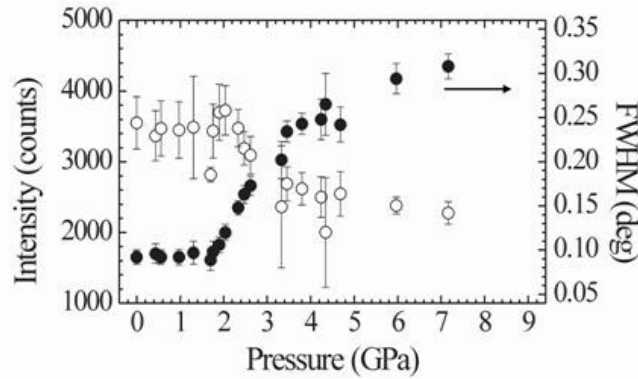
Figure 4.3 Pressure dependence of the intensity and FWHM of the (0 2 2) Bragg reflection (indexed in the $Fm\bar{3}m$). Other reflections show similar broadening. There is no systematic variation in FWHM with either reflection class or 2θ.

At the same pressure the evolution of the unit-cell volume V of the material shows a distinct change (fig. 4.4a). This change in elasticity is clearer when the data are transformed to an "f-F" plot (fig. 4.4b) in which the normalized pressure $F_E = p/3f_E(1+2f_E)^{5/2}$ is plotted against the Eulerian finite strain, $f_E = \left[(V_0/V)^{2/3} - 1\right]/2$. The low-pressure data indicate that the bulk modulus K_T of the material is *decreasing* with *increasing* pressure. At $p>2$ GPa the slope of the f-F plot is positive, and a direct fit of the p-V data indicates that $dK_T/dp = 13 \pm 4$.
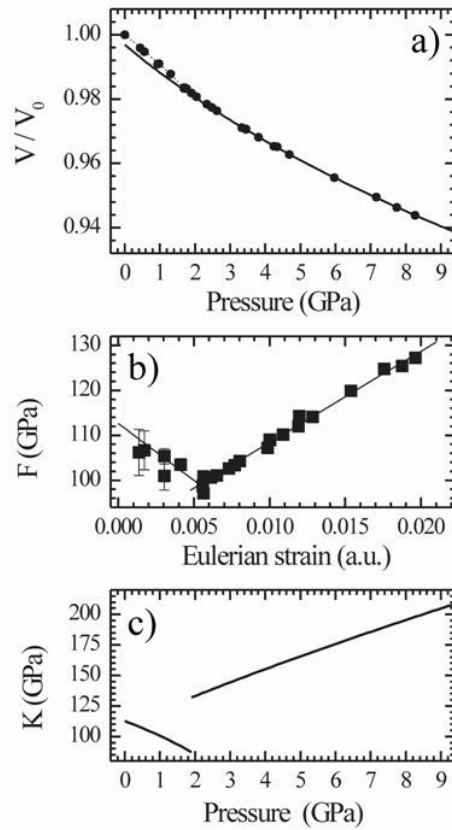
Figure 4.4 Pressure dependence of the pseudocubic unit-cell volume normalised to the volume at ambient pressure, $f - F$ plot and elastic bulk modulus K vs. pressure.

The low-pressure diffraction patterns (Fig. 4.5) reconstructed from the synchrotron X-ray scattering data contain the same classes of Bragg reflections with h, k, l= all even and h, k, l = all odd found at ambient conditions. They correspond to an apparent $Fm\bar{3}m$ symmetry of the average structure. Upon pressure increase, the diffuse X-ray scattering considerably weakens above 1.9 GPa.
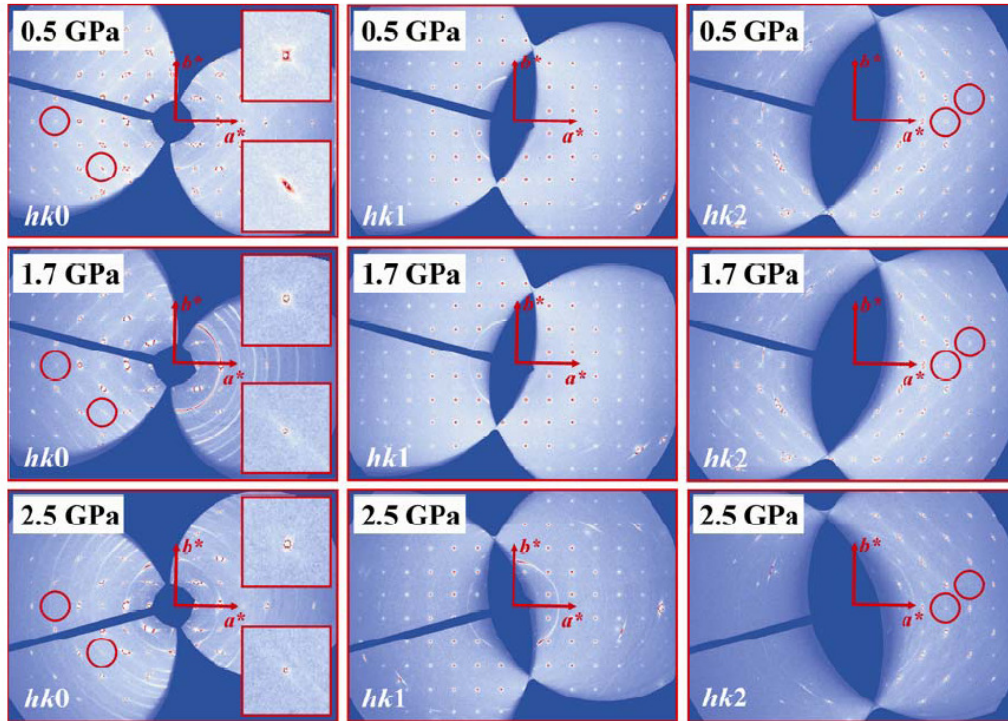
Figure 4.5 The reciprocal lattice reconstruction of synchtotron XRD data. The red circles mark example diffraction maxima of the type $h + k + l = 4n + 2$, which exhibit a significant decrease in intensity as pressure is increased to 1.9 GPa and are absent at higher pressures. The insets demonstrate the suppression of the diffuse scattering above the phase transition.

The pressure evolution of the Raman scattering reveals a sequence of reversible changes in the *local structure*, on a time scale much shorter than that of the dynamic fluctuations of polar nanoclusters. The Raman peaks observed at ambient pressure were unambiguously assigned to specific atomic vibrations on the basis of comprehensive polarized Raman studies of stoichiometric and doped PST and PSN [72, 75, 76]. In the lower energy region (< 400 cm^{-1}), significant pressure-induced changes indicate structural transformations involving Pb and *B*-site cations. At 1.2 GPa the peak near 135 cm^{-1} splits in two (Fig. 4.6). This peak is generated by rhombohedrally distorted BO_3-Pb species (see Fig. 4.6, the inset on right) and arises from a single rhombohedral mode related to the F_{1u} translational mode of the prototype structure $Fm\overline{3}m$, which involves motions of the BO_3 units against the Pb atoms.
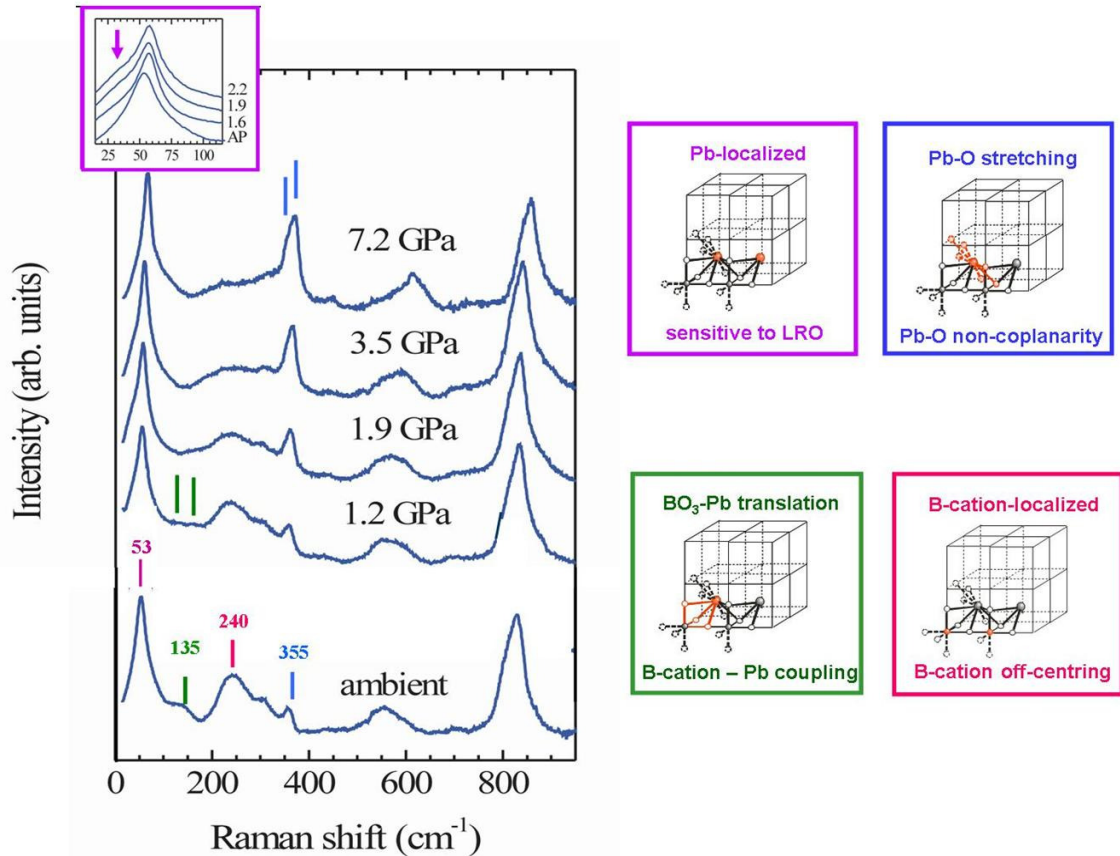
Figure 4.6 The Raman spectra of PST at different pressures with marked peak where the most pronounced pressure-induced changes take place, and their corresponding origins.

The peak at 240 cm^{-1} becomes strongly suppressed at higher pressures. It is related to the F_{1u} mode of $Fm\bar{3}m$ localized in the B-site cations. Its anomalous Raman activity is due to B-cation off-centred shifts.

In the region around 355 cm^{-1} one peak which is resolvable at ambient pressure splits in two at high pressures. This Raman signal is due to the noncoplanarity of Pb and O atoms within <111> planes and it is sensitive to Pb-O bond stretching interactions within the Pb-O layers [72]. Above 2 GPa, a new Raman peak near 37 cm^{-1} is clearly observed (the left inset in Fig. 4.6), which arises from a soft mode associated with the phase transition and involves the vibrations of the orderly displaced heavy Pb atoms. In the high energy region, the change in the appearance of the band between the 550 – 600 cm^{-1} related to the internal BO_6 vibrations, indicates that the octahedra undergo substantial adjustments to adapt to the compressing volume.

4.3 High-pressure Raman scattering of $PbSc_{0.5}Nb_{0.5}O_3$

As in the case of the PST, the most pronounced pressure-induced spectral changes in $PbSc_{0.5}Nb_{0.5}O_3$ (PSN) are observed in the low-energy region below 400 cm^{-1}. The peak at 155 cm^{-1}, related with the BO$_3$-Pb translation exhibits no splitting as observed in the case of PST but is strongly suppressed upon pressure increase.
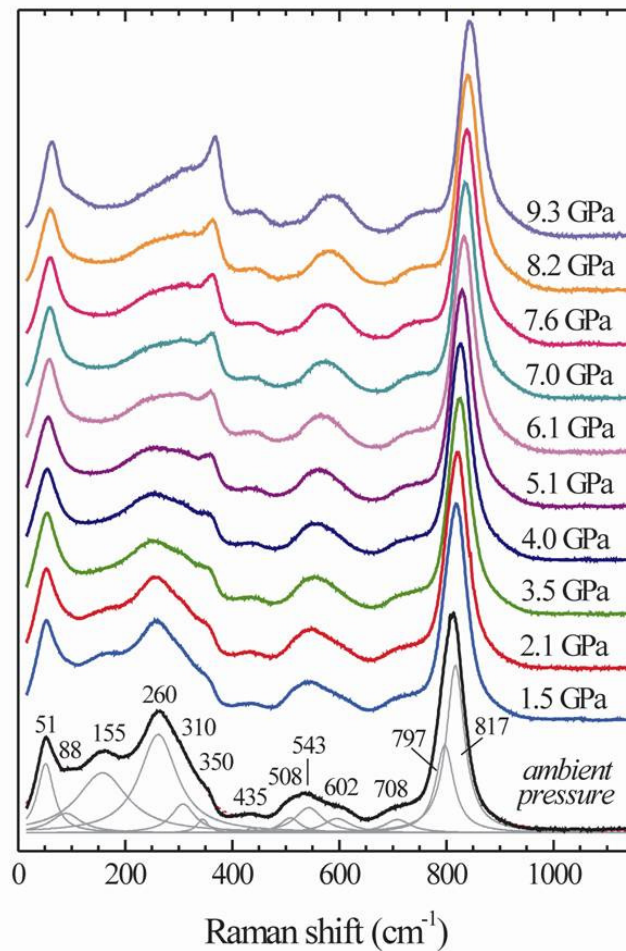
Figure 4.7 Raman spectra of PSN collected at different pressures. Thin grey lines represent Lorentzian modelling replicas.

The intensity of the peak at 260 cm^{-1} drops significantly between ambient pressure and 4 GPa. This indicates that, as in the case of PST, the *B*-cation off-centre shifts are drastically reduced on rising pressure. No splitting was observed in the 350 cm^{-1} peak related with the Pb-O stretching but with higher pressure, it becomes significantly enhanced.

In the high-energy region, the modes related to the internal BO_6 vibrations indicate that Nb affects the pressure-induced octahedral evolution in a different way than Ta in PST. At ambient pressure, three Lorentzian excitations were used to model the region between 500 – 600 cm^{-1}. As the band became more symmetrical, above 3.5 GPa an additional Lorentzian was dropped and only two had to be used. This indicates that at higher pressures the BO_6 octahedra in PSN become more regular, unlike in the case of PST. Unlike in PST, the region near 710 cm-1 was fitted with a single peak, which is in agreement with the assumption that in PSN the BO_6 octahedra are less deformed. At the same time, the bands in the region 800 - 830 cm^{-1} originating from the BO_6 symmetrical stretching are also more symmetrical compared with the same peaks in PST.

4.4 High-pressure Raman scattering of Ba-doped PbSc$_{0.5}$Ta$_{0.5}$O$_3$

$Pb_{0.78}Ba_{0.22}Sc_{0.5}Ta_{0.5}O_3$ (PST-Ba) is a new, recently synthesized canonical relaxor. The observed Raman modes were previously attributed to definite atomic vibrations on the basis of polarized spectra of lead scandium niobates and tantalates measured at ambient pressure and different temperatures. The number of Lorentzian mode profiles used to fit the spectrum at ambient pressure is consistent with the number of expected peaks.

The Raman spectra collected at different pressures resemble strongly the PST data at high pressures (see figures 4.6 and 4.8). The A_{1g} and E_g modes, related to the internal BO_6 symmetrical stretching vibrations and give rise to the peaks near 830 and 802 cm^{-1}. As in the case of pure PST, the region around 710 cm^{-1} is related to the anti-symmetrical stretching mode of rhombohedrally distorted BO_6 octahedra. The presence of Ba however leads to a splitting of the Raman signal, into two components near 735 cm^{-1} and near 696 cm^{-1} where the lower-energy component is enhanced at HP.
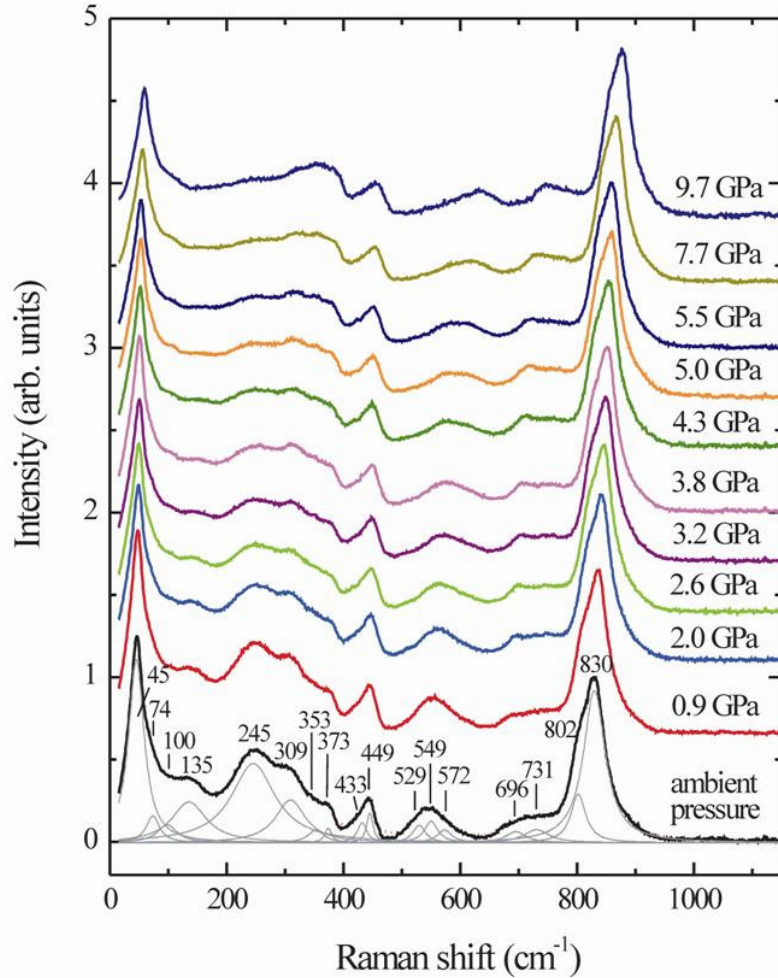
Figure 4.8 Collected PST-Ba Raman data up to 9.7 GPa; thin grey lines represent used Lorentzian replicas.

The region between 500 – 600 cm^{-1}, comprising the band related to the internal BO$_6$ bending, becomes more asymmetrical at high pressures. The mode near 572 cm^{-1} resulting most probably from the rhombohedral stretching mode, is enhanced at high pressures while the peaks at 529 and 549 cm^{-1} drop in intensity.

Due to the presence of an additional A-site cation, the peak at 353 cm^{-1} is already split from ambient pressure. The splitting is a consequence of the Pb-O bond shortening within the AO$_{12}$ polyhedra in the {111} planes. Additionally, the pressure-induced enhancement of the Raman scattering near 353 – 373 cm^{-1} peaks is not so strongly pronounced as in the case of pure PST. The peak at 245 cm^{-1} is related to the cubic F$_{1u}$ mode comprising B-site cation vibrations (B-cation localized mode), whose Raman activity is due to the existence of off-centred B-cations in polar nanoregions and is strongly suppressed. As in the case of PST and PSN, this mode is suppressed with pressure increase. The peak at 135 cm^{-1}, related with Pb atomic

vector displacements against the BO_3 species does not show splitting and indicates the decoupling of two ferroic species, but considerably loses intensity. The signal near 100 cm^{-1} appears due to the presence of an additional A-site cation. Pb-localized vibrations produce a peak at 45 cm^{-1} and additionally at 74 cm^{-1} due to the rhombohedral splitting of the F_{2g} mode.

4.5 High-pressure Raman scattering of Ba- and Bi-doped $PbSc_{0.5}Nb_{0.5}O_3$

PSN is a system which allows the introduction of additional A-site cations. Ba^{2+} is isovalent with Pb^{2+} but has larger ionic radius and is stereochemically inactive. Substitution of Ba^{2+} for Pb^{2+} leads to the formation of local elastic fields and in the case of PST-Ba it leads to the enhancement of the relaxor behaviour. Bi^{3+} is aliovalent to Pb^{2+} and its incorporation in the structure results in a charge-imbalance. However, it shows a strong affinity to form stereochemically active electronic lone pairs, which would not disturb the existing system of lone pair electrons. In order to elucidate the dominant role of elastic vs electric fields under high-pressure conditions, $Pb_{0.93}Ba_{0.07}Sc_{0.53}Nb_{0.47}O_{2.98}$ (PSN-Ba) and $Pb_{0.98}Bi_{0.02}Sc_{0.51}Nb_{0.49}O_3$ (PSN-Bi) were investigated by Raman spectroscopy.

The Raman spectra measured up to 10 GPa are presented in figure 4.9. As in the case of pure PSN, the band between 500 – 600 cm^{-1} observed for PSN-Ba and PSN-Bi at ambient conditions comprises three modes, out of which two are anomalous and related to the rhombohedral octahedral distortion while the peak, at 545 cm^{-1} is the Raman active F_{2g} mode associated with the internal BO_6 bending. Initially, three Lorentzian mode profiles were used for to fit this band. Above 2 GPa, the band becomes more symmetrical and the third replica is omitted. However, in PSN-Bi at pressures above 6 GPa new weak peak at 490 cm^{-1} appears.
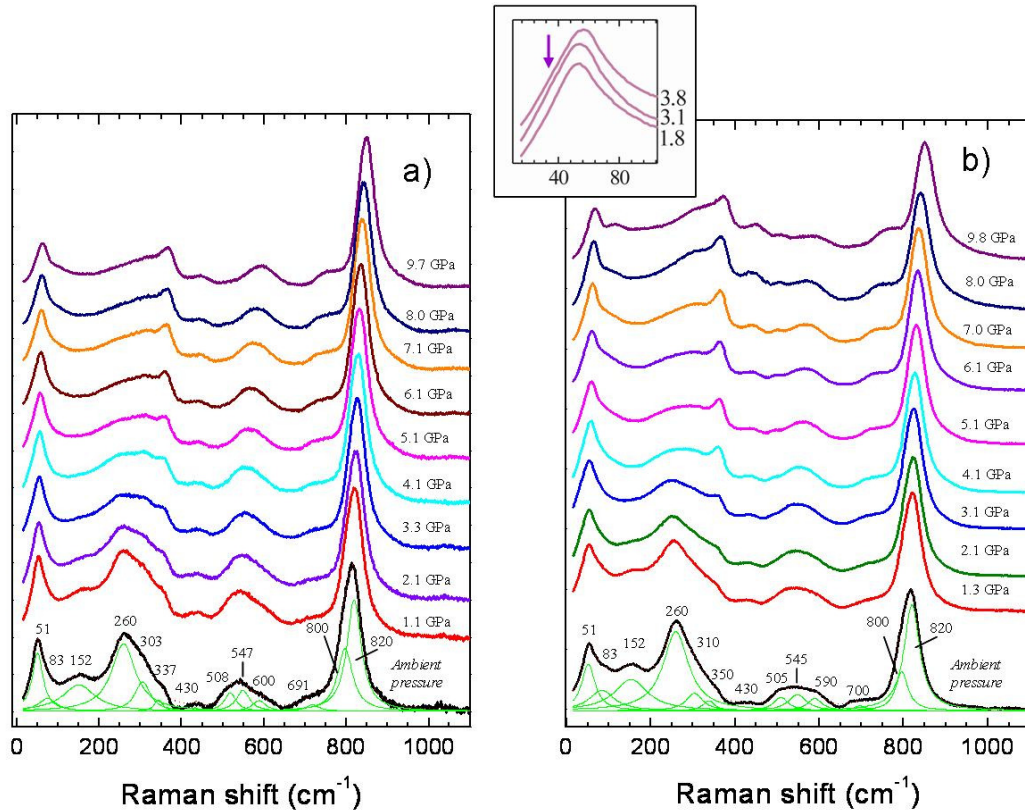
Figure 4.9 Raman spectra of a) PSN-Ba and b) PSN-Bi measured at different pressures with the soft mode inset. Same number of Lorentzians was used in both cases (marked as thin green lines).

Changes involving *A*- and *B*-site cations vibrations can be observed in the lower energy region. The Pb-O stretching mode, at 350 cm^{-1} in both PSN-Ba and PSN-Bi is strongly enhanced with pressure as in the case of PSN. Additionally, as observed in other Pb-based relaxors, the mode near 260 cm^{-1} associated with *B*-cation off-centre shifts is strongly suppressed with pressure. The peak at 150 cm^{-1} related to Pb translations against the *B*O$_3$ species also becomes weaker with the pressure increase. In PSN-Bi, above 3 GPa a new mode appears near 35 cm^{-1}, as in the case of PST, indicating the occurrence of a pressure-induced phase transition.

4.6 High-pressure Raman scattering of undoped and Ba-doped solid solution of $PbSc_{0.5}Ta_{0.5}O_3$ and $PbSc_{0.5}Nb_{0.5}O_3$

PSTN and Ba-doped PSTN represent compounds of a pure and Ba-doped solid solution of PST and PSN. PSTN is a complex system involving three types of *B*-cations competing within the structure. Local cation enrichments are expected in both cases resulting in Ta- or Nb-dominant chemical domains. Additionally, the incorporation of Ba-cation on *A*-sites frustrates the spatial growth of polar nano-regions (PNRs).

PSTN and Ba-doped PSTN were investigated by means of Raman spectroscopy under high pressures up to 10 GPa. At ambient pressure both oxides have $Fm\bar{3}m$ symmetry and exhibit pronounced canonical relaxor properties. The observed number of modes corresponds to the expected one for Pb-based relaxors. In the course of fitting 14 Lorentzian mode profiles were initially used for PSTN and 15 for PSTN-Ba (fig 4.10 - profiles). The extra Lorentzian at 400 cm^{-1} used for PSTN-Ba results from deformed octahedra adjoining the incorporated Ba^{2+} cations. The same additional profile was used in the case of PST-Ba. For PSN-Ba the introduction of such a peak was not needed in order to rationally fit the spectrum profiles, because the content of Ba in PSN-Ba (Ba/Pb = 0.07) is considerably smaller than that in PSTN-Ba (Ba/Pb = 0.12) or PST-Ba (Ba/Pb =0.22) and the contribution from the deformed BO_6 octahedra could be neglected. The same is valid for the additional Lorentzian profile near 700 cm^{-1}. For pure PSTN the Raman scattering in the range 670 – 750 cm^{-1} was also better fitted when two Lorentzian functions were used. In this case however, the two modes are related to the existence of two *B"* cations and hence, a two-mode behaviour of the antisymmetrical BiO_6 stretching results. It should be noted that only for this type of vibration a two-mode behaviour was detected. All the other peaks that arise from internal BO_6 or from *B*-localized modes exhibit one mode behaviour, i.e. the pressure of two *B"*-cation leads to shifts in the peak positions as compared to those for the two end members.
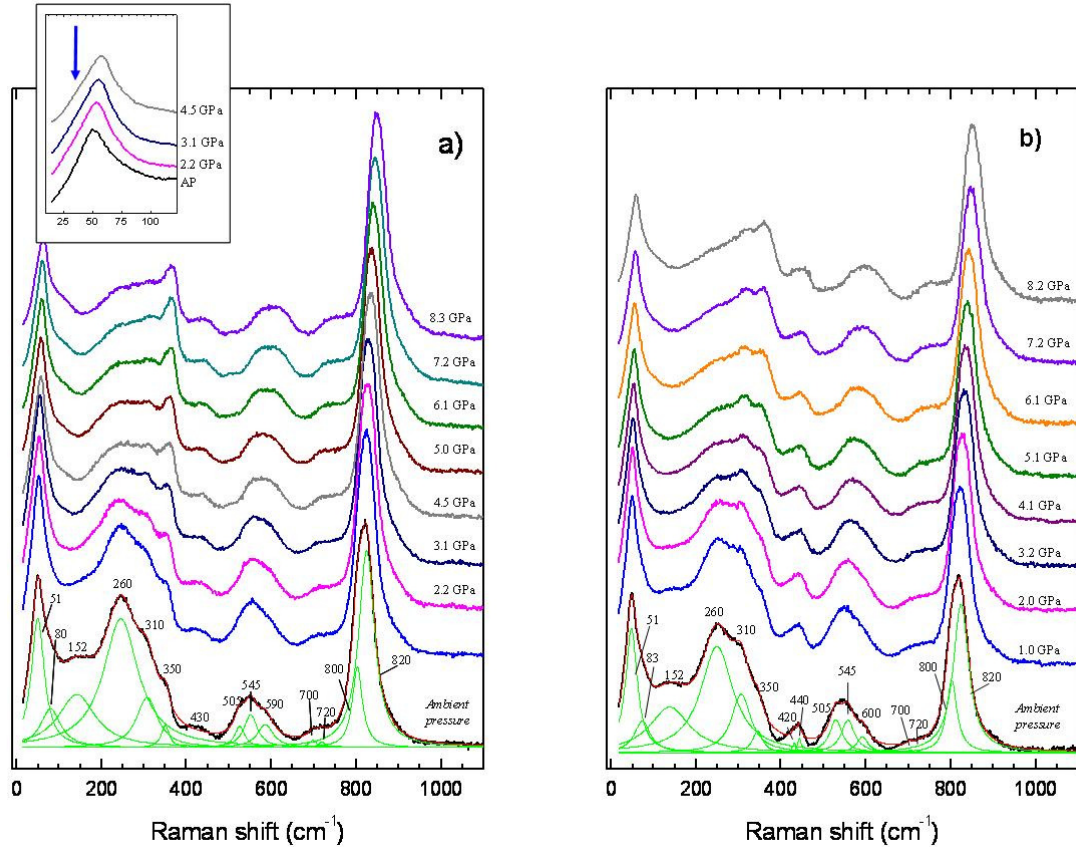
Figure 4.10 Raman spectra of a) PSTN and soft mode appearing at 2.2 GPa
(inset) and b) PSTN-Ba measured at different pressures.

The A_{1g} and E_g modes, related to the internal BO_6 symmetrical stretching vibrations are resolvable at 820 cm^{-1} and 800 cm^{-1}, respectively. The Raman scattering near 730 and 700 cm^{-1} is related to the antisymmetric stretching of the distorted BO_6 octahedra. The band between 500 – 600 cm^{-1} consists of three peaks, associated with the symmetrical and antisymmetrical O-B-O bending within the BO_6 octahedra. Even though this band evolves over pressure resembling the case in pure PSN, all three modes are present even above 8 GPa, as in the case of pure PST.

The intensity of the mode observed at 350 cm^{-1} increases with pressure in PSTN and PSTN-Ba, which is in agreement with the results from the pure and Ba-doped PSN and PST. The mode is related with the Pb-O bond stretching and it is Raman active due to the non-coplanarity of Pb displacements along <1 1 1> . However, in PSTN-Ba, both peaks enhance with pressure, while in PSTN the 350 cm^{-1} is stronger than the one at 310 cm^{-1}. Additionally, in PSTN the peak at 350 cm^{-1} is split above 4 GPa.

The anomalous Raman peak near 250 cm^{-1} which is due to off-centre displacements on *B*-sites is strongly suppressed in both, pure and Ba-doped PSTN as in the case of other compounds. The translation of Pb-atoms against the *B*O$_3$ species results in the peak near 150 cm^{-1}. The peak is suppressed even at pressures below 2 GPa. Similarly to pure PST, an additional soft mode appears near 30 cm^{-1} indicating the occurrence of a pressure-induced phase transition. The critical pressure however is slightly higher (at 2.5 GPa) for PSTN as compared to PST (1.9 GPa).

5. Discussion

5.1 Pressure-induced structural transformations in $PbSc_{0.5}Ta_{0.5}O_3$

The broadening of the h, k, l = all even (indexed according to the the double-perovskite cell, $Fm\bar{3}m$) at the pressures above 1.9 GPa cannot represent a decrease in domain/crystallite size because the corresponding reflections arise from the average cubic structure alone.

There is no detectable discontinuity in the unit-cell volume (fig. 4.4a), but there is in the bulk modulus (fig. 4.4c). These observations are characteristic of a thermodynamically second-order structural phase transition involving elastic softening in both phases as they approach the phase transition [104].

The low-pressure diffraction patterns (see fig. 4.5), reconstructed from the synchrotron X-ray scattering data contain the same classes of Bragg reflections with h, k, l = all even and h, k, l = all odd found at ambient conditions, corresponding to the apparent $Fm\bar{3}m$ symmetry of the average structure. The <110> diffuse streaks results from atomic displacements in the polar nanoregions [105] and decrease in intensity when approaching p_c, but at $p > p_c$ the streaks still persist in weakened form, suggesting that correlated atomic displacements remain in the sample at least up to 2.8 GPa. With increasing pressure up to p_c = 1.9 GPa the intensities of certain reflections with $h + k + l = 4n + 2$ (n integer) decrease continuously (Fig. 4.5). Structure factor calculations suggest that this can only result from antiferroic displacements of the Pb atoms in the *average* structure. The absence of new classes of reflections at high pressures eliminates the possibility of a transition to a structure in which the BO$_6$ octahedra are tilted in-phase [106].
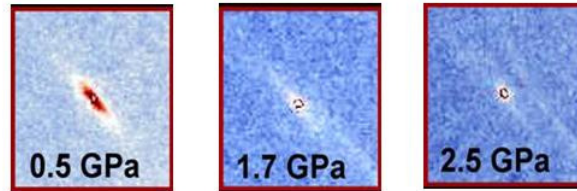
Figure 5.1 The suppression of the diffuse scattering in the <110> direction resulting from the atomic displacements in the polar nanoregions.

However, the structure could develop an anti-phase tilt system which would only contribute small changes to the intensities of the h, k, l = all odd reflections [106]. Thus, the symmetry change of the double-perovskite framework alone is restricted from $Fm\bar{3}m$ to become either $R\bar{3}m$, $I4/m$ or $C2/m$. Space group $C2/m$ is, however, excluded because of the thermodynamically continuous character of the transition. If the tilt pattern corresponds to $R\bar{3}m$ symmetry, then the presence of antiferroic Pb displacements deduced from the change in the intensities of the $h + k + l = 4n + 2$ reflections would reduce the symmetry to the same $R3$ symmetry found at low temperatures [72, 75, 76]. The development of domains of lower symmetry than cubic also explains the reflection broadening (Fig. 5.1) as being the result of unresolved splitting.

In the Raman scattering data, the first observed pressure-induced change is the splitting of the peak near 135 cm^{-1} at 1.2 GPa. It is generated by the rhombohedrally distorted BO$_3$-Pb species and the splitting indicates a violation of the dynamical coupling between the Pb- and the B-cation system in the polar nanoregions. At the same pressure of 1.2 GPa the pressure dependence of the wave number $\omega(p)$ for the scattering near 355 cm^{-1} has a kink (fig 5.2b). This Raman signal is due to noncoplanarity of Pb and O atoms within <111> planes and it is sensitive to Pb-O bond stretching interactions within the Pb-O layers.
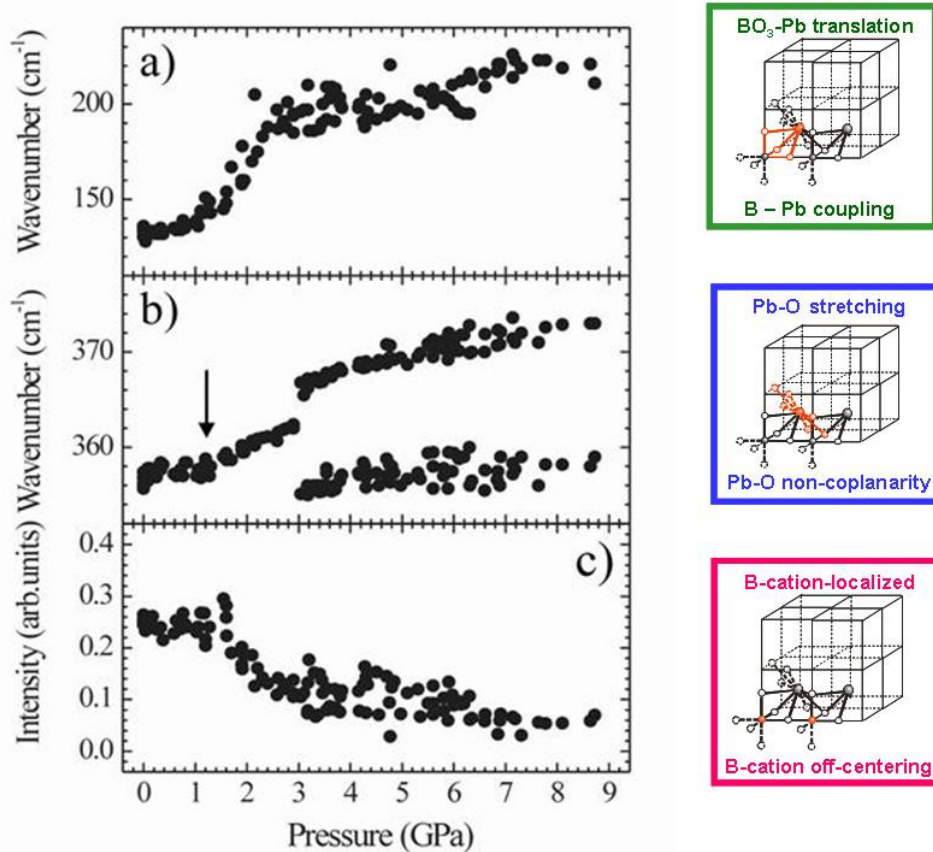
Figure 5.2 Pressure dependence of Raman peak positions (ω) and intensities (I) determined by fitting the spectra with Lorentzian mode profiles. The plots represent data collected from different samples. The absolute error in ω and I is within the statistical deviation.

The change in the slope of $\omega(p)$ indicates that the rate of stiffening of the Pb-O bonds within the <111> planes with pressure is increased above 1.2 GPa. On further pressure increase up to 1.9 GPa the higher-wave number component of the BO$_3$-Pb translational mode rapidly shifts to higher energies (Figs. 4.6 and 5.2a).

Above the critical pressure p_c = 1.9 GPa a soft mode that appears near 37 cm^{-1} is associated with the phase transition detected by XRD. Apparently, the soft mode comprises vibrations of the heavy Pb atoms and its occurrence confirms the conclusion also based on XRD data, that the high-pressure phase is characterized by ordered Pb displacements. Near p_c the peak at 240 cm^{-1} drops in intensity (fig. 5.2c). This peak is related to the F$_{1u}$ mode of the $Fm\bar{3}m$ symmetry and is localized in B-site cations. Its anomalous Raman activity is due to the existence of the B-cation

off-centred shifts. The spectral changes show that the loss of coupling between the Pb and *B*-cation systems allows the displaced *B* cations to move back to the octahedral centres and the structure relaxes via enhancement of the structural anisotropy in the Pb system as would be expected for a symmetry change to $R3$. However, Raman scattering reveals that the high-pressure local structure differs from that at low temperatures. The observed decoupling between Pb and *B*-cation displacements and further suppression of *B*-cation off-centre shifts indicates a pressure-induced fragmentation of polar nanoregions existing at ambient pressure and is in accordance with changes of the dielectric permittivity at moderate pressures. The decrease in intensity of the *B*-localized mode continues up to 3 GPa (fig. 5.2c). At that pressure a splitting of the Pb-O mode near 355 cm^{-1} occurs (fig 5.2b), which points to a further enhancement of the ferroic distortion in the Pb-O system. Slightly above 3 GPa a small change in the $\omega(p)$ slope of the peak near 830 cm^{-1}, arising from BO_6 symmetrical stretching appears (fig 5.3). This reveals a decrease in the average BO_6 octahedral compressibility.
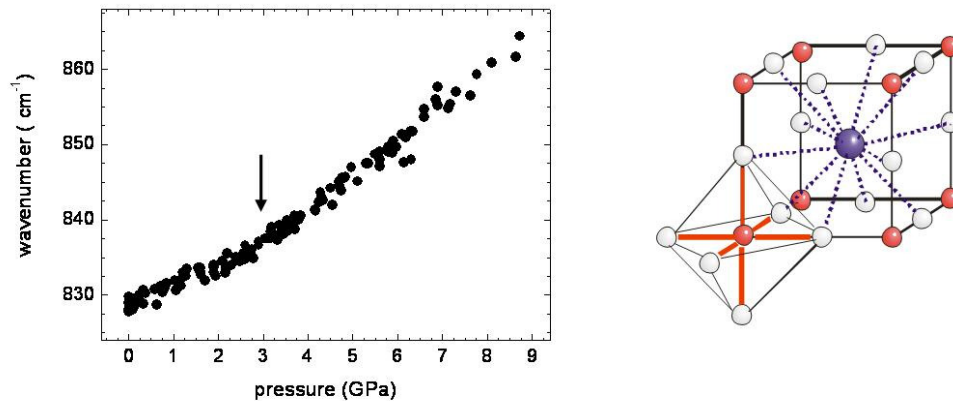
Figure 5.3 The pressure evolution of the ω (A$_{1g}$) from symmetrical stretching of the BO_6 octahedra (left).

The pressure range of local structural changes above p_c corresponds to the pressure range of gradual weakening of the diffuse scattering. The strong decrease in the diffuse scattering at a critical pressure is associated with the structural elastic instability involving a continuous change in the pseudo-cubic volume compressibility and the appearance of a soft mode. The high-pressure phase is characterised by the loss of coherence between the sublattices of *B* cations and Pb atoms; the former

becomes "less distorted," while the latter "more ferroic." No further pressure-induced structural alterations were deduced from the Raman spectra up to 9 GPa.

The initial compression of PST near T_m occurs via bond shortening. Eventually, the volume reduction can no longer be accommodated by the bond shortening and the framework undergoes a continuous phase transition at 1.9 GPa associated with an elastic instability that is typical of octahedral tilt transitions in perovskites. The XRD data are consistent with the high-pressure phase having the same *average* symmetry, $R3$, as that found at low temperature [21]. This would result in a positive slope of the equilibrium phase boundary in *p-T* space, in accordance with principle governing tilt transitions in perovskites [107] showing that PST behaves as a normal "2:4" perovskite. The tilted octahedra then allow ferroic ordering of the Pb atoms on a macroscopic length scale. The development of complete long range order of the Pb displacements is continuous as evidenced by the persistence of the diffuse scattering immediately above the transition. The pressure-induced atomic rearrangements in PST, namely, Pb shifts that correlate within <111> planes and chains of anti-phase tilted octahedra with suppressed *B*-cation *polar* off-shifts, should be characteristic of all Pb-based relaxors and explain the disappearance of X-ray diffuse scattering above a certain pressure. This interpretation is in full agreement with the Raman spectra showing that the displacements of the *B*-site cations in the existing dynamical polar nanoclusters are suppressed in the HP phase whereas the local noncubic displacement of ferroic Pb-O species is enhanced. For PST the structural changes are clearly observed by both, diffraction and Raman scattering because of the longer coherence length of ferroic Pb-O species that is already apparent at ambient conditions.

5.2 Pressure-induced structural transformations in PbSc$_{0.5}$Nb$_{0.5}$O$_3$

In PSN, the first pressure-induced changes above ambient involve Pb-atoms. The wavenumber ω of the Pb-localized F$_{2g}$ mode near 51 cm^{-1} as a function of pressure p exhibits a minimum at 2.2 GPa (figure 5.4).
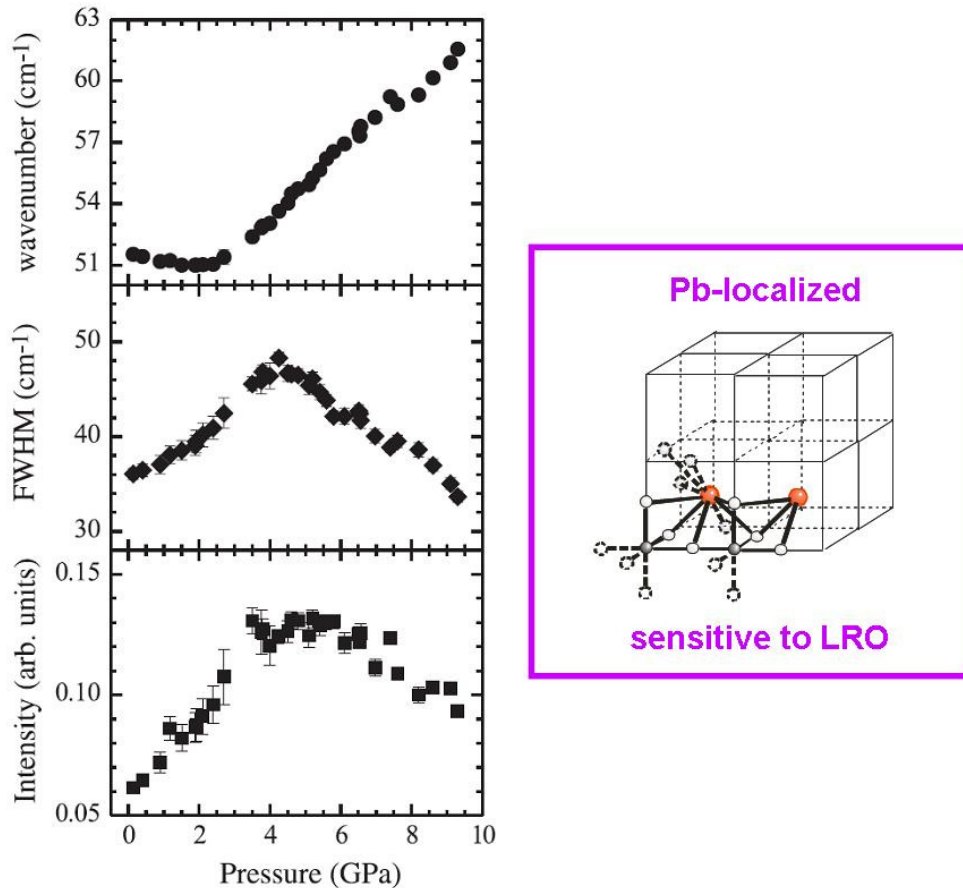
Figure 5.4 Pressure evolution of the Raman-active Pb-localized F$_{2g}$ mode at 51 cm^{-1}.

The soft mode that appears in PST at nearly the same pressure is not resolvable for PSN, most probably due to the smaller size of the ferroic species with coherent off-centred Pb shifts. However the ω (p)-dependence clearly shows softening of the pseudocubic Pb-localized mode, thus indicating pressure-induced ferroelectric ordering in the Pb system, similarly to the case of PST. However, the FWHM of the Pb-localized F$_{2g}$ mode reaches its maximum at a higher pressure, at

about 4 GPa, while the intensity has a broader maximum between 4-6 GPa (figure 5.4). Phonon modes involved in the phase transition experience substantial damping near the critical point because of the structural instability. Besides, in systems with dynamical structural fluctuations as in the case of relaxors, an increase in both FWHM and intensity of the lowest-energy mode is expected near the phase transition due to its coupling with the flip mode. Thus, the pressure dependence of the width and intensity of the peak at 51 cm^{-1} indicates that most significant structural transformations in PSN take place near 4 GPa. Indeed, the pressure dependence of the unit cell volume measured by Angel et al (unpublished), reveals that the pressure induced phase transition for this compound occurs at 4.1 GPa.

Further we considered the Raman scattering near 155 and 260 cm^{-1}. Both signals arise from infrared-active F_{1u} modes of the prototype cubic structure and their appearance in the Raman spectra is due to the existing polar nanoregions. The phonon mode near 155 cm^{-1} comprises in-phase vibrations of the B-cation and oxygen atoms, which can be considered as a translation of the "rigid" BO_3 group, as well as Pb vibrations opposite to the BO_3 motion. In the ideal perovskite-type structure with a primitive cubic cell this type of vibration is called the 'Last' mode [18]. In terms of rhombohedral symmetry, which is typical of the low-temperature state of perovskite-type relaxors, the Raman peak near 155 cm^{-1} results from a non-degenerate A-mode corresponding in frequency to the longitudinal F_{1u} cubic mode of the prototype structure. This assignment is in good accordance with the polar mode frequencies in $PbMg_{1/3}Nb_{2/3}O_3$ determined by infrared reflectivity spectroscopic analysis [108]. In the case of PST, a splitting of this mode was observed upon pressure, which indicates the suppression of the dynamical coupling between the off-centred Pb and B-site cations [109]. No apparent splitting of this mode was observed for PSN, which is most probably due to the smaller size and fraction of polar nanoregions as compared to PST. However, the width of the Pb-BO_3 translation mode increases near 2.5 GPa, i.e. close to the characteristic pressure at which softening of the Pb-localized F_{2g}-mode is observed (figure 5.4). Besides, the Pb-BO_3 mode wavenumber dependence on pressure for PSN (see figure 5.5) resembles that observed for PST, indicating the occurrence of similar phenomena in both compounds. Hence, we assume that decoupling of the Pb and B-cation systems in polar nanoregions occurs in PSN as well. The $\omega(p)$-trend suggests that this process abundantly takes place above 4 GPa, where $d\omega(p)/dp$ of the Pb-BO_3 translation mode rapidly increases. This is in accordance with the observed structural instability at about 4 GPa revealed by the maximum of FWHM of the Pb-localized F_{2g} mode

(figure 5.4). Near 6 GPa the $\omega\,(p)$ dependence of the Pb-BO$_3$ translation mode becomes nearly constant, showing that the transformation processes attain a saturation state.
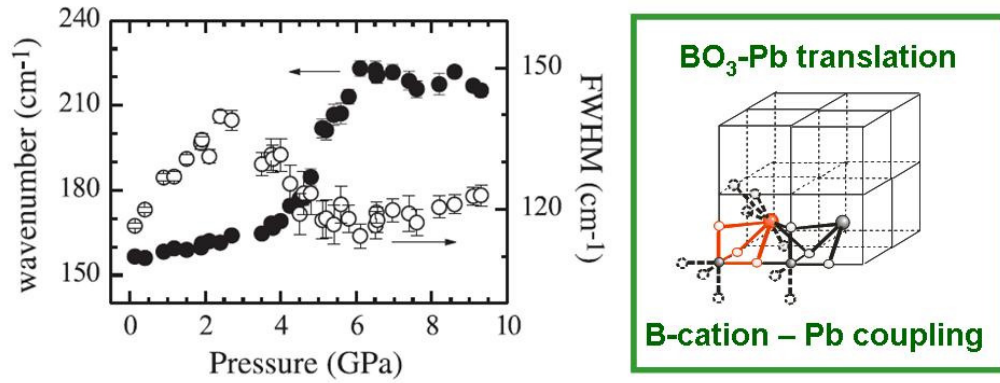
Figure 5.5 Wavenumber (open symbols) and FWHM (filled symbols) versus pressure for the Raman scattering near 155 cm^{-1} arising from Pb-BO$_3$ translation mode.

The pressure evolution of the Raman scattering near 260 cm^{-1}, which arises from the B-cation localized mode in polar nanoregions, also points out that 4 and 6 GPa are characteristic pressures (see figure 5.6). The pressure dependence of the wavenumber and FWHM shows respectively softening and damping of the mode at 4 GPa. At this pressure a drop in the intensity of the B-localized mode occurs, which reveals massive movement of the B-site cations back to the octahedral centres. At 6 GPa the intensity and FWHM reach a constant value, suggesting the completion of the corresponding structural changes. A pressure-induced decrease in the Raman scattering intensity near 250 cm^{-1} is typical of all perovskite-type relaxors studied [61, 109, 110] and, therefore, the suppression of off-centred displacements of B-cations is a characteristic structural feature of the HP state of relaxors. The intensity decrease is not so well pronounced for relaxor-PbTiO$_3$ solid solutions [111, 112], which indicates that the addition of PbTiO$_3$ stabilizes the B-cation off-centring.
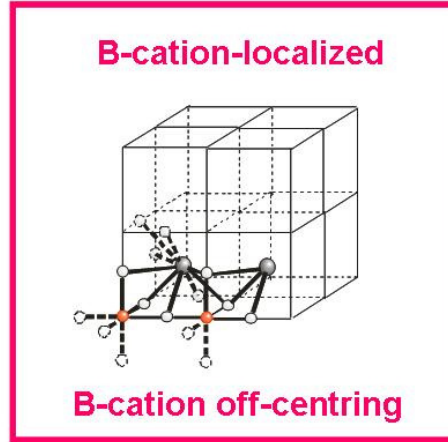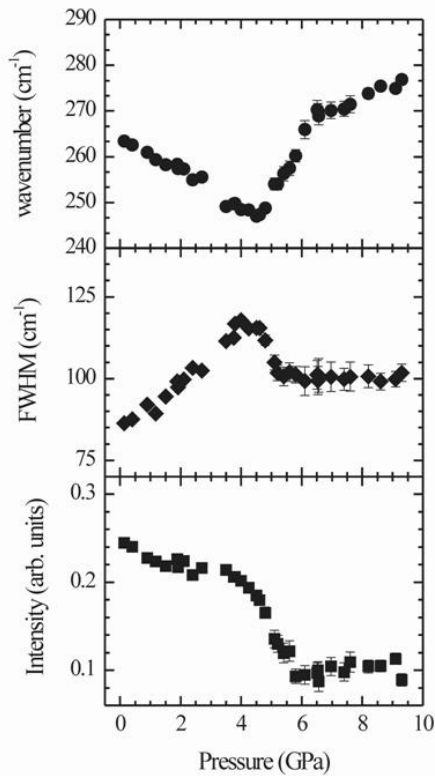
Figure 5.6 Pressure dependence of the wavenumber, FWHM and intensity of the B-cation-localised localised F_{1u} mode near 260 cm^{-1}, which is observable in Raman spectra due to presence of off-centred displacements of the *B*-cations from their cubic positions.

Figure 5.7 presents the pressure dependence of the wavenumber and intensity of the Raman scattering near 350 cm^{-1}. This signal is associated with the silent F_{2u} mode of the prototype cubic structure, which involves Pb-O bond stretching vibrations, and its appearance in the Raman spectra is due to coherent off-centred shifts of Pb atoms with respect to the oxygen atom planes perpendicular to the cubic body diagonal [72].
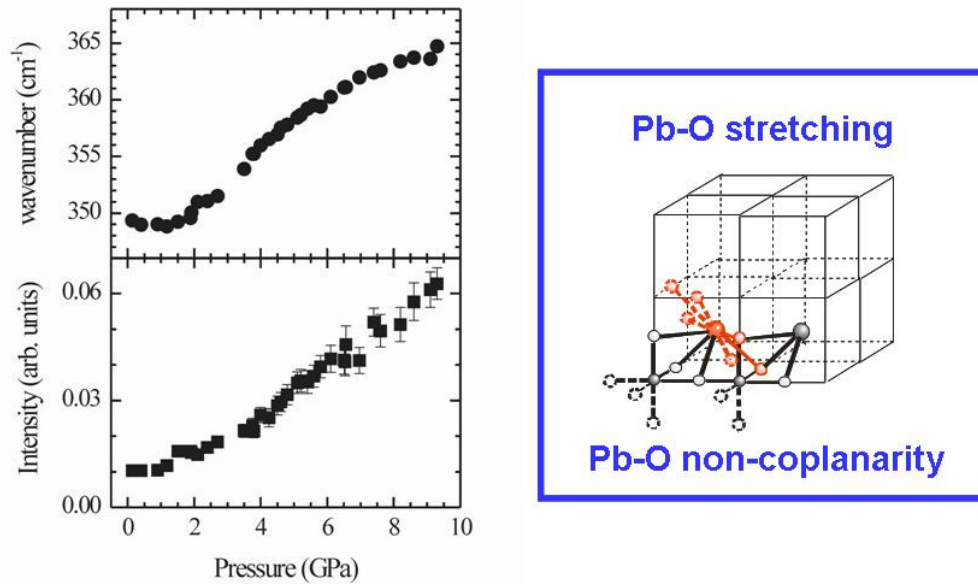
Figure 5.7 Pressure dependence of the wavenumber and intensity of the Raman scattering near 350 cm^{-1}.

The ω (p)-dependence of this peak has a kink near 2 GPa, which corresponds well to the minimum of ω (p) of the Pb-localized F$_{2g}$ mode near 51 cm^{-1} and also points to structural transformations in the Pb system. The increase in the Raman intensity near 350 cm^{-1} is enhanced above 4 GPa, i.e. when the suppression of off-centred B-cation displacements takes place. Therefore, the PSN structure responses to external elastic fields via enhancement of the ferroicity in the Pb-O system. The same pressure-induced increase in the Raman intensity near 350 cm^{-1} is observed for all Pb-based perovskite-type relaxors and related solid solutions [110-112]. Hence, the pressure-enhanced enlargement of the coherence length of off-centred Pb shifts is a common structural feature for that class of materials.

The pressure evolution of the Raman scattering of PSN up to 10 GPa reveals three characteristic pressures, p_1 ~ 2 GPa, p_2 ~ 4 GPa and p_3 ~ 6 GPa, at which the local structure undergoes transformations. The first pressure is associated with ferroic ordering processes in the Pb-O system, which however cannot be followed by the existing off-centred B-cations, triggering structural instabilities. As a result, at the second characteristic pressure massive structural changes take place, which involve a violation of the dynamical coupling between the off-centred Pb and B-cations indicating a movement of the B-cations back to the octahedral centres. At the third

67

pressure the suppression of B-cation off-centred shifts reaches saturation and upon further mechanical load the structure relaxes mainly via enlargement of the size and fraction of Pb-O ferroic clusters.

The comparison between PSN and PST shows that the replacement of Ta by Nb increases the characteristic pressure at which the decoupling of the Pb- and B-cation systems in polar nanoregions and consequent suppression of B-cation off-centred shifts occurs. This indicates that ferroic Pb-O-Nb atomic linkages are more stable than the corresponding Pb-O-Ta linkages. Ferroic ordering in the Pb-system takes place at nearly the same pressure for both compounds. For PST this structural transformation is revealed by the appearance of a soft mode, whereas for PSN it is manifested by the softening and damping of the Pb-localized Raman-active cubic mode. In the case of PSN, the decoupling of the Pb- and B-cation systems in polar nanoregions happens at a pressure higher than the pressure of ferroic ordering of the Pb-system, while the two transformation events take place at nearly the same pressure for PST. The distinction between the two compounds is most probably due to the difference in the stiffness of the Pb-O-B linkages and B-cation masses.

5.3 Effect of *A*-positioned Ba on the structure of $PbSc_{0.5}Ta_{0.5}O_3$

The incorporation of Ba leads to additional Raman peaks. The signal near 100 cm^{-1}, which is well resolved in cross-polarized spectra, is due to the presence of a second A-site cation. The concentration of Ba in PST-Ba is the highest among the three Ba-containing compounds studied here. Hence, the effect of Ba on the surrounding atoms in Pb-based relaxors is best pronounced in PST-Ba. The main Ba-induced changes in the ambient-pressure spectrum are additional peaks at 449 and 731 cm^{-1} as well as the additional peak near 373 cm^{-1}.
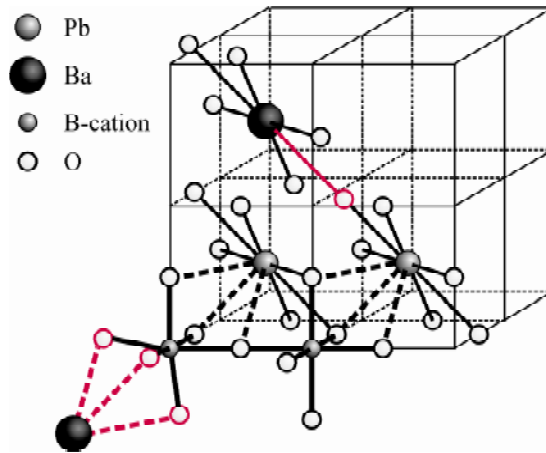
Figure 5.8 Representative structural species in a perovskite-type structure with a second A-site cation having an ionic radius larger than that of Pb as in the case of $(Pb_{1-x}Ba_x)BO_3$; Ba^{2+} deforms the adjacent BO_6 octahedra along <111> directions and shortens the A-O bonds within the {111} planes

The peak near 373 cm^{-1} is due to shortened Pb-O bonds next to BaO_{12} polyhedra within {111} planes (see fig. 5.8), while the signals near 449 and 731 cm^{-1} results from internal modes of deformed BO_6 octahedra adjoining the BaO_{12} polyhedra along $\langle 111 \rangle$ directions (see fig. 5.8). It is clear that the dilution of the Pb-system with Ba leads to considerable local "internal" pressures in the structure, which can oppose the effect of external pressure. Indeed, in the case of PST a soft mode appears at the critical pressure p_c = 1.9 GPa, whereas no additional low-wavenumber Raman signals are observed for PST-Ba.

The pressure evolution of the pseudo-cubic unit-cell volume indicates that the pressure-induced phase transition is smeared out over a pressure range between 2 and 4 GPa [117]. The $f - F$ plot has a plateau-line instead of a well-defined critical pressure point as in the case of PST. Upon the pressure increase an additional lowest energy signal was not detected for PST-Ba. However, the wavenumber of the Pb-localized mode near 45 cm^{-1} as a function of pressure has a kink near 4 GPa (see fig.5.9a). Besides, the wavenumber of the BO_3-Pb translation mode in ferroic regions substantially increases above 4 GPa (Fig. 5.9b), which also indicates abundant atomic rearrangements.

69
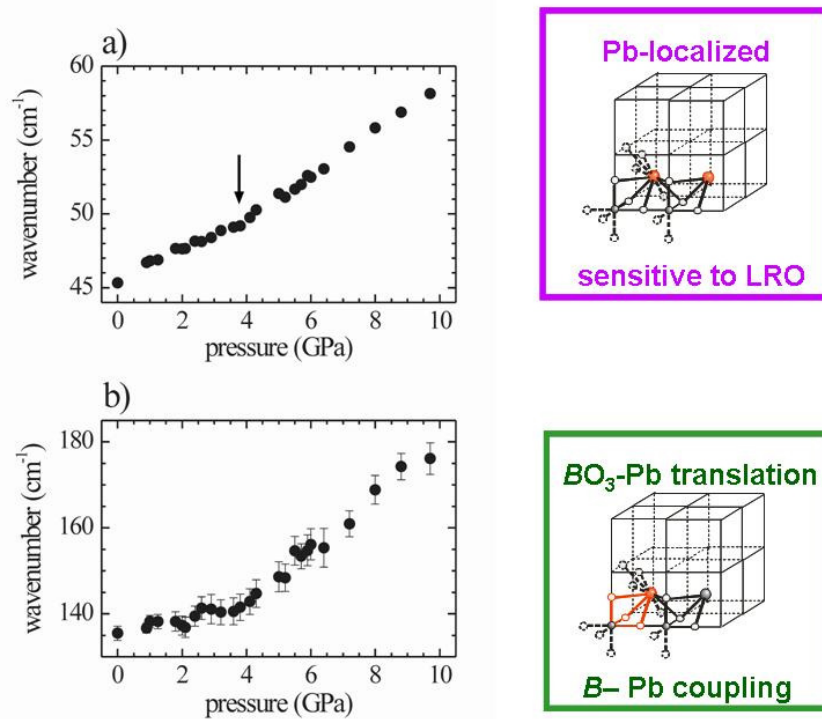
Figure 5.9 Pressure evolution of the Raman scattering frequency generated by a) the Pb-localised mode and b) BO_3-Pb translational mode in ferroic nanoregions.

Two types of pressure-induced alterations are observed for both PST and PST-Ba: the suppression of off-centred shifts of B-cations, as revealed by the intensity decrease of the Raman peak near 245 cm^{-1} (Fig.5.10a), and the enhancement of correlated Pb-O non-coplanarity in {111} planes, as manifested by the intensification of the Raman scattering near 350-370 cm^{-1} (Fig. 5.10b). High-pressure Raman spectroscopic data on other compounds indicate that these structural changes are common for all Pb-based perovskite-type relaxors. In PST-Ba the off-centred B-site cations start to move back to their central cubic positions at relatively low pressure ~1.3 GPa. This is more probably related to the fact that Ba is positioned at the centre of the AO_{12} cavity, which violates the dynamical coupling between off-centred A- and B-cations in the polar nanoregions and incites the octahedral centring of B-cations. Thus, the pressure evolution of the Raman spectra shows that the chemically-induced local elastic fields associated with A-positioned Ba are responsible for the diffuseness of the pressure-induced phase transition.

70
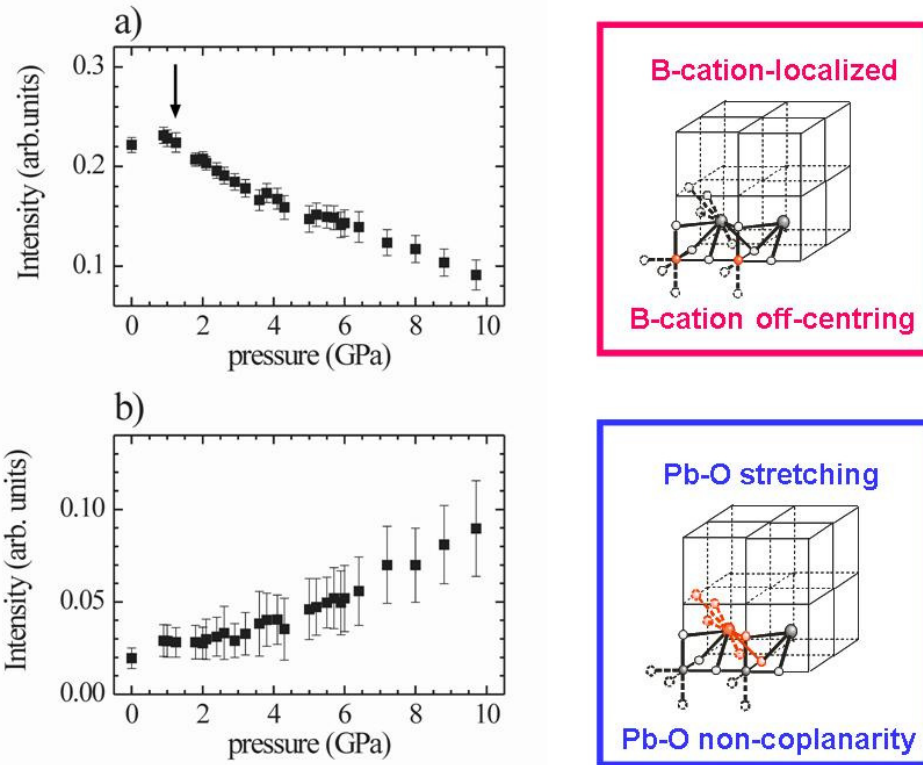
Figure 5.10 Pressure dependence of a) the integrated intensity of the anomalous Raman scattering near 245 cm^{-1} arising from *B*-cations that are off-centred from their cubic positions and b) the sum of the intensities of the anomalous Raman signals near 353 and 373 cm-1 generated by Pb-O bond stretching in Pb-O ferroic species (correlated off-centre shifts of Pb-atoms relative to oxygen atoms in {111} planes).

The incorporation of Ba into the structure of Pb-based perovskite-type relaxor ferroelectrics creates local elastic fields due to the difference between Ba^{2+} and Pb^{2+} in the ionic radius and the outermost electron shell and, thus, restrains the development of a pressure-induced long-range order. The local structural deformations in the vicinity of A-positioned Ba cations, namely, distortion of BO_6 octahedra adjoining Ba along $\langle 111 \rangle$ and shortening of Pb-O bonds within {111} planes, lead to the occurrence of a pressure-induced "diffuse phase transition", spread out over a pressure range. Although the development of ferroic long-range order is substantially disturbed by the presence of Ba, the high-pressure structural state of PST-Ba exhibits structural features which are similar to those of the high-

71

pressure phase of PST: the off-centered displacements of B-site cations are strongly suppressed, while the coherent length of ferroic Pb-O species is enhanced.

The comparison between pressure- and temperature-induced structural changes in PST and PBST reveals that the replacement of Pb^{2+} by Ba^{2+} has the same effect on the transformation processes in Pb-based perovskite-type relaxor ferroelectrics, no matter if the thermodynamical variable is temperature or pressure. In both cases, Ba doping hampers the development of ferroic long-range order. This highlights the importance of potential barriers associated with chemically-induced local strains for the occurrence of a relaxor structural state.

5.4 Ba- and Bi-induced renormalization phenomena in $PbSc_{0.5}Nb_{0.5}O_3$

In Pb-based relaxor materials at ambient pressure Pb-cations are not 'independent' but coupled with the BO_3 species. The Raman peak observed in PSN-Ba and PSN-Bi near 150 cm^{-1} arises from atomic vibrations in PNRs related to the IR F_{1u} mode which involves the BO_3 translation as 'rigid' unit against the Pb and in primitive cubic ABO_3 structure is known as the 'Last' mode. The intensity of this peak sharply drops between ~ 2 GPa to 4 GPa in both Bi- and Ba-doped PSN (see fig 5.11). The same behaviour of this mode is observed also in pure PSN. This is an indication of decoupling between these two units, which are released to individually respond to the increasing pressure. It is a precursor of all further pressure-induced changes which involving Pb and B-site cations. Similarly to pure PSN, the FWHM of the Pb-localized mode near 50 cm^{-1} has a well pronounced maximum at a certain pressure point. For both A-site doped PSN compounds the maximum is near 3.5 GPa, which is slightly below the corresponding p_c for pure PSN (figure 5.11). This is an indicator of significant structural transformations in both PSN-Ba and PSN-Bi occurring near 3.5 GPa.
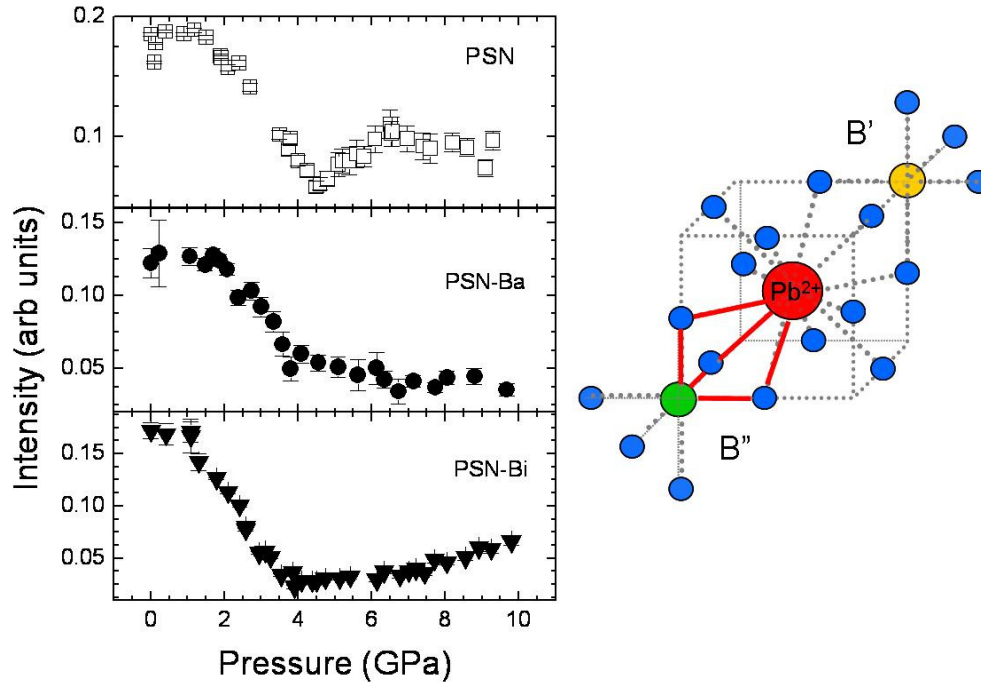
Figure 5.11 Drop of intensity of the signal at 150 cm^{-1} due to the decoupling of Pb-atom and BO$_3$ as a rigid unit (marked in red lines on the structure model on the right).

In the case of PSN-Ba, the $\omega(p)$ dependence of the Pb-localized ~ 50 cm^{-1} mode for PSN-Ba has a kink at the corresponding pressure point (figure 5.12b). This spectral feature is very similar to $\omega(p)$ for PST-Ba, which indicates that Ba has the same effect on the PbSc$_{0.5}B''_{0.5}$O$_3$ host matrix under pressure, regardless of the B''-cation type. Ba^{2+} hinders the development of the pressure-induced ferroic long-range ordering which smoothens the phase transition. This is in accordance with the $f - F$ dependences of PSN-Ba and PSN-Bi determined by Maier et al [118].
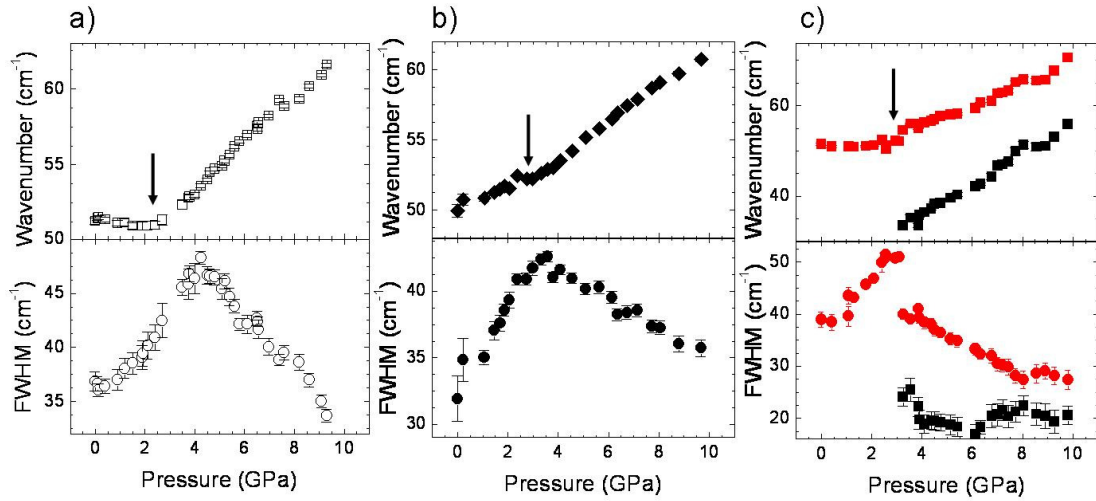
Figure 5.12 Pressure evolution of ω and FWHM of the Pb-localized F_{2g} mode of a) pure PSN, b) PSN-Ba and c) PSN-Bi, with the soft mode appearing near 35 cm^{-1} at 3.5 GPa.

The Raman data on PSN-Bi reveals that Bi^{3+} has a different effect on the structure under conditions of compressing volume, in comparison with Ba^{2+}. The incorporation of Bi^{3+} leads to the appearance of a soft mode near 35 cm^{-1}, which is not as well pronounced as in the case of PST. This suggests that the size and the fraction of ferroic domains in the high-pressure phase is lower than in PST. For pure PSN a soft mode was not resolved, so the high-pressure state of PSN-Bi in terms of the abundance of ferroic regions stands between PSN (low degree) and PST (high degree). This result is quite similar to the low-temperature structural state of PSN, PSN-Bi and PST.

The peak near 240 cm^{-1} is related to the vibrations localized in the *B*-site cations and is observed in the Raman spectrum due to their off-centre displacement. The changes in the frequency and intensity (fig 5.13) indicate pressure-induced rearrangements in the *B*-site sublattice. In both Ba and Bi-containing samples, the frequency of this mode has a minimum near 4 GPa.
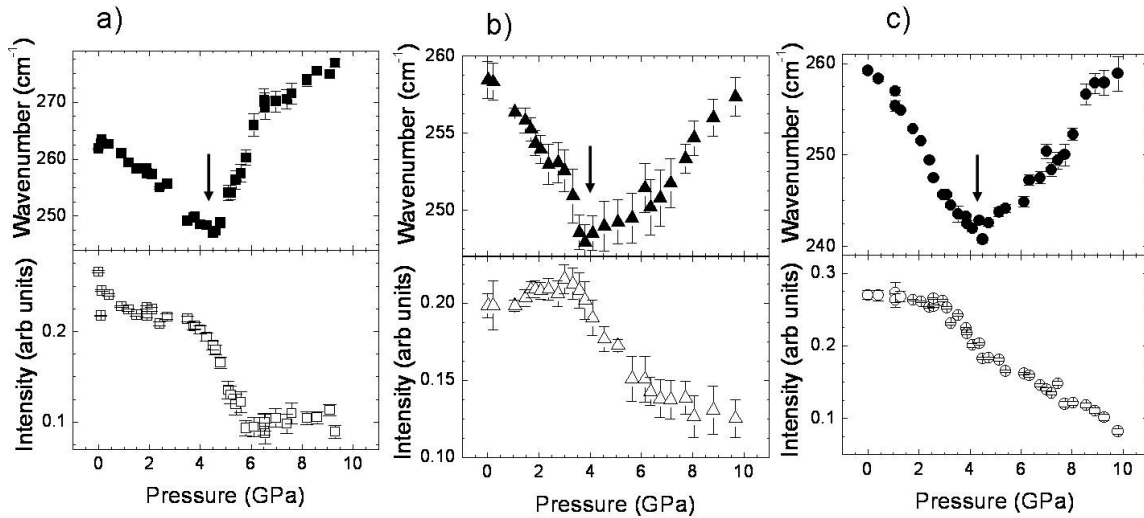
Figure 5.13 Pressure-induced evolution of ω and intensity of B-cation localised F_{1u} mode observed at 250 cm^{-1} for a) pure PSN, b) PSN-Ba and c) PSN-Bi

At this pressure point a strong drop in the intensity is observed indicating the suppression of B-site cation off-centre displacements. The pressure-induced changes in both, frequency and intensity of Ba- and Bi-containing PSN strongly resemble the pressure-evolution of the corresponding peak in pure PSN (figure 5.6). However, whereas the suppression of the intensity of the peak saturates near 6 GPa in pure PSN, in PSN-Ba and PSN-Bi such a saturation is not apparent and only a decrease in the change of the intensity as a function of pressure is observed ~ 6 GPa (see figures 5.6 and 5.13).

The anomalous Raman scattering observed in the spectral range 300 – 400 cm^{-1} results from the cubic F_{2u} silent mode which is Raman active due to the local double-well potentials related to an electron-phonon coupling and is at ambient conditions split into two components near 310 and 350 cm^{-1}. The changes in this range indicate the modifications in the Pb-O stretching and the non-coplanarity between Pb and the oxygen network along direction normal to $\langle 111 \rangle$. The intensity of the mode at 350 cm^{-1} is strongly pressure-enhanced, resulting from the improved coherence degree of the Pb-displacements from an oxygen network (see figure 5.14).
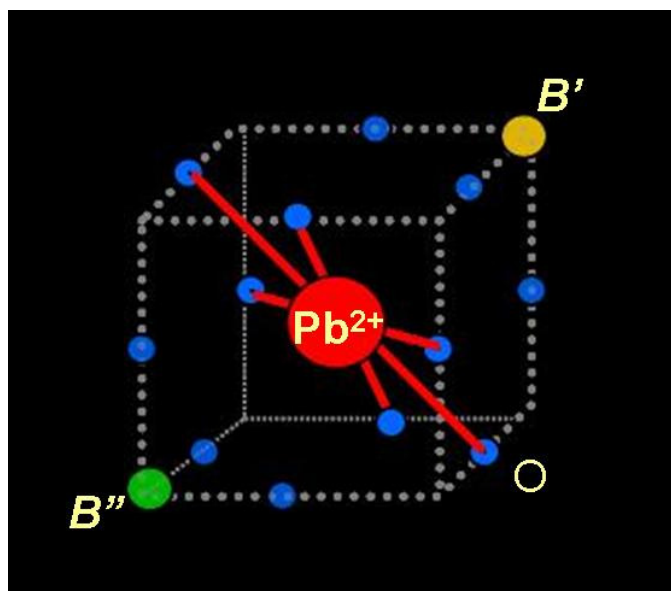
Figure 5.14 In the oxygen network Pb displaces in the direction of the cubic body diagonal.

In the case of pure PST, the peak at 350 cm^{-1} additionally splits at pressures above 4.5 GPa as a result of further lowering of the local symmetry. In PST-Ba this peak is split even at ambient pressure due to the existence of two Pb-O bond lengths in the cubic {111}. Such splitting was not sufficiently pronounced in Ba- and Bi-doped PSN samples, which is most probably a consequence of the lower concentration of dopants compared with the doped PST compounds. However, a certain asymmetry of this peak became apparent for PSN-Ba at very high pressures (above 7 GPa). It is weaker in PSN-Bi, while in pure PSN it was not resolved. It indicates that Ba^{2+} as stereochemically inactive cation significantly disturbs the orientational order of aligned Pb lone pairs or, respectively Pb off-centre displacements.

Both Pb^{2+} and Bi^{3+} have affinity to lone-pair electrons and they are quite similar with respect to their masses and ionic radii. The tolerance factor of the system is only slightly disturbed when Bi^{3+} is incorporated in PSN and therefore under pressure Bi-O species should follow or be in resonance with the changes in the dominant Pb-O species. However, on decreasing the interatomic distances, the repulsive electrostatic interactions between cations will become stronger. The process should be more pronounces for Bi^{3+} than for Pb^{2+}. This might explain why above a certain pressure Bi^{3+} cannot follow the Pb^{2+} system and the coherence in the overall A-O ferroic system is disturbed.

The region between 500 – 600 cm^{-1} related to the BO$_6$ bending modes initially comprises 3 signals, but as in the case of pure PSN, at higher pressures (2 – 3 GPa)

one is omitted since the whole band becomes more symmetrical and is successfully modelled with two Lorentzian functions. Only judging by the loss of the additional peak, one might speculate that in the case of Nb-containing compounds the octahedra at high pressures become more regular, in contrast to the Ta-containing compounds.

As proved for similar Pb-based relaxor compounds such as PST, pure or Ba-doped, and PSN, three characteristic pressure points mark the sequence of structural transformations in PSN-Ba and PSN-Bi. The decoupling between Pb and the B-cation in PNRs begin at 2 GPa, as indicated by the Raman signal near 160 cm-1. The phase transition occurs near 3.5 - 4 GPa as revealed by the Pb-localized mode. Above 6 GPa no significant changes in the intensities of phonon modes were detected up to 10 GPa.

In agreement with the XRD and Raman data for the temperature-dependent behaviour of pure, Ba- and Bi-doped PSN, Ba^{2+} and Bi^{3+} have the same impact on the spatial interaction between PNRs and the improvement of long-range order within the host matrix at the conditions of the compressing volume.

5.5 High-pressure structural behaviour of mixed $PbSc_{0.5}Ta_{0.5}O_3$ and $PbSc_{0.5}Nb_{0.5}O_3$ and the effect of Ba-doping

Based on the preceding high-pressure studies of pure and Ba-doped PST and PSN, several structural changes taking place at certain characteristic pressure points can be deduced from the pressure evolution of Raman scattering. The Pb-atoms have proven to be very sensitive to pressure. Observed changes in the Pb-localized mode indicate that the Pb-atoms is highly sensitive on increasing pressure. The soft mode that appears near 35 cm^{-1} at 2.2 GPa in PSTN (see figure 5.16a) is a combined pressure-induced change observed for PST (soft mode at 1.9 GPa) and PSN (change of $\omega\,(p)$ slope at 2.2 GPa). In the case of PSTN-Ba, no soft mode was observed, which is comparable to the results on PST-Ba, but the $d\omega/dp$ slope change at 3.5 GPa (fig 5.16b). It is worth noting that similarly to PST vs PST-Ba, the characteristic pressure point for PSTN-Ba is higher than that for PSTN.
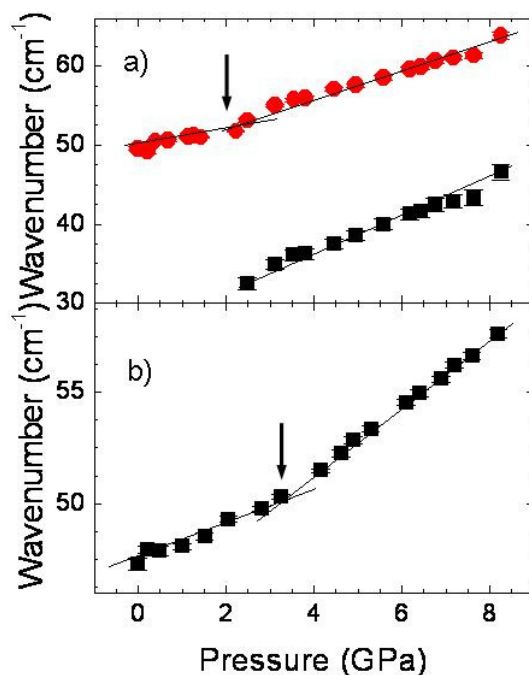
Fig 5.16 Pressure-induced evolution of the Pb-localized mode frequency for a) PSTN and b) PSTN-Ba - Arrows indicate critical pressure points at 2.2 GPa and 3.5 GPa for PSTN and Ba-PSTN, respectively.

The IR-active F_{1u} mode at 160 cm^{-1} representing Pb-atom vibrations against BO$_3$ species is observed as an anomalous Raman signal due to the rhombohedral distortion of the polar nano-regions (PNRs). In pure PST, the splitting of this peak has been observed at a very low pressure of 1.2 GPa, while no splitting was resolvable for PSN as a sign of smaller sized PNR than those in PST. Strong suppression of this mode's intensity (fig 5.17) is indicative of the decoupling of A- and B-sublattices in PNRs and this is due to the volume compression. Such behaviour was found in all investigated compounds, both pure and A-site doped. Between 0 and 1.5 GPa the pressure-evolution of the intensity of this mode differs for PSTN and PSTN-Ba. While in PSTN-Ba the intensity is gradually decreased starting from ambient pressure, in the case of PSTN a plateau exists at low pressure indicating that the coupling resists until 1.5 GPa, in analogy to the PST and PSN behaviour (see figure 5.17a).
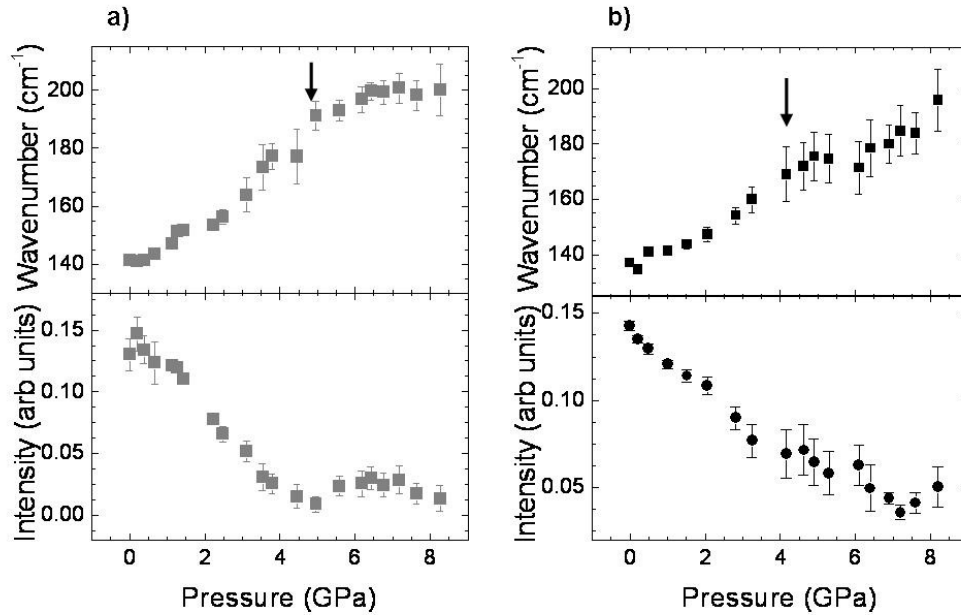
Figure 5.17 Frequency and renormalized intensities of Pb-BO_3 translation mode for a) PSTN and b) PSTN-Ba.

The critical points in the $\omega\,(p)$ evolution of this peak is 5 GPa for PSTN and 4.5 for PSTN-Ba. Up to these pressures, the frequency for both compounds has a sharp change of the gradient which above the critical point stabilises. The intensity drop in the case of PSTN also reaches saturation at 5 GPa, but no such additional pressure can be ascertained for Ba-PSTN. The additional presence of Ba^{2+} on the A-site, even in minimum quantity is sufficient to affect changes in the development of this mode over pressure. The presence of Ba^{2+} lowers the characteristic pressure point to 4.5 GPa (fig 5.17b), hence, Ba^{2+} frustrates the coupling between the A- and B- sublattice.

In Pb-based perovskite-type relaxor materials at ambient conditions, the B-site cations are displaced from their ideal crystallographic positions. When such materials are cooled, progressive cation displacements of the B-cations become apparent and dominant over the Pb-related ferroic species. However, upon pressure-induced volume compression a reduction of the B-cation displacement is an expected feature for perovskite-type ferroelectrics [61,63,109,119-121]. Such a pressure-induced B-cation displacement suppression is apparent from the changes in both, $\omega\,(p)$ and $I(p)$ dependencies of the B-cation localized mode observed around 250 cm^{-1} (presented on figure 5.18). While PSTN exhibits almost identical features upon pressure as its parent compounds PST and PSN, PSTN-Ba differs in this aspect. The frequency softening of the B-localized mode in PSTN reaches its

minimum around 4 GPa and upon further pressure it has a sharp shift towards higher energy. It coincides with the pressure point at which massive *B*-cations abundantly shift towards to the centre of their designated octahedra This is indicated by a sharp drop of the intensity. In pure PST and PSN, the rearrangement in the *B*-sublattice happens between 4 and 6 GPa, while in PSTN a saturation plateau above 4 GPa is not apparent.
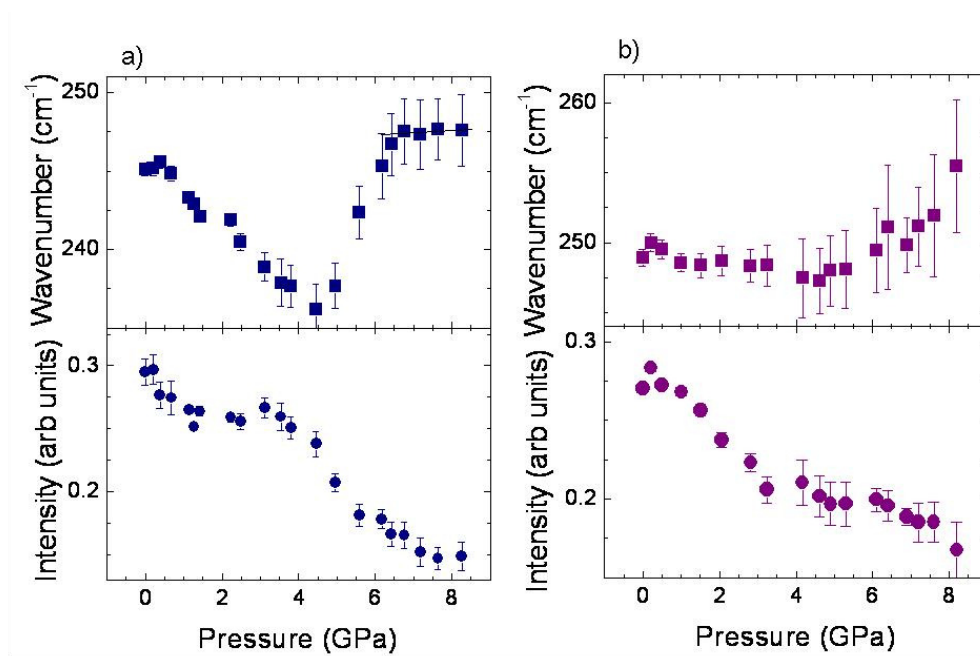
Figure 5.18 Distinct changes in the ω and I of *B*-localized F_{1u} mode for a) PSTN and b) PSTN-Ba.

On the other hand, the additional *A*-site cation in PSTN-Ba introduces a substantial disorder to the *B*-sublattice. The mode frequency softening below 4.5 GPa and subsequent hardening above 4.5 GPa is considerably less pronounced. This is most probably due to the fact that stereochemically inactive Ba disturbs the polar ordering of Ta and Nb already at ambient pressure. The latter can be deduced from the *I(p)* dependence, exhibiting a decrease at very low pressures (~ 0.5 GPa). This indicates that the *B*-site cations are less constrained resulting in their return to the centre of the octahedra at very low pressures ~ 1 GPa. Since the Ta/Nb ratio of cations present at *B*-sites is almost identical for pure and doped PSTN, Ba is directly responsible for the observed differences. This is an important indication of the delicate balance between the *A*- and *B*-subsystem in such a complex system, as well as of the significance of *A*-cation in governing the rearrangement of Sc^{3+}, Ta^{5+} and Nb^{5+} within the BO_6 cage.

The pressure evolution of phonon modes in PST and PSN indicate that the structural transformations occur in a sequence mainly at three characteristic pressure points. Initially the decoupling of the Pb and BO_3 species enables a reorganization of cation positions. Then, Pb-atoms unrestricted by the translation against the BO_3 are active between 2 and 4 GPa, while the B-cations move towards the centre of the BO_6 octahedra. During the volume compression electro-static forces become intense, resulting in Pb getting closer to one of the B-cations. When the bonds in the oxygen sublattice become substantially energetically disproportional Pb moves along the directions normal to the cubic body diagonal. The change in the Pb-O bond stretching reflects correlated changes in Pb-O bonds throughout the structure with an increasing length of coherence. This results in an intensity increase of the peaks observed around 300 and 350 cm^{-1}. In PSTN, an additional splitting of the peak at 350 cm^{-1} is present above 4 GPa suggesting that the two different types of Pb-O dipoles compete, depending on the surrounding octahedral cations. The displacement of Pb placed between Sc^{3+} and Ta^{5+} is inequivalent to the shift of Pb stretched between Sc^{3+} and Nb^{5+} in PSTN.
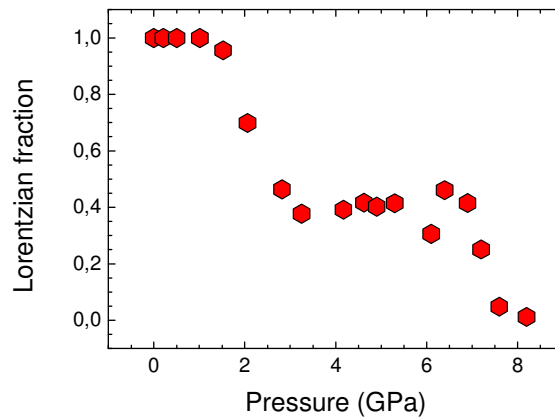
Figure 5.19 Lorentzian fraction in the pseudo-Voigt function on fitting the peak at 350cm^{-1} in PSTN-Ba, arising from Pb-O stretching.

On the other hand, in PSTN-Ba the number of different types of cations create a system too complicated to properly deconvolute in the fitting process. Instead of clearly defined peaks or peak-splitting, broader bands were observed, comprising several different merged vibrations. The use of pseudo-Voigt functions, instead of Lorentzians resulted in better and more stable fittings. The Gaussian peak shape is related with the static disorder within the structure, while the Lorentzian shape is applicable for more ordered systems. Initially a fully Lorentzian shape was assumed

for the peak near 350 cm^{-1}, but on increasing pressure, its fraction significantly dropped into a purely Gaussian shape. In figure 5.19 the Lorentzian fraction changes over pressure marking 3.5 and 6.5 GPa as characteristic pressure points of the structural transformations.

The pressure-induced changes in PSTN and Ba-PSTN are in a good agreement with the results obtained from the pure and Ba-doped parent compounds PST and PSN. Individual spatial regions rich of Ta should exhibit PST-type behaviour and others locally enriched with Nb should show a behaviour typical for PSN; the same should be valid for Ba-containing analogues. At low pressures (< 2 GPa), the coupling between Pb and B-cations is violated releasing the two sublattices which independently adjust to the initiated volume compression. The rate of changes in the A-site cation system may substantially differ from the rate of changes in the B-site cation system due to the mass difference on one hand, and the affinity of Pb to lone pairs on the other hand. The presence of Ba which is stereochemically inactive interferes with the coupling between the A- and B-sublattice. It facilitates the process of structural rearrangement in the B-cation system when pressure is increased because no energy is lost on the decoupling. One should mention that the reduction of B-site cation displacements to a certain minimum (not necessarily zero) value reaches a saturation plateau near 3.5 GPa for the pure compounds or endures a monotonous drop in the case of Ba-doped samples. Due two types of B-site cations, the Pb atoms have inequivalent B-O-Pb angles, which change with pressure due to the process of the BO$_6$ centring. During the unit-cell volume compression, electrostatic interactions between off-centred Pb atoms and the surrounding B^{3+}/B^{5+} cations also change the magnitude of Pb^{2+} off-centre displacements.

To accommodate volume compression, octahedral tilts are a conceivable option, but the direct evidence for such a structural feature cannot be obtained from Raman spectroscopy alone. Nevertheless, the strong enhancement of the Raman peak arising from the Pb-O bond stretching indirectly indicates an improved ferroic order also in the O-system, with symmetry resembling to that of the Pb-sublattice. Out-of-phase octahedral tilting deduced from diffraction data [118] is consistent with observed changes in the Raman spectra and the rearrangements in the Pb-system.

6. Conclusions

Analyses of the Raman data of pure and doped PST and PSN compounds revealed that the pressure-induced structural transformations occur in a well defined sequence between 2 and 6 GPa. The basic scenario is applicable to all investigated compounds. A decoupling between the Pb and BO_3 species occurs at low pressures. The initially strongly displaced B-site cations return to the positions in the centre of the BO_6 octahedra between 2 and 4 GPa. Changes in the Pb-system indicate that the length of coherent displacements of Pb-atoms from the oxygen network in directions normal to the cubic body diagonal improves under pressure. Pb-O ferroic species are favoured at pressure conditions.
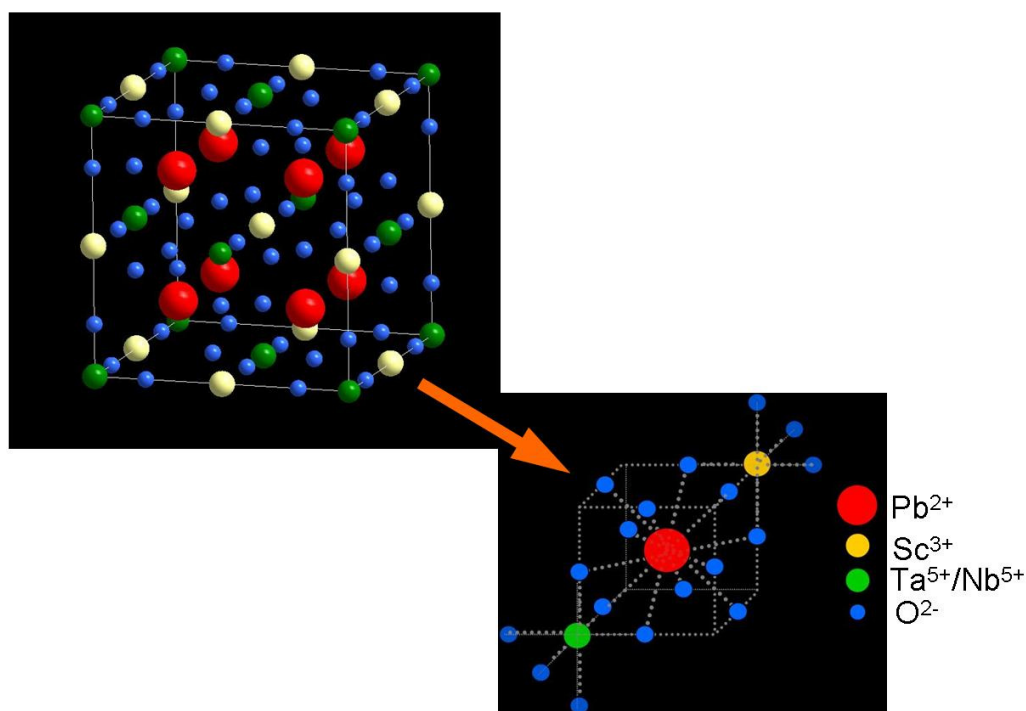
Figure 6.1 Double perovskite cell of $Fm\bar{3}m$ and a 1/8th of the cell enlarged.

Ba^{2+} and Bi^{3+} as doping agents renormalize the pressure-induced structural transformations in Pb-based relaxor similarly to their effect on the temperature-driven structural changes. Stereochemically inactive Ba^{2+} being larger than Pb^{2+}, introduces local elastic fields which act as barriers against a spatial propagation of the coherence in Pb-O non-coplanarity. Thus the presence of Ba^{2+} smears out the phase transition over a pressure

range. In this sense, the substitution of an isovalent element with an isotropic outermost electron-shell for Pb^{2+} in relaxor ferroelectrics leads to a pressure-induced diffuse phase transition. On the other hand, Bi^{3+} has the affinity to form lone-pair electrons and as such introduces less distortion to the orientational order of the Pb^{2+} lone-pair electrons. The incorporation of Bi^{3+} in a $PbB'_{0.5}B''_{0.5}O_3$ matrix even enhances the development of the pressure-induced ferroic order. The case of a mixed PSTN compound with three *B*-site cations bears resemblance to the pressure-induced behaviour of the pure PST and PSN parent compounds, but represents a case of enhanced relaxor structural features. The introduction of Ba^{2+} to such a complex system additionally segments the polar nano-domains, leading to locally encapsulated PST and PSN nano-islands.

This comprehensive study of a series of representative relaxor compounds reveals that chemically-induced local elastic fields play a primary role over the *A*- and *B*-site related charge imbalance for the suppression of long-range ferroic order.

References

[1] Valasek, J, *Phys Rev* **17** 475-481 (1921)

[2] Lines, M. E. and Glass, A. M. *Principles and Applications of Ferroelectrics and Related Materials*, Clarendon Press, Oxford (1977)

[3] Samara, G.A and Venturini, E.L., *Phase Transitions* **70**, 21 (2006)

[4] Kittel, C., *Introduction to Solid State Physics*, Seventh edition, John Wiley and Sons Inc, 394 (1996)

[5] Uchino, K., Nomura, S, Cross, L.E, Jang, S.J. and Newnham, R.E, *J Appl Phys* **51** 1142 (1980)

[6] Shrout, T.R. and Fielding, J. *Ultrasonic Symposium* 711 (1990)

[7] Uchino, K, *Ferroelectrics* **151**, 321 (1994)

[8] Hirota, K, Wakimoto, S. and Cox, D.E. *J Phys Soc Jpn* **75** 111006 (2006)

[9] Egami, T, *Ferroelectrics* **267**, 101 (2002)

[10] Marinova, V., Mihailova, B., Malcherek, T., Paulmann, C., Lengyel, K., Kovacs,, L., Veleva, M., Gospodinov, M., Güttler, B., Stosch, R. and Bismayer, U., *J Phys: Condens Matter* **18**, L385 (2006)

[11] Burns, G. and Dacol, F.H. *Solid State Commun.* **48** 853 (1983)

[12] Tolouse, J., Jiang, F, Svitelskiy, O, Chen, W. and Ye, Z. G. *Phys Rev B* **72** 184106 (2005)

[13] Dul'kin, E., Roth, M., Janolin P.-E. and Dkhil, B. *Phys Rev B* **73** 012102 (2006)

[14] Mihailova, B. Maier, B., Paulmann, C., Ihringer, J., Gospodinov, M., Stosch, R, Güttler, B. and Bismayer U. *Phys Rev* B **77**, 174106/1 (2008)

[15] Blinc, R., Gregorovic, A., Zalar, B., Pirc, B., Laguta, V.V. and Glinchuk, M.D., *Phys Rev* B **63** 024104 (2001)

[16] Gvasaliya, S.N., Roessli, B., Cowley, R.A., Huber, P.and Lushnikov, S.G., *J Phys: Condens Matter* **17,** 4343 (2005)

[17] Gvasaliya, S.N., Pomjakushin, V., Roessli, B., Strässle, Th., Klotz, S. and Lushnikov, S.G., *Phys Rev* B **73**, 212102 (2006)

[18] Hlinka, J., Petzelt, J., Kamba, S., Noujni, D. and Ostapchuk T., *Phase Transitions* **79,** 41 (2006)

[19] Dmowski, W., Akbas, M.K., Davies, P.K. and Egami, T., *J Phys Chem Solids* **61**, 229 (2000)

[20] Blinc, R., Gregorovič, A., Zalar, B., Pirc, R. and Lushnikov, S.G., *Phys Rev* B **61**, 253 (2000)

[21] Woodward, P.M. and Baba-Kishi, K.Z., *J Appl Cryst* **35**, 233 (2002)

[22] Xu, G., Zhong, Z., Bing, Y., Ye, Z.-G., Stock, C. and Shirane, G., *Phys Rev* B **67**, 104102 (2003)

[23] Xu, G., Zhong, Z., Bing, Y., Ye, Z.-G., Stock, C. and Shirane, G., *Phys Rev* B **70**, 064107 (2004)

[24] Takesue, N., Fujii, Y., Ichihara, M. and Chen, H., *Phys Rev Letters* **82**, 3709 (1999)

[25] Malibert, C., Dkhil, B., Kiat, J.M., Durand, D., Bérar, D. and Spasojević-de Biré, A., *J Phys: Condens Matter* **9**, 7485 (1997)

[26] Yokota, H., Oyama, T. and Uesu, Y., *Phys Rev* B **72**, 144103 (2005)

[27] Kumar, A., Murari, N.M., Katiyar, R.S. and Scott, J.F., *Appl Phys Letters* **90**, 262907 (2007)

[28] Kim, T.-Y., Jang, H.-M. and Cho, S.M., *Solid State Communications* **119**, 527 (2001)

[29] Jiang, F., Kojima, S., Zhao, C and Feng, C., *J Appl Phys* **88**, 3608 (2000)

[30] Svitelskiy, O., Toulouse, J., Yong, G. and Ye, Z.-G., *Phys Rev* B **68**, 104107 (2003)

[31] Glinchuk, M.D., Laguta, V.V., Bykov, I.P., Nokhrin, S., Bovtun, V.P., Leschenko, M.A., Rosa, J. and Jastrabik, L., *J Appl Phys* **81**, 3561 (1997)

[32] Laguta, V.V., Glinchuk, M.D., Bykov, I.P., Blinc, R. and Zalar, B., *Phys Rev* B **69**, 054103 (2004)

[33] Dmowski, W., Vakhrushev, S.B., Jeong, I.-K., Hehlen, M.P., Trouw, F. and Egami, T., *Phys Rev Letters* **100,** 137602 (2008)

[34] Juhas, P., Grinberg, I., Rappe, A.M., Dmowski, W., Egami, T. and Davies, P.K., *Phys Rev* B **69**, 214101 (2004)

[35] Cross, L.E., *Ferroelectrics* **76**, 241 (1987); **151**, 305 (1994); ibid **151**, 305 (1994)

[36] Chen, I.-W., Li, P. and Wang, Y., *J Phys Chem Solids* **57**, 1525 (1996)

[37] Hirota, K., *Ferroelectrics* **354**, 136 (2007)

[38] Lufaso, M.W. and Woodward, P.M., *Acta Cryst* B **57**, 725 (2001)

[39] Bhalla, A.S., Guo, R, and Roy, R., *Mat Res Innovat* **4**, 3 (2000)
2 2584 (1961)

[40] Setter, N and Cross, L.E, *J Cryst Growth* **50**, 555 (1980)

[41] Stenger, C.G.F. and Burggraaf, A.J., *Phys Stat Solidi* **A61**, 275 (1980)

[42] Bismayer, U, Devarajan, V. and Groves, P., *J Phys: Condens Matter* **1**, 6977 (1989)

[43] Chu, F., Reaney, I.M. and Setter, N., *Ferroelectrics* **151**, 343 (1994)

[44] Smolenskii, G.A. *J Phys Soc Jpn* **28** 26 (1970)

[45] Cohen, R.E, *Nature* **358**, 136 (1992)

[46] Smolenskii, G.A., Isupov, V.A., Agranovskaya A.I. and Popov, S.N. *Soviet Phys – Solid State*

[47] Isupov, V.A. *Ferroelectrics* **90** 113 (1989); **143** 109 (1995)

[48] Cross, L.E, *Ferroelectrics* **184,** 193 (1996)

[49] Bokov, A. A. *Phys Solid State* **36** 19 (1994); *Ferroelectrics* **190** 197 (1997)

[50] Höchli, U.T., Knorr, K. and Loidl, A. *Advan Phys* **39** 405 (1990)

[51] Ymry, Y, and Ma, S.-K. *Phys Rev Lett* **35** 1399 (1975)

[52] Westphal V., Kleeman, W. and Glinchuk, M.D. *Phys Rev Lett* **68** 847 (1992)

[53] Glinchuk M.D. and Farhi. R. *J Phys: Condens Matter* **8** 6985 (1996)

[54] Samara, G.A., *Phys Rev Lett* **77** 314 (1996)

[55] Samara, G.A., *J Appl Physics* **84** 2538 (1998)

[56] Samara, G.A. and Boatner, L.A., *Phys Rev* B **61** 3889 (2000)

[57] Samara, G.A., *Phys Rev* B **71** 224108 (2005)

[58] Venturini, E.L., Grubbs, R.K., Samara, G.A., Bing, Y. and Ye, Z.-G., *Phys Rev* B **74** 064108 (2006)

[59] Samara, G.A and Venturini, E.L., *Phase Transitions* **79** 21 (2006)

[60] Kreisel, J., Glazer, A.M., Bouvier, P. and Lucaseau, G., *Phys Rev* B **63** 174106 (2001)

[61] Kreisel, J., Dkhil, B., Bouvier, P. and Kiat, J.-M., *Phys Rev* B **65** 172101 (2002)

[62] Chabaane, B., Kreisel, J., Dkhil, B., Bouvier, P. and Mezouar, M., *Phys Rev Lett* **90** 257601 (2003)

[63] Kreisel, J., Bouvier, P., Dkhil, B., Thomas, P.A., Glazer, A.M., Welberry, T.R., Chabaane, B. and Mezouar, M., *Phys Rev* B **68** 014113 (2003)

[64] Kreisel, J. and Bouvier, P., *J Raman Spectrosc* **34** 524 (2003)

[65] Chabaane, B., Kreisel, J., Bouvier, P. and Dkhil, B., *Physical Review* B **70** 134114 (2004)

[66] Szafranski, M., Hilczer, A. and Nawrocik, W., *Journal of Physics: Condensed Matter* **16** 7025 (2004)

[67] Rogacheva, E.A., *Physica* B **291**, 359 (2000)

[68] Bismayer, U., Devarajan, V. and Groves, P., *J Phys: Condens Matter* **1** 6977 (1989)

[69] Salje, E. and Bismayer, U., *J Phys: Condens Matter* **1** 6967 (1989)

[70] Farhi, R., El Marssi, M., Dellis, J.-L., Yuzyuk, Y.I, Ravez, J. and Glinchuk, M.D., *Ferroelectrics* **235**, 9 (1999)

[71] Kim, T.-Y., Jang, H.M. and Cho, S.M., *Solid State Commun* **119**, 527 (2001)

[72] Mihailova, B., Bismayer, U., Güttler, B., Gospodinov, M. and Konstantinov, L., *J Phys: Condens Matter* **14**, 1091 (2002)

[73] Mihailova, B., Bismayer, U., Güttler, B., Gospodinov, M., Boris, A., Berndhard, C. and Aroyo. M., *Z Kristallogr* **220**, 740 (2005)

[74] Güttler, B., Mihailova, B., Stosch, R., Bismayer, U. and Gospodinov, M., *J Mol Struct* **661**, 469 (2003)

[75] Mihailova, B, Gospodinov, M., Güttler, B., Petrova, D., Stosch, R. and Bismayer, U., *J Phys: Condens Matter* **19**, 246220 (2007)

[76] Mihailova, B, Gospodinov, M., Güttler, B., Stosch, R. and Bismayer, U., *J Phys: Condens Matter* **19**, 275205 (2007)

[77] Raman, C.V and Krishnan, K.S, *Nature* No.3048, **121**, 501 (1928)

[78] Nakamoto, K., *Infrared and Raman Spectra of Inorganic and Coordination Copounds, fifth edition, John Wiley and sons, Inc.*(1997)

[79] Sumiya, H., Toda, N, Nishibayashi and Satoh, S., *J Cryst Growth* **178**, 485 (1997)

[80] Eremets. M, *High Pressure Experimental Method, page* 54, Oxford University Press (1996)

[81] Dunstan, D.J. and Spain, I.L., *J Phys: Sci Instrum* **22**, 913 (1989)

[82] Eremets. M, *High Pressure Experimental Method, page* 13, Oxford University Press (1996)

[83] Eremets, M.I., Trojan I.A., Gwaze, P., Huth, J., Boehler, R. and Blank, V.D., *Appl Phys Lett* **87**, 141902 (2005)

[84] Jayaraman, A., *Rev Modern Phys* **55**, 65 (1983)

[85] Asaumi, K. and Ruoff, A. L. *Phys Rev* B **33**, 5633 (1986)

[86] Jephcoat A.P., Mao, H.K. and Bell, P.M., *J Geophys Res* **91**, 4677 (1986)

[87] Milletich, R., Allan, D.A. and Kuhs, W.F., *Reviews in Mineralogy and Geochemistry* **41**, 445 (2000)

[88] Milletich, R., Allan, D.A. and Kuhs, W.F., *Reviews in Mineralogy and Geochemistry* **41**, 455 (2000)

[89] Angel, R., Bujak, M., Zhao, J., Gatta, G.D. and Jacobsen, S., *J Appl Crystallogr* **40,** 26 (2007)

[90] Eggert, J.H., Goettel, K.A. and Silvera I.F., *Phys Rev* B **40**, 5724 (1989)

[91] Eggert, J.H., Goettel, K.A. and Silvera I.F., *Phys Rev* B **40**, 5733 (1989)

[92] Eggert, J.H., Moshry, F., Evans, W.J., Goettel, K.A. and Silvera, I.F., *Phys Rev* B **44**, 7202 (1991)

[93] Syassen K, *High Pres Res* **28**, 75 (2008)

[94] Barnett, J.D., Block, S. and Piermarini G.J., *Rev Sci Instrum* **44**, 1 (1973)

[95] Piermarini. G.J., Block, S., Barnett, J.D. and Forman, R.A., *J Appl Phys* **46**, 2774 (1975)

[96] Mao, H.K., Xu, J. and Bell, P.M., *J Geophys Res* B **91**, 4673 (1986)

[97] Mao, H.K., *Simple molecular systems at very high density*, page 221, Plenum Press, New York (1989)

[98] Angel, R.J., Ross, N.L., Wood, I.G. and Woods, P.A., *Phase Transitions* **39,** 13(1992)

[99] Vos W.L. and Schouten J.A., *J Appl Phys* **69** 6744 (1991)

[100] Milletich, R., Allan, D.A. and Kuhs, W.F., *Reviews in Mineralogy and Geochemistry* **41**, 499 (2000)

[101] Lacam, A., *High Press Res* **5**, 782 (1990)

[102] Lacam, A. and Chateau. C., *J Appl Phys* **66**, 366 (1989)

[103] Boehler, R. and De Hantsetters, K., *High Pressure Res* **24**, 391 (2004)

[104] Carpenter, C.J. and Salje, E.K.H., *Eur J Mineral.* **10**, 693 (1998)

[105] Xu, G., Shirane, G., Copley, J.R.D. and Gehring, P.M., *Phys Rev* B **69**, 064112 (2004)

[106] Howard, C.J., Kennedy, B.J. and Woodward, P.M., *Acta Crystallogr* Sect B **59**, 463 (2003)

[107] Angel, R.J., Zhao, J. and Ross, N.L., *Phys Rev Lett* **95**, 025503 (2005)

[108] Hlinka, J., Otsapchuk, T., Noujni, D., Kamba, S., Petzelt, J., *Phys Rev Lett* **96**, 027601 (2006)

[109] Mihailova, B., Angel, R.J., Welsch, A.-M., Zhao, J., Engel, J., Paulmann, C., Gospodinov, M., Ahsbahs, H., Stosch, R., Güttler, B. and Bismayer, U., *Phys Rev Lett* **101**, 017602 (2008)

[110] Janolin, P.-E., Dkhil, B., Bouvier, P., Kreisel, J. and Thomas, P.A., *Phys Rev* B **73,** 094128 (2006)

[111] Ahart, M., Cohen, R.E., Struzhkin, V., Gregoryanz, E., Rytz, D., Prosandeev, A., Mao, H. and Hemley, R.J., *Phys Rev* B **71**, 144102 (2005)

[112] Chabaane, B., Kreisel, J., Bouvier, P., Lucazeau, G. and Dkhil, B., *Phys Rev* B **70**, 134114 (2004)

[113] Maier, B., Mihailova, B., Paulmann, C., Ihringer, J., Gospodinov, M., Stosch, R., Güttler, B. and Bismayer, U., *Phys Rev* B **79**, 224108 (2009)

[114] Gospodinov, M., *unpublished*

[115] Shannon, R.D. and Prewitt, C.T., *Mat Res Bulletin* **4**, 57 (1969)

[116] Okawa, T., Imaeda, M., Ohsato, H. and Harada, A., *Mat Chem Physics* **79**, 199 (2003)

[117] Welsch, A.-M., Maier, B.J., Engel, J., Mihailova, B., Angel, R. J., Paulmann, C., Gospodinov, M., Friedrich, A., Stosch, R., Güttler, B. and Bismayer, U., submitted for publication to Phys. Rev. B (2009)

[118] Maier, B.J., Welsch, A.-M., Angel, R.J., Mihailova, B., Zhao, J., Engel, J. M., Schmidt, L., Paulmann, C., Gospodinov, M., Friedrich, A. and Bismayer, U, *in preparation*

[119] Welsch, A.-M., Mihailova, B., Gospodinov, M., Stosch, R., Güttler, B. and Bismayer, U., *J Phys: Condens Matter* **21**, 235901 (2009)

[120] Ravy, S., Itie, J.P., Polian, A. and Hanfland, M., *Phys Rev Lett* **99**, 117601 (2007)

[121] Jaouen, N., Dhaussy, A.C., Itie, J.P., Rogalev, A., Marinel, S. and Joly, Y., *Phys Rev* B **75**, 224115 (2007)

[122] Shannon, R.D., *Acta Crystallogr.* A **32**, 751 (1976)

Appendix

Gas-membrane driven easyLab µScope-RT (G) DAC operating manual

1. General description

The μScope-RT(G) diamond anvil cell (DAC) produced by easyLab (earlier Diacell) resides on the combined system of gas-membrane for increasing and 4 bolts for securing pressure in between the anvil-holding pistons. It consists of four principle parts (see fig A.1):

    1. Outer clamping ring

    2. Pressure plate

    3. Gas membrane

    4. Inner piston-cylinder DAC
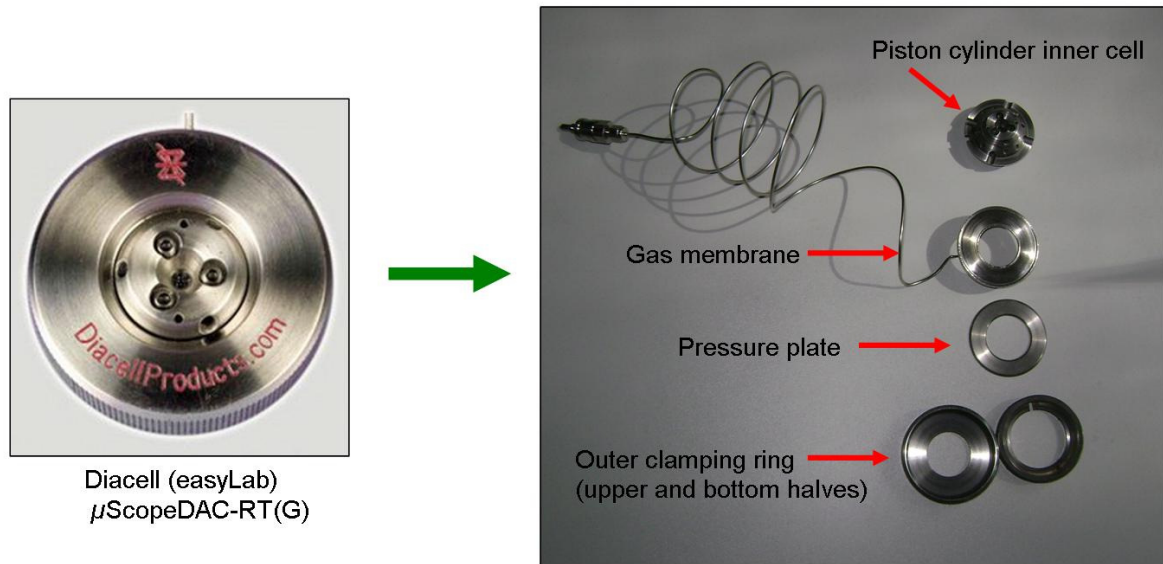
Figure A.1 Diacell gas-membrane driven DAC μScope-RT(G) assembled as
ready for experiment (left) and disassembled into major parts.

The outer ring serves to fix the gas-membrane onto the piston cylinders of the inner cell and hold them tightly together during the pressure loading. In order to protect the gas membrane from inverting during the experimental run, the pressure plate needs to lay flat inside on the upper outer ring and with its convex side on the upper side of the gas-membrane.

The inner DAC is held together by a system of 4 clamping bolts. This part can be used without the gas-membrane part, as a simple DAC where pressure is introduced by tightening the clamping bolts up to maximum load of 5 GPa (fig A.2).
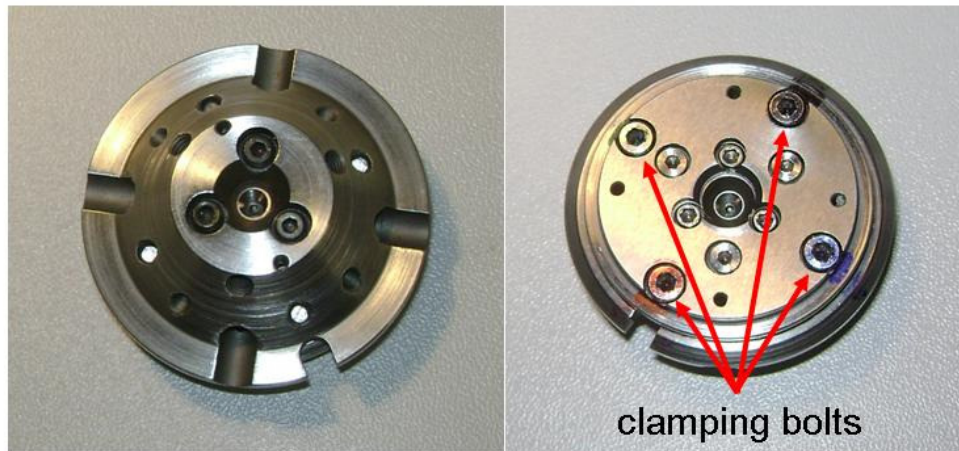
upper half   lower half

Figure A.2 View of the upper and lower half of the inner cell. Clamping bolts should always match their assigned hole, marked by individual colours.

All clamping bolts are marked with a particular colour to ensure that the same bolt always goes into its own hole. In such a way, the threads within the holes are preserved directly improving the stability of the cell under pressure. The inner cell consists of two piston cylinders which intimately fit into one another (fig A.3). Due to the symmetry of the inner parts of the pistons, which retain anvils, it is crucially important to maintain the exact positions of the bottom piston relative to the top piston while closing the cell. The bolt and the bottom anvil hole marked with red should always come on the side of the indentation of the upper anvil (see fig A.3).
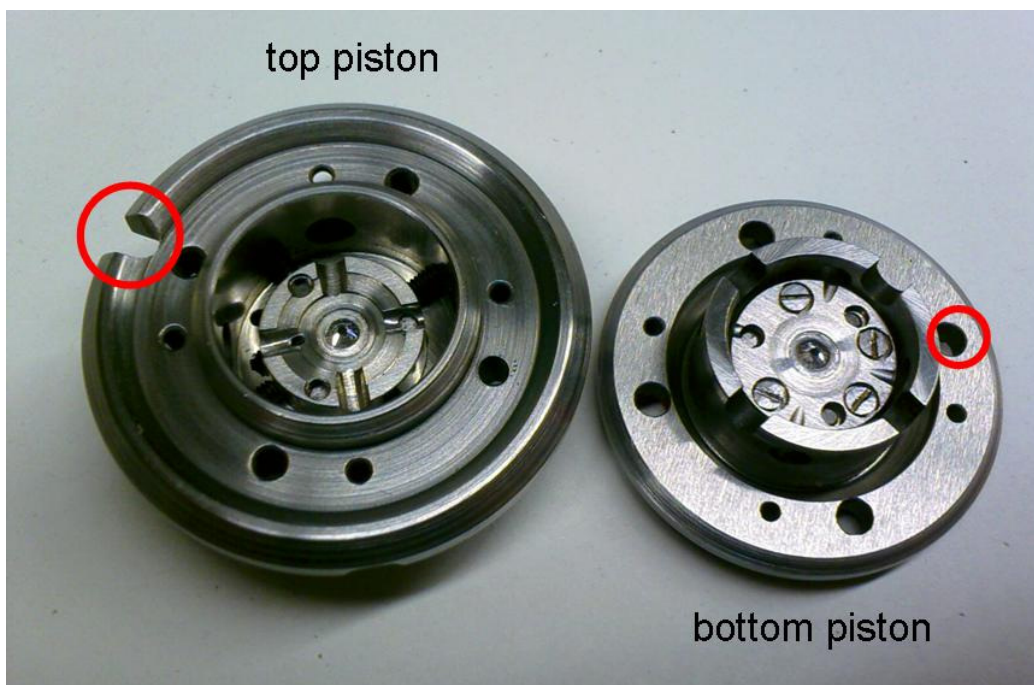
Figure A.3 Inner cell opened. Due to the specific symmetry of the inner, anvil-retaining parts, it is important to follow the proper piston orientation while closing the cell – red hole should come on the top of the indentation (for the gas membrane inlet hose, also marked in red on the top piston).

Figure A.4 Diamond anvils mounted in steel for protection and secure fixing within the cell.

The diamond anvils used in this cell, with steel ring mounting (fig A.4) are positioned laying on their flat side on top of the carbide seats inside the piston cylinders. Each anvil is held in the position by sets of anvil-retaining screws, marked on figure A.5. The upper anvil has 3 retaining screws which hold the anvil in position while the bottom anvil has 4 small screws that hold the anvil screwed onto the half-sphere (see fig A.7 marked by red circle). After exchanging the anvils, the upper and lower anvil holders must be returned to their initial position in respect to the individual piston symmetry.
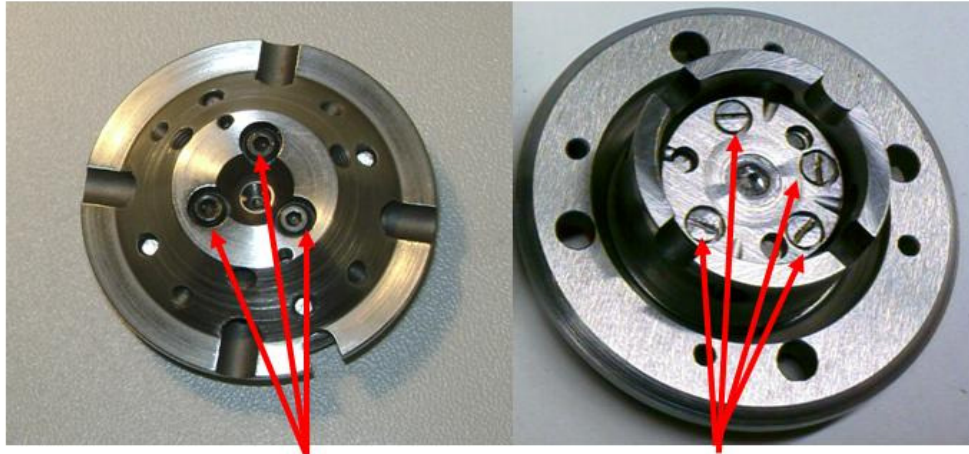
Upper anvil retaining screws   Bottom anvil retaining screws

Figure A.5 Red arrows mark the positions of the upper and bottom anvil retaining screws, which hold the diamonds in attached to the cell.

The top and bottom diamond anvils are positioned with the diamond table facet touching the carbide seat and the culet facing upward when the pistons are disassembled and positioned flat on a surface. When the pistons are closed, the anvil culets should be brought into a contact. During every exchange of the diamond anvils, the carbide seats and diamond anvils themselves *must* be kept absolutely clean, especially from fingerprints. Usually, the cotton swabs dipped in iso-propanol are used while the diamonds and piston parts are being secured with tweezers.

A vertical and horizontal alignment of the culets follows every exchange of the anvils. An additional control of the diamond alignment is often necessary after extensive experimental pressure-loadings, especially if changes in the gasket hole have stopped the experiment. The anvil culets need to perfectly coincide in the horizontal plane and be perfectly parallel one to another in the vertical plane (see figure A.6).
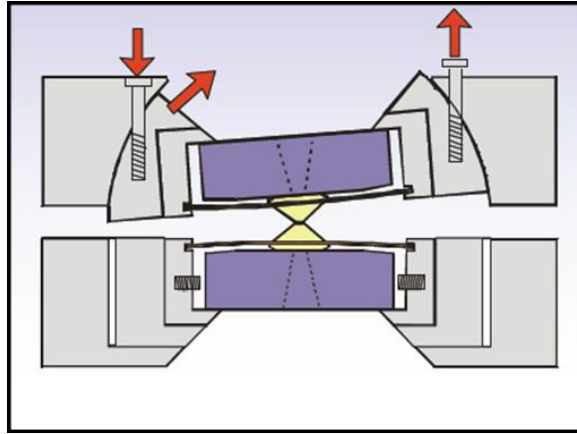
Figure A.6 Vertical aligning of the diamond anvils. The anvil attached to the half-sphere is rotated until the culets become perfectly parallel.

In the μScope-RT(G) DAC, the upper anvil can be horizontally adjusted and the bottom anvil can be vertically tilted. The alignment procedure should be performed as following:

1. The upper anvil is fixed on the carbide seat, fitted into the holder (see fig A.7); the holder is positioned properly inside the upper anvil (relative to the piston symmetry) and fixed by the three screws although not completely, since the upper anvil must be allowed to shift laterally
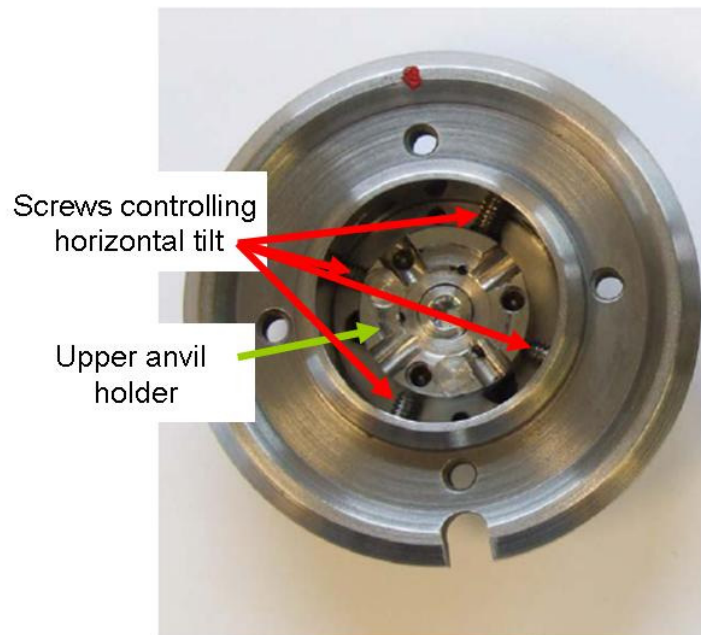
Figure A.7 Holder of the upper anvil, pointed at by a green arrow and 4 screws controlling lateral position of the anvil.

95

2. The lower anvil is exchanged by unscrewing of the 4 small screws marked on the right-hand side on figure A5. Upon exchanging of the anvil, they should be fixed as much as possible. It was a very unfortunate and unforeseen event when these screws started to rust, resulting in the bottom anvil failure. After that event the new set of screws was meticulously dipped in grease before tightening. It should also be underlined that the screws responsible for holding the half-sphere (marked on picture A.8 as "tilt screws" by a red arrow and the half-sphere by red circle) *should not* be removed or unscrewed.
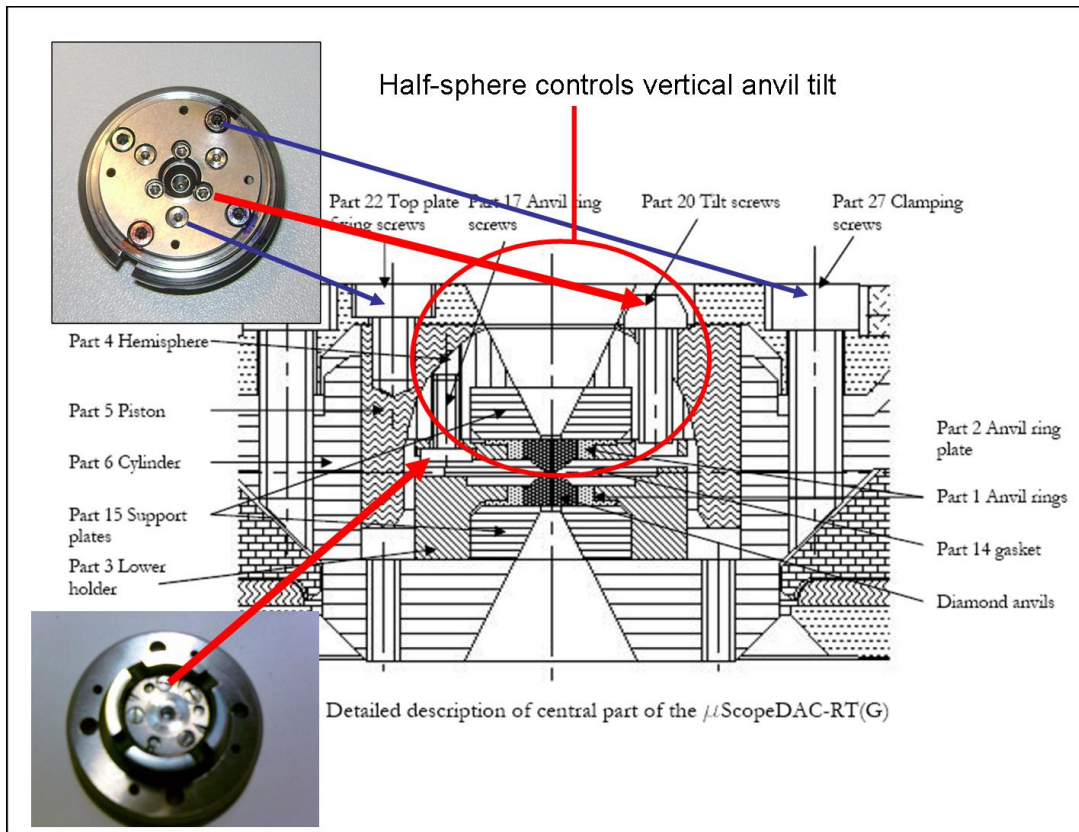
Figure A.8 Scheme provided in the user guide for the easyLab μScope-RT(G) describing the position of the anvils within the inner cell (on this scheme, it is upside down). With red circle was marked half-sphere which controls the vertical diamond tilt. Red arrow points to the small screws retaining the bottom anvil and the big ones controlling the tilt of the half-sphere. Clamping bolts and top-plate fixing screws marked by blue arrows just for clarity.

3. When both anvils are securely placed in their holders and held in place by the retaining screws, the piston cylinders are assembled one into another so that the culets touch. Aligning of the diamonds is the most sensitive part because the culets are in close contact and the risk of them breaking or chipping is extremely high. Proceeding with the alignment must be done with **the utmost care, patience and lightness of touch!** The alignment of the anvils requires a well-lit observational microscope (binocular, by preference) with sufficiently large working area assuring easy approach to all sides of the inner cell, with possibility of working under light reflection or transmission modes with equal ease.

4. The process of the culet alignment begins with the adjustments of the upper anvil's lateral position so that the culets coincide (figure A.9) when viewed in the transmission mode through the microscope. The upper anvil is shifted in the horizontal plane by inserting and rotating 2 of 6-sided Allen keys (aka 'inbus') in the screw holes at the sides of the upper piston (see figure A.10). When the culets are positioned perfectly one on top of the other, the three upper anvil retaining screws marked on figure A.5 are completely tightened, fixing the position.
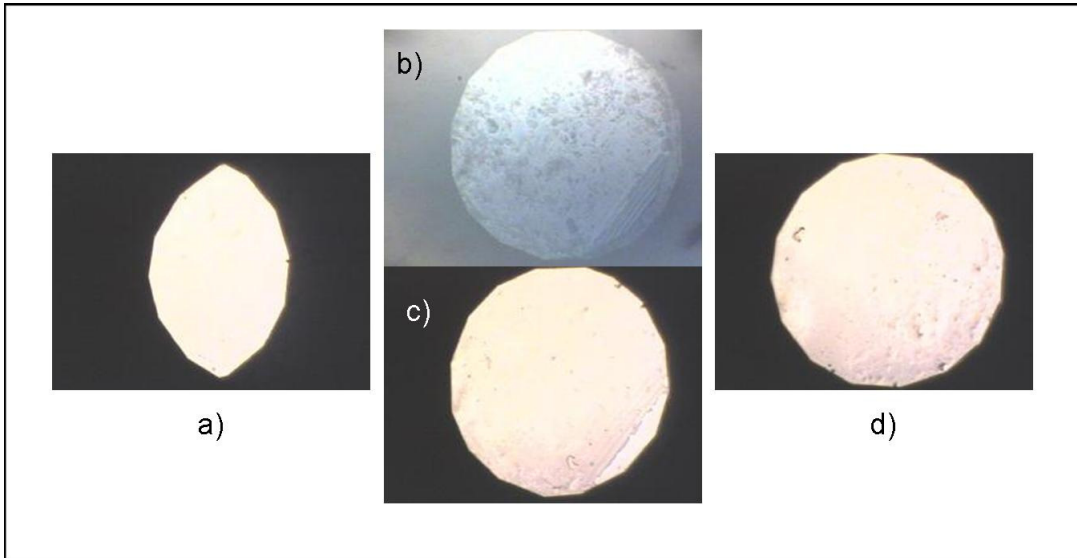
Figure A.9 The image change produced in a transmission light microscope regime during lateral alignment of the anvils of easyLab μScope-RT(G) cell: a) the initial position, b) the reflection mode showing the off-set of the anvils, c) the same is insufficiently visible in the transmission mode; d) the image of the properly aligned anvils.
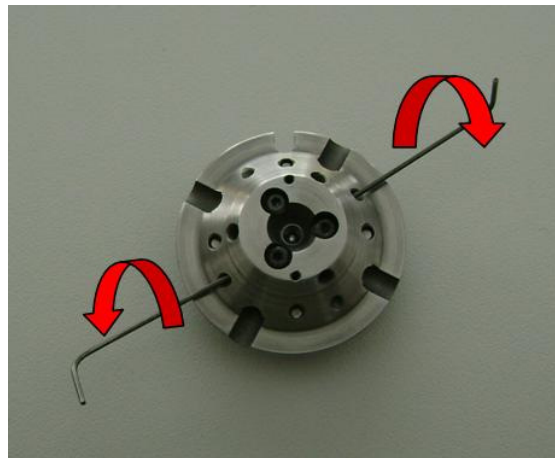
Figure A.10 Lateral adjustment of the upper anvil position with two small Allen keys during the alignment procedure.

5. After the culet alignment in the horizontal plane the inner cell is turned upside down in order to adjust the vertical tilt by controlling the tilt of the half-sphere held by the three 'tilt screws' marked on figure A.8 (as 'part 20' on the scheme). The reduction of the vertical offset anvil tilting can be observed by the disappearance of the Newton fringe lines (see figure A.11). If the culets are vertically tilted one from another, it means that a

certain culet area becomes exposed to higher pressure load. This is very dangerous since not only that stress shall be unevenly distributed causing gasket-flowing, but anvils might be driven to failure during the experiment. When the vertical tilt is properly adjusted, the lower half-sphere is securely fixed by tightening the three 'tilt screws'. In such a way any potential lateral or vertical anvil movements are prevented and diamonds are both protected and ready to be maximally utilized.
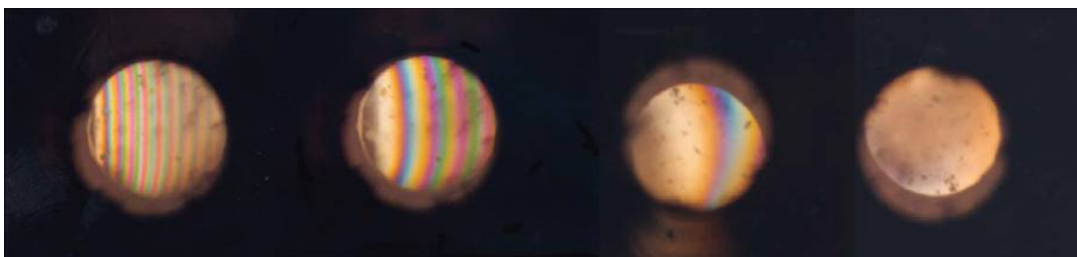
Figure A.11 Newton interference fringe lines disappear when the culets are perfectly parallel one on another, while in intimate contact.

The freshly aligned diamonds should be checked after the first few pressure-loading cycles, in order to prevent misalignment occurring as a consequence of relaxation after the pressure decrease. When the diamonds are properly aligned and the inner cell carefully opened, the diamonds should be cleaned with alcohol, from any traces of dirt, dust or grease under the microscope, before proceeding with the sample loading.

2. Cell loading

In order to prepare the cell for sample-loading, it is necessary to use pre-indented, drilled and cleaned gasket. Gaskets for easyLab μScope-RT(G) cell are bought ready-made. Before the indentation of the gasket to the desired thickness, a small scratch is made on the surface of the gasket in order to enable it to always be placed inside the cell in the exact same way (see figure A.12). The pre-indented gasket is drilled in the middle of the indented area, enabling for the sample to be

safely and optimally positioned in the gasket hole during the experiment. Additionally, any potential deformation of the gasket hole during the experimental run can be noticed before it reaches the edge of the culets, consequently exposing the diamonds under stress to a direct contact.
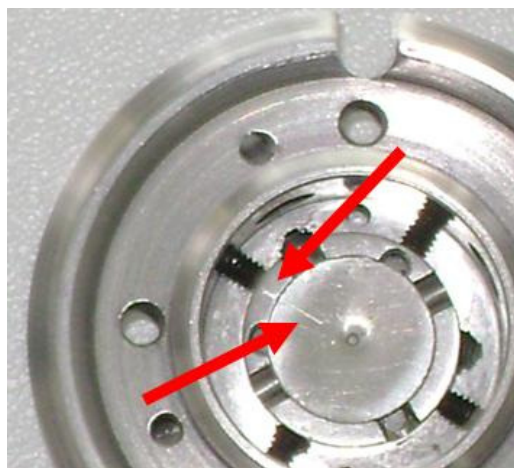
Figure A.12 Markings on the gasket should always coincide to the marking on the inner ring of the upper piston.

Some of the basic tools needed for sample loading are shown on the figure A.13. Previously cut, polished to thickness of ~ 50 μm and cleaned sample is put on a laboratory glass holder. A few drops of alcohol are put around the sample grain in order to create a sphere denser than air. Inside this bubble a piece of the sample is cut using the very tip of the scalpel. Since the alcohol evaporates quickly it leaves the sample cut dry within minutes. The sample cut should be roughly of the size 50 x 50 x 50 μm and as regular as possible. With the tip of the needle (figure A.13d), the sample is lifted from the glass holder and positioned into the centre of a perfectly clean culet. Spectroscopic experiments do not tolerate glycerine as a gluing medium, which is the usual approach in the sample loading for single-crystal XRD experiments under high pressure. A minute quantity of ruby chips is positioned next to the sample, or as more often the case – spread in the vicinity of the sample.
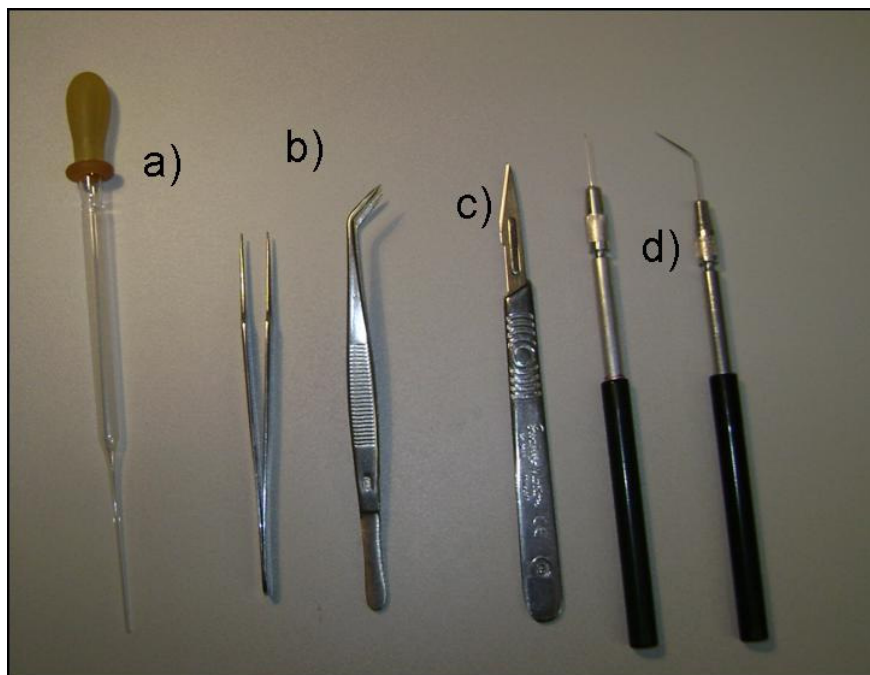
Figure A.13 Basic tools used for DAC sample loading: a) pipette for injecting pressure medium, b) tweezers with very fine tips, c) scalpel with a flat top edge and d) exceptionally thin long needles for picking up and manoeuvring the sample onto the culet.

The most complicated part of the sample loading is the positioning of the gasket so that the undisturbed sample ends up in the middle of the gasket hole (usually 150 μm in diameter for culets of 500 μm). This process is so complicated in practice that it very often ends up destroying or losing the sample. The soundest way is to position the gasket on a glass plate, in a similar position as it should lie within the cell, and pick it up by the very tips of the fine tweezers with bent ends (figure A.13b, pair to the right). The process of lowering the gasket onto the diamond can be controlled through the microscope by using a low magnification and long focus.

Once the gasket is positioned and sample resides in the middle of the hole, the pressure medium is administered by adding small drops on the side of the gasket until the quantity is sufficient. It should be spread out across the gasket surface and inside the hole with the sample, but without spilling over the gasket edge. Through the microscope it should be controlled that no bubbles of air is accidentally caught inside the gasket hole. In such a case bubble can be removed by careful piercing with a long thin needle without disturbing either the sample or the gasket.

The closing of the cell is the riskiest part in the sample loading procedure in the case of the easyLab μScope-RT(G). Usually it is achieved by taking the bottom piston and aiming through the empty clamping bolt holes to the exact position of the

corresponding holes of the upper piston laying flat, packed with gasket and pressure medium on it. With a controlled and careful push, bottom piston is pressed inside the upper one as far as it can be manually achieved. If the microscope check confirms that the sample is still locked between the anvils, in the centre of the gasket hole, pistons are clamped together with 4 bolts and the cell is ready for the laser. Since the sample is not glued on the diamond, at lower pressures it is possible that the sample and ruby shall float inside the pressure medium and slightly shift about. At pressures above 2 GPa, the sample usually does not shift around anymore.
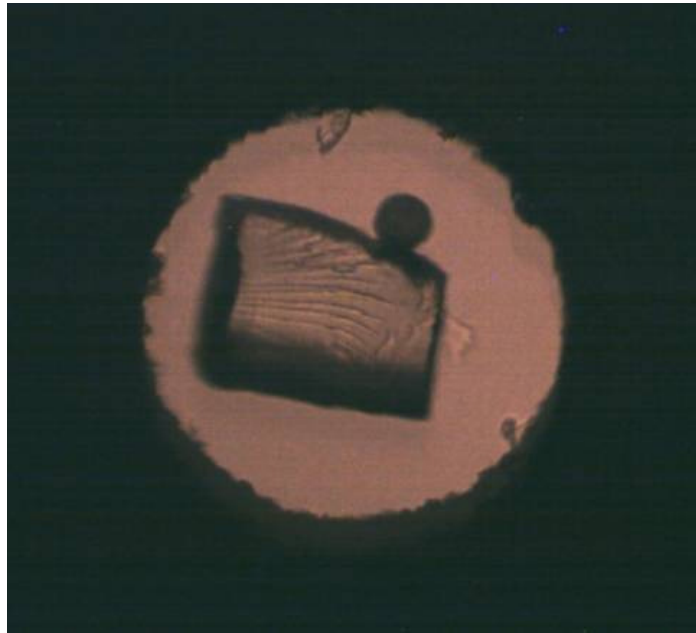
A.14 PST sample next to a sphere of ruby as a pressure calibrant at ambient
pressure, inside DAC (photographed in a transmission mode of light).

Acknowledgments

Curriculum Vitae

Surname	Welsch (Velč)
Name	Anna-Maria Erika (Ana-Maria Erika)
Date of Birth	November 19th 1977
Place of Birth	Belgrade, Serbia
Office address	Mineralogisch-Petrographisches Institut, Universität Hamburg Grindelallee 48, D-20146 Hamburg, Germany phone: +49 (0)40 42838-2076 / fax: +49 (0)40 42838-2422 e-mail: anna.maria.welsch@uni-hamburg.de

Education

Oct 1996 – Apr 2003	Studies of Mineralogy and Crystallography at the Belgrade University, Belgrade Serbia – Department for Geology; diploma thesis titled "Pressure-induced structural changes in Seignette salt (KNaC$_4$H$_4$O$_6$ • 4H$_2$O)", thesis advisor Prof. Dr. R.Ž. Dimitrijević
Jun 2001 – Dec 2001	Gemmological Institute at Idar-Oberstein, Germany: courses in gemmology and diamonds
Oct 2006 – Sep 2009	Doctorate studies at the University of Hamburg, Germany, involved in the Raman spectroscopic studies of the relaxor ferroelectrics under high-pressure

Participation at schools for PhD students and young scientists:

- Diamond anvil cell techniques, Bayerisches Geoinstitut, Bayreuth, Germany, April 2007
- High pressure – high temperature mineral physics: Implications for Geosciences, Bressanone – Brixen, Italy, February 2008
- Laser heating at high pressures, Institut für Geowissenschaften, J.W.Goethe-Universität, Frankfurt-am-Main, Germany. March 2008
- Mathematical and Theoretical Crystallography, Gargnano, Italy, May 2008

List of publications

1. Mihailova B., Angel R.J., **Welsch A.-M.**, Zhao J., Engel J., Paulmann C., Gospodinov M., Ahsbahs H., Stosch R., Guttler B. and Bismayer U. (2008): Pressure-induced phase transition in $PbSc_{0.5}Ta_{0.5}O_3$ as a model Pb-based perovskite-type relaxor ferroelectric, *Physical Review Letters* **101**, 017602; (selected for the *Virtual Journal of Nanoscale Science & Technology*, **18**(2) 2008)

2. **Welsch A.-M.**, Mihailova B., Gospodinov M., Stosch R., Guttler B. and Bismayer U., (2009): High pressure Raman spectroscopic study on the relaxor ferroelectric $PbSc_{0.5}Nb_{0.5}O_3$, *Journal of Physics: Condensed Matter* **21**, 235901

3. **Welsch A.-M.**, Maier B.J., Engel J., Mihailova B., Angel R. J., Paulmann C., Gospodinov M., Friedrich A., Stosch R., Güttler B. and Bismayer U., Effect of Ba on pressure-induced strcutural changes in the relaxor ferroelectric $PbSc_{0.5}Ta_{0.5}O_3$, *to be published in Phys. Rev. B*

4. Maier, B.J., **Welsch, A.-M.**, Angel, R.J., Mihailova, B., Zhao, J., Engel, J. M., Schmidt, L., Paulmann, C., Gospodinov, M., Friedrich, A. and Bismayer, U: A-site doping induced renormalization phenomena in $PbSc_{0.5}Nb_{0.5}O_3$ under high pressure, *in preparation*

Contributions to Conferences

5. **Welsch, A.-M.**, Mihailova, B., Malcherek, T., Gütter, B., Paulmann, C., Gospodinov, M. and Bismayer, U. The effect of La-doping on the structure of Pb-based relaxors, 15. Jahrestagung der DGK 2007, Bremen, March 05-09, poster

6. Mihailova, B., **Welsch, A.-M.**, Gütter, B., Gospodinov, M. and Bismayer, U. Relaxor ferroelectrics: ferroic clustering and phonon anomalies, 71. Jahrestagung der DPG 2007, Regensburg, March 20-30, 2007, talk.

7. **Welsch, A.-M.**, Mihailova, B., Malcherek, T., Gütter, B., Paulmann, C., Gospodinov, M. and Bismayer, U. Local structural phenomena in Ba-containing $PbSc_{0.5}B"_{0.5}O_3$, 71. Jahrestagung der DPG 2007, Regensburg, March 20-30, 2007, poster.

8. **Welsch, A.-M.**, Mihailova, B., Malcherek, T., Güttler, B., Paulmann, C., Gospodinov, M., Bismayer, U. Effects of A-site doping on the local structure of Pb-based relaxor ferroelectrics. SERBIAN CRYSTALLOGRAPHIC SOCIETY XIV Conference of the SKD (SCS) with international participation, Vrsac 28 – 30. Jun 2007.

9. **Welsch, A.-M.**, Mihailova, B., Malcherek, T., Güttler, B., Paulman, C., Gospodinov, M., Bismayer, U. Effects of A-site doping on the structure of Pb-based relaxors, 2nd International Workshop, Kiel, Germany, 29.-31.08.2007, oral presentation.

10. **Welsch, A.-M.**, Mihailova, B., Malcherek, T., Güttler, B., Paulman, C., Gospodinov, M., Bismayer, U. The effect of A-site doping on the structure of Pb-based relaxors, 11th European Meeting on Ferroelectricity, Bled, Slovenia, 3-7 Sep 2007, poster

11. Mihailova, B., Güttler, B., **Welsch, A.-M.**, Gospodinov, M., Paulmann, C., Malcherek, T., Stosch R. and Bismayer, U. Ferroic Clustering and Phonon Anomalies in Pb-based Relaxor Ferroelectrics, 11th European Meeting on Ferroelectricity, Bled, Slovenia, 3-7 Sep 2007, oral presentation.

12. **Welsch A.-M.**, Mihailova B., Stosch R., Güttler B., Gospodinov M., Bismayer U. Pressure-induced structural transformations in $Pb_{0.78}Ba_{0.22}Sc_{0.5}Ta_{0.5}O_3$; a Raman spectroscopic study. 16. Jahrestagung der DGK 2008, Erlangen, March 03-06, talk

13. Mihailova, B., Angel, R.J., **Welsch, A.-M.**, Zhao, J., Engel, J., Paulmann, C., Gospodinov, M., Güttler, B. and Bismayer, U. Pressure-induced phase transition in $PbSc_{0.5}Ta_{0.5}O_3$ as a

model Pb-based perovksite-type relaxor ferroelectric. 2. Berichtskolloquium of the SPP1236, 16-18 June 2008, Freiberg, Germany, poster.

14. **Welsch, A.-M.**, Mihailova, B., Stosch, R., Güttler, B., Gospodinov, M. and Bismayer, U. Local structural changes in pure and Ba-doped $PbSc_{0.5}Ta_{0.5}O_3$ and $PbSc_{0.5}Nb_{0.5}O_3$ relaxor ferroelectrics under high pressure. 2. Berichtskolloquium of the SPP1236, 16-18 June 2008, Freiberg, Germany, talk.

15. Mihailova B., Angel, R.J., Maier B., **Welsch, A.-M.**, Paulmann C., Malcherek T., Gospodinov M., Güttler B., Bismayer U., Temperature- and pressure-induced structural changes in the perovskite-type relaxor ferroelectric $PbSc_{0.5}Ta_{0.5}O_3$. 86. Jahrestagung der Deutschen Mineralogischen Gesellschaft (DMG), Berlin, 14. - 17. September 2008. talk

16. **Welsch, A.-M.**, Mihailova B., Gospodinov, M., Stosch, R., Güttler, B., Bismayer U., High-pressure Raman spectroscopy of Ba-doped $PbSc_{0.5}Ta_{0.5}O_3$ and $PbSc_{0.5}Nb_{0.5}O_3$ relaxor ferroelectrics. 86. Jahrestagung der Deutschen Mineralogischen Gesellschaft (DMG), Berlin, 14. - 17. September 2008, talk.

17. **Welsch, A.-M.**, Mihailova, B., Gospodinov, M., Stosch, R., Güttler, B., Bismayer U., High-pressure Raman spectroscopy of Nb- and Sn-doped $PbSc_{0.5}Ta_{0.5}O_3$ relaxor ferroelectric, 17. Jahrestagung der DGK, Hannover, 9-12. März 2009, talk

18. **Welsch, A.-M.**, Mihailova B., Gospodinov, M., Stosch, R., Güttler, B., Bismayer U., Pressure-induced local structural changes in PSN, PSN:Bi and PSN:Ba. DPG Frühjahrstagung der Sektion Kondensierte Materie (SKM), Dresden, 22. - 27. März 2009, talk.

19. **Welsch, A.-M.**, Mihailova, B., Maier, B., Angel, R., Paulmann, C., Gospodinov, M., Güttler B. and Bismayer, U. , High pressure-induced renormalization phenomena in lead scandium niobates and tantalates with relaxor behaviour, Antragskolloquium SPP1236, Ebernburg, Bad Münster, 31.03.09 - 2.04.09, poster

20. **Welsch, A.-M.**, Mihailova, B., Maier, B., Engel, J., Paulmann, C., Angel, R, Zhao, J., Gospodinov, M., Stosch, R., Güttler B. and Bismayer, U., Effect of Ba on pressure-induced changes in the relaxor ferroelectric $PbSc_{0.5}Ta_{0.5}O_3$, 1st Workshop for the Extreme Conditions Beamline at PETRA III, 18.05.09 - 19.05.09, poster